MICROFLUIDIC ASSEMBLY AND PACKING DYNAMICS OF COLLOIDAL GRANULES

BY

ROBERT F. SHEPHERD

DISSERTATION

Submitted in partial fulfillment of the requirements
for the degree of Doctor of Philosophy in Materials Science and Engineering
in the Graduate College of the
University of Illinois at Urbana-Champaign, 2010

Urbana, Illinois

Doctoral Committee:

Professor Jennifer Lewis, Chair
Professor Ralph Nuzzo
Professor Gustavo Gioia
Professor Nancy Sottos
Assistant Professor Shen Dillon

ABSTRACT

Granular materials composed of primary colloidal particles are of both scientific and technological importance. The creation of granular systems for fundamental studies of their packing dynamics as well as applications ranging from ceramics processing to low-cost MEMS devices requires the ability to precisely control the granule size, size distribution, shape, and composition. Many methods exist for producing colloidal granules, including fluidized granulation, high shear mixer granulation, and spray drying. However, none of these methods provide adequate control over these important parameters. In this thesis, we use microfluidic-based assembly methods to control granular size, shape, and chemical heterogeneity. We then investigate the packing dynamics of non-spherical granular media using X-ray micro-computed tomography.

Monodisperse spheroidal granules composed of colloid-filled hydrogels are created in a sheath-flow microfluidic device. By exploiting the physics of laminar flow in microchannels, drops composed of silica microspheres suspended in an aqueous acrylamide monomer solution are created within a continuous oil phase. The interfacial tension between these two immiscible fluids drives a Rayleigh-mode instability that promotes drop formation. Next, the drops undergo photopolymerization to create an acrylamide hydrogel that freezes in the desired morphology and composition during assembly. To demonstrate the flexibility of this new granulation technique, we assemble both dense homogenous and Janus granules in both spherical and discoid geometries.

To produce non-spherical granular media, a lithographic-based microfluidic technique known as stop-flow-lithography is employed. Specifically, colloidal granules and microcomponents in the form of microgear, triangular, discoid, cuboid, and

rectangular shapes are produced by this approach. In addition, pathways are demonstrated that allow these building blocks to be transformed into both porous and dense oxide and non-oxide structures.

Finally, large quantities of non-spherical colloidal granules of controlled surface roughness are created via stop-flow lithography in cube and rectangular prism geometries of varying polydispersity. Their packing behavior under static and dynamic conditions is investigated by X-ray micro-computed tomography. Their voronoi volume distribution is quantified as a function of granule shape and agitation time using image analysis techniques. These data are then fit to a probabilistic *k*-Gamma analytical function, which allows one to quantify an order parameter, *k*, for the jamming condition of low dispersity cube, rectangular prism and bimodal cube granules. We find a steadily decreasing *k*-value for monodisperse cubes, suggesting local cube rearrangement during consolidation; while monodisperse rectangular granules and a bimodal distribution of cube granules demonstrate a relatively consistent *k*-value during consolidation, suggesting the local granule configuration remains similar. In each case, the data collapse onto a single master curve, suggesting a qualitatively similar jamming condition during compaction.

ACKNOWLEDGEMENTS

I would like to thank my advisor, Professor Jennifer Lewis, for her guidance and support throughout my graduate school experience. I appreciate the freedom she gave me to pursue my scientific interests, as well as her enthusiasm for the research that we did; I hope we will continue to work together in the future.

I would like to thank the members of my research group whom have been allies in my journey through graduate school. Most of those I was closest to are not here at the time of my graduation, but I feel that they are close anyway. Ranjeet, Dan, Summer, Mark, Jaci, Bok, Chris, and Willie – thanks for making it fun to come to work.

I thank my parents for being wonderful. They support me no matter whether I would be a janitor or an astronaut.

I need to acknowledge the wonderful staff members of both the ITG and MRL facilities on campus—without them much of my research would not have been possible. From the ITG, I would like to thank Scott Robinson, Jon Ekman, Darren Stevenson and Lei-lei Yin; from the MRL I would like to thank Scott McLaren and Vania Petrova.

I would also like to express my sincere appreciation to my thesis committee members: Professor Ralph Nuzzo, Professor Nancy Sottos, Professor Gustavo Gioia, and Professor Shen Dillon. I have been fortunate to have been able to interact with these intelligent, thoughtful professors in varying degrees throughout my graduate school experience.

I need to thank my wonderful wife, Jen. She has made me human and given me purpose. Without her, I most likely would not be graduating.

I would also like to thank my collaborators, Professors Gustavo Gioia, Patrick Doyle, David Weitz, and Ralph Nuzzo for taking my research to the next level.

TABLE OF CONTENTS

CHAPTER 1

INTRODUCTION AND RESEARCH SUMMARY

1.1 Introduction

Granular matter is used in industrial processes more than any other material, except water.[1] Many granular materials consist of assemblies of colloidal particles, whose primary particle size ranges from a few nanometers to several microns.[2] For example, colloidal granules are utilized as feedstock in ceramic,[3, 4] food,[5] cosmetic,[6] and pharmaceutical[7] industries. By intentionally granulating colloidal particles, transport and processing problems that arise due to their large surface area-to-volume ratio, such as wall-stick, health hazards from inhalation, and inefficient compaction into pills, tablets, or other forms, are mitigated.[8] Nevertheless, granular matter exhibits a rich array of behavior, including gas, liquid, and solid-like responses under largely athermal conditions.[9, 10]

Colloidal and granular particles display identical physical characteristics, the only difference being the effect of thermal fluctuations on fluidized colloids. This difference is captured by the Langevin equation, $ma = F(x) - \beta v + \lambda(t)$, where F(x) is the interaction force on the particle from particle collisions, βv is the viscous force due to the particle velocity, and $\lambda(t)$ is a noise term. $\lambda(t)$ arises due to thermal effects in colloidal fluids[2] and to external driving forces, such as vibration, in athermal granular media.[9, 11] This somewhat unifying concept of colloidal and granular dynamics coupled with their pervasiveness provides motivation to both create and systematically investigate the behavior of model colloidal granules.

To create model granular materials, one must be able to precisely control the size, size distribution, shape, and composition of colloidal granules of interest. Many methods exist for

producing colloidal granules, including fluidized granulation,[12] high shear mixer granulation,[13] and spray drying.[4] However, none of these methods provide adequate control over these key parameters, which are important for both fundamental experiments and technological application as low-cost MEMS,[14-16] designer pharmaceuticals,[17,18] or optical displays.[19] Thus, my PhD research aims to engineer colloidal granules of narrow size dispersion, with exquisite control over shape and chemical composition using microfluidic-based assembly methods.

1.2 Thesis Scope and Organization

In this thesis, concentrated colloid-filled hydrogels are formulated for use in drop-based flow focusing and stop flow lithography (SFL) microfluidic devices. Several system parameters are optimized, including colloid concentration, hydrogel content, interfacial tension, flow parameters, optical properties, UV exposure conditions, and microfluidic device architecture to produce spherical, non-spherical, and chemically heterogeneous (Janus) colloidal granules and novel microcomponents. The packing behavior of cuboid colloidal granules of varying aspect ratio is investigated under static and dynamic conditions via X-ray micro-computed tomography (μCT). The key findings of this research are described in the following chapters:

In Chapter 2, spherical granules are produced by photocuring the colloidal suspension drops formed using a flow-focusing device. Prior to photocuring, the drops are molded into sphere and oblate sphere (discoid) geometries through manipulation of microchannel architecture. Additionally, by controlling fluid flow within the formed drops, two different streams of colloidal suspension were able to be sequestered to form both spherical and discoid Janus granules.

In Chapter 3, non-spherical granules and microcomponents are produced via stop-flow lithography of an index-matched, colloid-filled photopolymerizable suspension. Several objects are created including those with triangular, cube, hollow cube, and microgear (diameter c.a. 300μm) motifs. The colloidal microgears are then transformed into functional components via thermal sintering and magnesiothermic reduction to form dense glass and porous silicon microgears, respectively.

In Chapter 4, packing of cuboid granules of varying aspect ratio as well as triangular under static and dynamic conditions is investigated by μCT.

Finally, in Chapter 5, the principal findings of this research are summarized.

1.3 References

1. Buchanan, M., *Think outside the sandbox.* Nature, 2003. **425**(9): p. 556-557.
2. Russel, W.B., *Brownian Motion of Small Particles Suspended in Liquids.* Ann. Rev. Fluid Mech., 1981. **13**: p. 425-455.
3. Lewis, J.A., Journal of the American Ceramics Society, 2000. **83**(10): p. 2341-2359.
4. Lukasiewicz, S.J., *Spray-Drying Ceramic Powders.* J. Am. Ceram. Soc., 1989. **72**(4): p. 617-624.
5. Hogekamp, S., M. Stang, and H. Schubert, *Jet agglomeration and dynamic adhesion forces.* Chemical Engineering and Processing, 1994. **33**: p. 313-318.
6. Oulahna, D., *et al., Wet granulation: the effect of shear on granule properties.* Powder Technology, 2003(130): p. 238-246.
7. Simons, S.J.R., *et al., Predicting the performance of granulation binders through micro-mechanistic observations.* Powder Technology, 2004. **140**: p. 280-289.
8. Saleh, K., L. Vialatte, and P. Guigon, *Wet granulation in a batch high shear mixer.* Chemical Engineering Science, 2005(60): p. 3763-3775.
9. D'Anna, G. and G. Germaud, *The jamming route to the glass state in weakly perturbed granular media.* Nature, 2001. **413**: p. 407-409.

10. Jop, P., Y. Forterre, and O. Pouliquen, *A constitutive law for dense granular flows.* Nature, 2006. **441**(7094): p. 727-730.

11. Cundall, P.A. and O.D.L. Strack, *A discrete numerical model for granular assemblies.* Geotechnique, 1979. **29**: p. 47-65.

12. Cryer, S.A., *Modeling Agglomeration Processes in Fluid-Bed Granulation.* AIChE Journal, 1999. **45**(10): p. 2069-2078.

13. Darelius, A., *et al.*, *High shear wet granulation modelling--a mechanistic approach using population balances.* Powder Technology, 2005(160): p. 219-218.

14. Lehmann, O. and M. Stuke, Science, 1995. **270**: p. 1644-1646.

15. Schuster, R., V. Kirchner, and P. Allongue, *Electrochemical Machining.* Science, 2000. **289**(5476): p. 98-101.

16. Desbiens, J.-P. and P. Masson, *ArF excimer laser micromachining of Pyrex, SiC and PZT for rapid prototyping of MEMS components.* Sensors and Actuators A, 2007(136): p. 554-563.

17. Pitts, P., M. Tew, and A. Preate, *21st Century Health Care Terrorism: The Perils of International Drug Counterfeiting*. 2005, Center for Medicines in the Public Interest, Pacific Research Institute. p. 6.

18. *Guidance for Industry Incorporation of Physical-Chemical Identifiers into Solid Oral Dosage Form Drug Products for Anticounterfeiting*. 2009, Food and Drug Administration: Rockeville. p. 11.

19. Chen, Y., *et al.*, *Flexible active-matrix electronic ink display.* Nature, 2003. **423**(6936): p. 136-136.

CHAPTER 2

MICROFLUIDIC ASSEMBLY OF SPHERICAL COLLOIDAL GRANULES

2.1 Introduction

A new route for forming colloidal granules is enabled by the emergence of microfluidic techniques that allow monodisperse emulsion drops to be generated by coflowing immiscible fluids at low Reynolds number, *Re*.[1-5]. Using this approach, both pure hydrogel[6, 7] and polymeric particles[8-11] (ca. 10 – 200 μm in diameter) have been produced via *in-situ* photopolymerization of monomeric drops in the form of homogeneous[6, 7], Janus particles[12-15], and discoids[8-11]. More complex microfluidic geometries have even produced hollow polymeric particles via multiple emulsion techniques. In addition, microfluidic devices have been used to synthesize colloids[16] and to aggregate colloidal particles into "photonic balls" using extremely dilute suspensions ($\phi \leq 0.01$)[17]. In this chapter, I report the first demonstration of microfluidic assembly of dense colloidal granules with precisely controlled shape and composition.

Microfluidic devices consist of an interconnected network of microchannels, whose diameter varies from ca. 10μm to 1mm. These devices are typically produced by soft lithography,[18] as shown in **Figure 2.1**. In this approach, a positive relief pattern is first formed by lithographically patterning SU-8 phtoresist on a silicon wafer. After this, a poly(dimethyl siloxane) (PDMS) prepolymer is poured over the SU-8 and allowed to cure at elevated temperature. The cured replica is then peeled off and bonded to a PDMS substrate to form microchannels. To date, microfluidic devices have been developed for material synthesis techniques[16, 19], assembly of "photonic balls"[17], and producing solid spherical[8, 11, 15], hollow[20, 21] and non-spherical [8, 11, 15, 22, 23] polymeric particles.

Microfluidic devices provide for exquisite control over fluid flow due to the minimization of inertial forces from the confinement of fluid elements in the microenvironment. This concept is captured in the generic Reynolds number, (*Re*):

$$Re = \frac{\rho u L}{\eta}$$

Where *r, u,* η are the density, velocity, and viscosity of the fluid and *L* is the dimensions of the fluid vessel respectively. The numerator reflects contribution of inertial forces, which are limited in micro-confined flow due to the small size of *L* while the viscous component, shown in the denominator acts to dampen turbulent flow. Typically, when *Re* <<100, there is a transition from turbulent to laminar flow.

The laminar flow of fluids within microfluidic devices has been exploited to create monodisperse emulsion droplets, as shown in **Figure 2.2**. The microchannel geometry used to generate these drops plays a critical role in determining the mode of initial drop formation and properties of the resultant particles. There are two primary forms of drop forming geometries: T-Junction, (TJ), and flow focusing devices, (FFD). Both routes create droplets in a bounded squeeze flow[24, 25] and are primarily sensitive to flow rate considerations. Drop formation is promoted by an interfacial tension that arises between immiscible fluids.

There are two distinct modes of drop formation in laminar flow: dripping and jetting. [26, 27] In dripping mode, drop formation occurs at low Capillary number (*Ca*):

$$Ca = \frac{\eta_m u}{\sigma}$$

where η_m is the viscosity of the outer fluid, u is the fluid velocity at the interface of the immiscible fluids, and σ is the interfacial tension between the immiscible fluids. The Ca is

determined by the balance of the shear force to the interfacial tension between the immiscible fluids. When interfacial tension is large compared to the shear forces, the Rayleigh instability drives drop formation at the orifice, **Figure 2.3a,b**. When the outer, continuous, fluid flows faster and creates a high shear environment, the Ca increases and can pull the inner fluid into a jetting mode prior to drop breakup **Figure 2.3c**. Finally, if the inner fluid is flowing too quickly, then the inner fluid extends beyond the capillary into a widening jet. This transition from dripping to widening-jet mode is defined by the Weber number (*We*) of the inner fluid,

$$We = \frac{\rho_{in} d_{tip} u_{in}^{\ 2}}{\sigma}$$

where ρ_{in} is the density of the internal fluid, d_{tip} is the tip diameter, and u_{in} is the mean velocity of the inner fluid. The *We* relates inertial forces to the interfacial tension of the system. In particular, when the inertia of the inner fluid is large relative to the interfacial tension, this allows the inner fluid to jet into the outer fluid prior to drop formation, creating a widening jet, **Figure 2.3d**. The representative, experimentally determined, phase diagram for drop formation in laminar flow is shown in **Figure 2.4**, for an inner fluid of $We < 1$ and an outer fluid of $Ca \leq 1$. In this regime, drop formation occurs via a dripping mode, which is preferred due to its stability and predictability.

For each drop forming device the addressable size scale of drops is slightly different, however, all drop forming techniques have a minimum size equal to that of the orifice when formed in a dripping mode regime. The fundamental limit on drop size is a balance between the Laplace pressure on the drops themselves,

$$\Delta P = P_{in} - P_{out} = \frac{2\sigma}{r}$$

and the chemical potential of the system where P_{in} is the pressure within the drop, P_{out} is the pressure outside the drop, and r is the drop radius. Practically, droplets have been formed in a controlled fashion as small as tens of nanometers via e-jet processes[12, 28] and in the micron-range using standard microfluidic devices[2, 29], where the final droplet size is approximated by relating the Laplace pressure to external shear forces[2]:

$$r \propto \frac{\sigma}{\eta_m \dot{\gamma}}$$

Figure 2.5 illustrates the effect of shear rate ($\propto \frac{u_{out}}{u_{in}}$) on drop size for different architectures of T-Junction, and flow focusing devices, where u_{out} is the outer fluid velocity and u_{in} is the inner fluid velocity. [29] As the shear rate is increased, u_{out} exceeds the internal fluid flow, u_{in} the microfluidic geometries approach a drop volume of 3pL, or ~10μm diameter. Though smaller drop sizes can be reached, **Figure 2.5b** the increased shear rates cause an increase in drop size dispersion. This study also reveals a particular channel geometry capable of producing relatively large droplets, c.a. 100μm, in the granular size regime, **Figure 2.5a (far right)**. This geometry features a widening output channel which is employed in our granule forming channel geometries.

The dynamic fluid flow within the drops themselves must also be considered. Depending on the external shear environment of the drops, the flow dynamics within the formed droplets vary dramatically from hemispherically symmetric to completely asymmetric, see **Figure 2.6**[30]. These considerations must be taken into account to either promote or prevent fluid mixing within drops[5, 31, 32]; for example, mixing is promoted in asymmetric flow within drops[5], whereas it is suppressed by a hemispherically symmetric motif.

By properly understanding the details of fluid flow within drops, discrete chemistries have been controlled within single drops; e.g., Ref. [15] describes coflowing two miscible fluids into an immiscible continuous fluid using an axisymmetric flow focusing device, **Figure 2.7**. By generating photopolymerizable drops within the device and subsequently curing them by UV light, one can produce solid, polymeric microparticles whose shape is defined by the microchannel geometry, as shown in **Figure 2.8**. Because the droplets want to minimize surface energy, they adopt a spheroid surface curvature. By deforming these droplets within microchannels, the droplets adopt either disk, oblate or rod, prolate spheroids with aspect ratios that depend on the microchannel geometry, as shown in **Figure 2.8e,f**[11]. Exposure of the monomeric droplets to UV light solidifies the microparticle in the shape defined by the microchannel, **Figure 2.9**.[11] By varying the monomer chemistry, both hydrophilic[16,17] and hydrophobic[20,21] spherical polymer spheres have been synthesized. By adjusting the channel geometries within the microfluidic devices, i.e. by deforming drops in channels of different aspect ratios prior to solidification, disk and rod shaped polymeric particles have also been produced **Figure 2.9**.[18,19,21]

In this chapter, we extend microfluidic assembly routes to create monodisperse colloid-filled hydrogel granules of tunable size, geometry, and composition. We exploit the physics of laminar flow in microchannels to first generate drops composed of silica microspheres suspended in an aqueous acrylamide monomer solution within a continuous oil phase. The interfacial tension between these two immiscible fluids drives a Rayleigh-mode instability[1, 33] that promotes drop formation. Next, the drops undergo photopolymerization to create an acrylamide hydrogel that freezes in the desired morphology and composition during assembly. To

demonstrate the flexibility of this new granulation technique, we assemble both dense homogenous and Janus granules in both spherical and discoid geometries.

2.2 Experimental Methods

2.2.1 Material System

Colloidal suspensions are prepared by adding an appropriate amount of monodisperse silica microspheres (ϕ_{silica} = 0.01 – 0.45, 500 nm ± 25nm diameter, FUSO, Japan) to an aqueous solution composed of acrylamide ($\phi_{acrylamide}$ = 0.01-0.3, Acros Organics), the crosslinker N,N methylenebisacrylamide ($\phi_{crosslinker}$ = 0.001-0.03, Aldrich), and the photoinitiator 2,2 diethoxyacetophenone, DEAP, ($\phi_{initiator}$ = 0.005, Aldrich) in deionized water at pH 7 following a procedure similar to that reported in Ref. [34]. To aid direct visualization, silica microspheres (ca. 500 nm in diameter) are synthesized either with a fluorescent, rhodamine isothiocyanate (RITC) or fluorescein isothiocyanate (FITC), core-shell architecture following the procedure described in Ref. [35]. **Table 2.1** contains the inlet compositions used in these experiments, where FITC denotes a 1:1 mixture of pure silica:FITC core-shell silica microspheres, RITC denotes a 1:1 mixture of pure silica:RITC core-shell silica microspheres, and oil refers to a 1:1 mixture of mineral oil (heavy viscosity, PTI Process Chemicals) and hexadecane (H0255, Aldrich) that contains a surfactant (2% by weight, Span 80, Aldrich) and the photoinitiator ($\phi_{initiator}$ = 0 - 0.05). The interfacial tension between the suspension and the oil phase is determined using the pendant drop method[36], and found to be 10 mN/m, 4 mN/m, 3 mN/m, and 1 mN/m for φ_{silica} of 0, 0.15, 0.36, and 0.45, respectively, at a fixed $\varphi_{acrylamide}$ of 0.165.

2.2.2 Preparation of Microfluidic Devices

Microfluidic devices are produced via soft lithography[36] by pouring polydimethylsiloxane (PDMS, Sylgard 184, Dow Corning) onto a silicon wafer patterned with

SU-8 photoresist features (Microchem, SU-8 50 for disk forming channels and SU-8 100 for sphere forming channels). The microchannel dimensions used in these experiments are provided in **Table 2.1**.

2.2.3 Drop Formation

Monodisperse drops are formed in the sheath-flow microfluidic device illustrated schematically in **Figure 2.10a**. The colloidal suspension(s) and oil are loaded into 500 μL glass syringes (1750TTL, Hamilton) and infused into the device via digitally controlled syringe pumps (KDS 100, KD Scientific). The viscosities of a representative colloidal suspension (ϕ_{silica} = 0.36, $\phi_{acrylamide}$ = 0.165) and the oil are 9 cP and 15 cP, respectively, as measured at a strain rate of 250 sec^{-1} using a controlled stress rheometer (C-VOR 200, Bohlin). Immediately after each drop is generated, the acrylamide solution is gelled by activating the photoinitiator using a UV lamp with 8000 mW/cm^2 illumination intensity (N2100 UV lamp, Exfo) that is directed through a 1" diameter collimating lens (Exfo) at a height of 2 cm above the device surface. We measure the drop gelation time, defined as the UV exposure time required to suppress the Brownian motion of colloidal particles within them, as a function of acrylamide and initiator concentration. To quantify the extent of polymerization as a function of exposure time, we perform thermogravimetric analysis (TGA) (Pyris 6, Perkin-Elmer) on representative dried granules heated to 800°C at 10°C/min in air.

2.2.4 Determination of Interfacial Tension

The pendant drop method[36] is used to determine the interfacial tension of the colloidal suspension and mineral oil solution. The interfacial tensions is determined via the shape of the pendant drop, defined by the shape factor β, which is dependent on D_e and D, where *De* is the

diameter of the drop at the capillary tip and *D* is the maximum diameter of the drop, **Figure 2.10**. The relevant equation for interfacial tension[36],

$$\sigma = \frac{\Delta\rho R_o^2 g}{\beta}$$

Where $\Delta\rho$ is the density difference between the colloidal suspension and mineral oil, R_o is the radius of curvature at the drop apex, g is gravity.

2.2.5 Observation of Drop Formation

Drop generation is observed using a high-speed camera (Phantom V7.1, Visible Solutions) mounted on an inverted fluorescence microscope (IX-71, Olympus). Direct visualization of both homogeneous and Janus granules is achieved via excitation of the FITC or RITC core-shell silica microspheres using a 100 W Mercury lamp (Chiu Tech. Corp.), whose light was directed through a 500-700 nm (TRITC, Chroma Tech. Corp.) or 450-650 nm (FITC, Chroma Tech. Corp.) filter for red or green excitations, respectively. Representative granules are dried and imaged using scanning electron microscopy (SEM) (6060 LV, JEOL). Image analysis is performed using "Image J" software on representative wet and dry granule populations (> 100 granules) to determine their size distribution. In addition, selected dried granules are freeze-fractured in liquid nitrogen and then imaged using SEM to probe their internal structure.

2.3 Results and Discussion

Colloid-filled hydrogel granules are assembled in a sheath-flow, flow focusing microfluidic device with the specified shapes and chemical compositions, shown schematically in **Figure 2.11a-b**, using the inlet compositions and channel geometries described in **Table 2.1**. A fluorescence image of the Y-junction formed at the intersection of inlets [1] and [2] is shown in **Figure 2.11c** for the device used to produce Janus granules. The green inlet [1] contains FITC

core-shell silica microspheres in suspension, while the red inlet [2] contains RITC core-shell silica microspheres in suspension. A core-shell architecture is adopted for the fluorescent microspheres to eliminate the deleterious interaction between one of the hydrogel constituents and the embedded dye. In these devices, laminar flow and diffusive mixing dominate due to their small channel dimensions and low flow rates. Hence, negligible mixing occurs between the coflowing red and green fluid streams, as evident in **Figure 2.11c**.

Further downstream in the device, drops are generated at the widening flow focusing orifice formed by the two oil inlets, denoted as [3] in **Figure 2.11a**. The orifice channels widen from 100μm to 220μm, a ratio similar to that formed by Abate *et al.* to form 100μm fluid drops at a Ca # approaching 0.5.[29] Correspondingly, the width of the necked region where the drop formation occurs, yields monodisperse granules approximately 100 μm in diameter (see **Figure 2.11d**). Again, drop formation is driven by the competition between the viscous shear and surface tension between these two immiscible fluids and occurs at a critical capillary number[37], under appropriate conditions, the inner fluid is sheared via external pressure from the continuous phase to an extension long enough to allow surface tension to drive the jet into a drop conformation[1]. As demonstrated previously[1-4], slight variations in the oil flow rates and channel geometries result in large variations in drop size. For example, when the flow rate of the continuous phase increases, smaller drops form due to a greater extension per volume of the inner fluid element.

To determine the optimal conditions for forming robust colloid-filled hydrogel granules, we investigate the influence of suspension composition on the production of monodisperse granules at fixed flow rates ($Q_{suspension}$ = 100 μl/hr and Q_{oil} = 300 μL/hr). The results are summarized in the processing phase diagram shown in **Figure 2.12**. When the silica volume

fraction is relatively high, the suspension breaks in a jetting mode yielding polydisperse drops due to their decreased interfacial tension, see **Figure 2.10**; even after factoring in the average fluid suspension densities of each volume fraction, there is a marked drop in in interfacial tension from the increasing silica volume fraction**.** From this, a moderate volume fraction of silica must be chosen for reliable drop formation. Additionally, when the initial acrylamide concentration is low, significant granule deformation and adhesion occurs upon drying, **Figure 2.12**. Thus, an optimal suspension composition of 36 v/o silica and 16.5 v/o acrylamide is identified for the short residence times (~ 3 sec of UV exposure) employed in this device. At this composition, a *Ca* of 0.5 is used to form granules of 100 μm in diameter in a dripping mode. Under these conditions, granules are generated at a rate of 45-65 Hz and travel at a velocity of ~ 6 mm/s.

To prevent the chemically distinct hemispheres of our Janus granules from mixing upon drop breakup, we use a flow focusing, sheath flow device (**Fig. 2.11d**) that directs oil flow around the spheres uniformly at breakup. Although the fluid motion within these drops exhibits a recirculatory flow pattern[5, 30], **Figure 2.13**, this does not lead to mixing of the hemispheres. In fact, Particle Imaging Velocimetry (PIV) establishes that the recirculatory flow actually promotes fluid sequestration in individual hemispheres, **Figure 2.13b,c**, as it has a flow pattern similar to that in **Figure 2.6a**. Upon exiting the microchannels, however, the shear environment changes thereby promoting mixing of the hemispheres in a manner that is likely similar to **Figure 2.6b**. To immobilize the colloids within each drop, we photopolymerize the aqueous acrylamide solution to form a solid hydrogel network (see **Fig. 2.11a**). This solidification process preserves both the non-spherical and chemically heterogeneous configurations of the granules even as they exit the microfluidic device. The exposure time of the drops to UV light is important as a minimum time is necessary to crosslink the acrylamide to a sufficient content to

bind the colloids. Due to the finite drop velocity (6mm/s) and the exposure area of our UV source (~2cm), the maximum exposure time possible is ~3 s. ThermoGravimetric Analysis (TGA) determines that a 3 s exposure time results in a 3 wt% loss from burnout in dried, solventless granules, **Figure 2.14**. Considering the ~20 wt% acrylamide monomer pre-exposure, this corresponds to a 15% conversion of monomeric acrylamide into polyacrylamide. This is verified by the long exposure time TGA measurements showing ~20 wt% loss, corresponding to 100% conversion of monomeric acrylamide into polyacrylamide for 20 s and 180 exposures, **Figure 2.14**.

To optimize the kinetics of hydrogel formation, we explore the effects of photoinitiator and acrylamide concentration on the polymerization process. Solidification must occur within a few seconds to suppress unwanted mixing or shape changes during assembly given the current device design and flow rates. In preliminary experiments, drops of fixed composition exhibit highly irregular gelation behavior. Such inconsistencies arise due to the solubility of the photoinitiator in the oil phase. The photoinitiator rapidly diffuses from the droplets prior to UV exposure due to the enhanced convective diffusion from the fluid recirculation environment.[30] We therefore measure the gelation time, defined as the exposure time at which the Brownian motion of the colloids first ceases, as a function of initiator concentration at a fixed acrylamide concentration. Upon adding a critical concentration of photoinitiator ($\varphi_{initiator} \sim 0.05$) to the oil phase, drops are reproducibly and rapidly gelled (< 3 sec), as shown in **Figure 2.15a**. The addition of photoinitiator within the oil phase is essential for maintaining its desired concentration in each drop. Although the use of a more water-soluble photoinitiator would alleviate this need, acetophenone-based species allow more rapid gelation kinetics. We have now identified an acetophenone photoinitiator that is soluble in our suspension conditions, but did not

use this at the time of publication. We also measure the gelation time as a function of acrylamide concentration at the optimal initiator concentrations of $\varphi_{initiator}$ of 0.005 in suspension and $\varphi_{initiator}$ of 0.05 in oil. For initial acrylamide concentrations below approximately $\varphi_{acrylamide}$ of 0.03, gelation does not occur, **Figure 2.15b**. At higher initial concentrations, the gelation times decrease from ~ 20 sec for $\varphi_{acrylamide}$ of 0.04 to less than 3 sec for $\varphi_{acrylamide}$ of 0.165. For the optimal initial acrylamide concentration, $\varphi_{acrylamide} \sim 0.165$, TGA experiments reveal that only 15% of the initial acrylamide in solution polymerizes under these exposure conditions. The excess species are likely removed during the solvent exchange and drying process. To fully polymerize the initial acrylamide in solution, longer exposure times (> 10 sec) are required.

To demonstrate the flexibility of this new granulation route, we assemble colloid-filled hydrogel granules of varying composition and shape. Specifically, we produce homogeneous and Janus granules in both spherical and discoidal shapes. They are imaged using fluorescence microscopy in the wet state without removal of excess oil (**see Fig. 2.16**). The characteristic size of the spherical granules is ~ 110 μm with a standard deviation of 4.2%. For the discoidal granules, the major and minor axes are ~115 μm and ~58 μm respectively, resulting in a minor-to-major axis ratio, α, of ~ 0.50. A coefficient of variation is not reported for these granules due to an insufficient population of discoids that are tilted at appropriate angles for image analysis.

To demonstrate the efficacy of this process as a route for forming robust granules, we harvest and dry the colloid-filled hydrogel granules. It is necessary to exchange the low volatility oil phase with a higher volatility solvent, in this case octane, during the drying process. Pure hydrogel drops (**Fig. 2.17a**) contract to nearly half of their initial volume upon drying, whereas colloid-filled drops only contract until a random close-packed particle network formed ($\phi \sim 0.64$)[38]. After solvent exchange, we obtain colloid-filled hydrogel granules with

relatively smooth surface morphologies. The dried granules retain their spherical (80 μm in diameter) or discoid (D_{major} = 90 μm, D_{minor} = 56 μm) geometries, as shown in **Fig. 2.17b,c**. Interestingly, the aspect ratio of the dried discoid granules is slightly higher than that observed in the wet state, although the reason for this anisotropic shrinkage is unclear. Finally, within each dried granule, the silica microspheres assemble into a random close-packed network, as shown in **Fig. 2.17d**.

2.4 Conclusions

Microfluidic-based assembly offers a facile route for assembling monodisperse colloid-filled hydrogel granules of well-controlled size, morphology and composition. To preserve their structure, we utilize *in situ* photopolymerization of an acrylamide-based solution during drop generation. For the first time, the production of both homogeneous and hemispherically distinct (Janus) colloidal granules in either spherical or discoidal geometries is demonstrated in the size range relevant for many applications. The ability to tailor local composition and/or shape of these granular precursors may lead to enhanced packing efficiency[39] and novel applications ranging from ceramics fabrication to pharmaceutical materials.

2.5 References

1. Umbanhowar, P.B., V. Prasad, and D.A. Weitz, *Monodisperse Emulsion Generation via Drop Break Off in a Coflowing Stream.* Langmuir, 2000(16): p. 347-351.
2. Thorsen, T., *et al.*, *Dynamic Pattern Formation in a Vesicle-Generating Microfluidic Device.* Physical Review Letters, 2001. **86**(18): p. 4163-4166.
3. Anna, S.L., N. Bontoux, and H.A. Stone, *Formation of dispersions using "flow focusing" in microchannels.* Applied Physics Letters, 2002. **82**(3): p. 364-366.
4. Link, D.R., *et al.*, *Geometrically Mediated Breakup of Drops in Microfluidic Devices.* Physical Review Letters, 2004. **92**(5): p. 05403-1 - 05403-4.
5. Song, H., J.D. Tice, and R.F. Ismagilov, *A Microfluidic System for Controlling Reaction Networks in Time.* Angew. Chem. Int. Ed., 2003. **7**(42): p. 767-772.

6. Jeong, W.J., *et al.*, *Continuous Fabrication of Biocatlyst Immobilized Microparticles Using Photopolymerization and Immiscible Liquids in Microfluidic Systems.* Langmuir, 2005(21): p. 3738-3741.

7. De Geest, B., *et al.*, Langmuir, 2005. **21**(23): p. 10275-10279.

8. Dendukuri, D., *et al.*, *Controlled Synthesis of Nonspherical Microparticles Using Microfluidics.* Langmuir, 2005(21): p. 2113-2116.

9. Seo, M., *et al.*, *Continuous Microfluidic Reactors for Polymer Particles.* Langmuir, 2005. **21**(25): p. 11614-11622.

10. Seo, M., *et al.*, *Microfluidics: From Dynamic Lattices to Periodic Arrays of Polymer Disks.* Langmuir, 2005. **21**(11): p. 4773-4775.

11. Xu, S., *et al.*, *Generation of Monodisperse Particles by Using Microfluidics: Control over Size, Shape, and Composition.* Angew. Chem. Int. Ed., 2005(44): p. 724-728.

12. Roh, K.-H., D.C. Martin, and J. Lahan, *Biphasic Janus particles with nanoscale anisotropy.* Nature Materials, 2006. **4**: p. 759-763.

13. Dendukuri, D., *et al.*, *Continuous-flow lithography for high-throughput microparticle synthesis.* Nature Materials, 2006. **5**: p. 365-369.

14. Nie, Z., *et al.*, *Janus and Ternary Particles Generated by Microfluidic Synthesis: Design, Synthesis, and Self-Assembly.* J. Am. Chem. Soc., 2006. **128**: p. 9408-9412.

15. Nisisako, T., T. Torii, and T. Higuchi, *Novel microreactors for functional polymer beads.* Chemical Engineering Journal, 2004(101): p. 23-29.

16. Khan, S.A., *et al.*, *Microfluidic Synthesis of Colloidal Silica.* Langmuir, 2004. **20**(20): p. 8604-8611.

17. Yi, G.-R., *et al.*, *Generation of uniform photonic balls by template-assisted colloidal crystallization.* Synthetic Metals, 2003. **139**: p. 803-806.

18. Zhao, X.-M., Y. Xia, and G.M. Whitesides, J. Mater. Chem., 1997(7): p. 1069-1074.

19. Kenis, P.J.A., R.F. Ismagilov, and G.M. Whitesides, *Microfabrication Inside Capillaries Using Multiphase Laminar Flow Patterning.* Science, 1999. **285**(2): p. 83-85.

20. Utada, A.S., *et al.*, *Monodisperse Double Emulsions Generated from a Microcapillary Device.* Science, 2005. **308**(22): p. 537-541.

21. Nie, Z., *et al.*, *Polymer Particles with Various Shapes and Morphologies Produced in Continuous Microfluidic Reactors.* Journal of the American Chemical Society, 2005.

22. Vanapalli, S.A., *et al.*, *Fluidic Assembly and Packing of Microspheres in Confined Channels.* Langmuir, 2008. **24**: p. 3661-3670.

23. Dendukuri, D., *et al.*, *Stop-flow lithography in a microfluidic device.* Lab on a Chip, 2007. **7**: p. 818-828.

24. Garstecki, P., H.A. Stone, and G.M. Whitesides, *Mechanism for Flow-Rate Controlled Breakup in Confined Geometries: A Route to Monodisperse Emulsions.* Physical Review Letters, 2005. **94**(16): p. 164501.

25. Garstecki, P., *et al.*, *Formation of droplets and bubbles in a microfluidic T-junction - scaling and mechanism of break-up.* Lab On A Chip, 2006. **6**: p. 437-446.

26. Utada, A.S., *et al.*, *Dripping to Jetting Transitions in Coflowing Liquid Streams.* Physical Review Letters, 2007. **99**(094502): p. 1-4.

27. Clanet, C. and J.C. Lasheras, *Transition from dripping to jetting.* J. Fluid Mech., 1999. **383**: p. 307-326.

28. Park, J.-U., *et al.*, *High-resolution electrohydrodynamic jet printing.* Nature Materials, 2007. **6**: p. 782-789.

29. Abate, A.R., *et al.*, *Impact of inlet channel geometry on microfluidic drop formation.* Physical Review E, 2009. **80**(026310): p. 1-5.

30. Stone, Z.B. and H.A. Stone, *Imaging and quantifying mixing in a model droplet micromixer.* Physics of Fluids, 2005. **17**(063103): p. 1-11.

31. Zheng, B., S. Roach, and R.F. Ismagilov, *Screening of Protein Crystallization Conditions on a Microfluidic Chip Using Nanoliter-Size Droplets.* J. Am. Chem. Soc., 2003(125): p. 11170-11171.

32. Shepherd, R.F., *et al.*, *Microfluidic Assembly of Homogenous and Janus Colloid-Filled Hydrogel Granules.* Langmuir, 2006. **22**: p. 8618-8622.

33. Taylor, G.I., *The Formation of Emulsions in Definable Fields of Flow.* Proceedings of the Royal Society of London. Series A., 1934. **146**(858): p. 501-523.

34. Pan, G., R. Kesavamoorthy, and S.A. Asher, *Optically Nonlinear Bragg Diffracting Nanosecond Optical Switches.* Physical Review Letters, 1997. **78**(20): p. 3860-3863.

35. Verhaegh, N.A.M. and A.v. Blaaderen, *Dispersions of Rhodamine-Labeled Silica Spheres: Synthesis, Characterization, and Fluorescence Confocal Scanning Laser Microscopy.* Langmuir, 1994. **10**(5): p. 1427-1438.

36. Hansen, F.K. and G. Rodsrud, *Surface Tension by Pendand Drop I. A Fast Standard Instrument Using Computer Image Analysis.* Journal of Colloid and Interface Science, 1991. **141**(1): p. 1-9.

37. Pathak, J.A. and K.B. Migler, *Droplet-String Deformation and Stability during Microconfined Shear Flow.* Langmuir, 2003(19): p. 8667-8674.

38. Torquato, S., T. Truskett, and P. Debenedetti, *Is random close packing of spheres well defined?* Physical Review Letters, 2000. **84**(10): p. 2064-2067.

39. Donev, A., *et al.*, *Improving the Density of Jammed Disordered Packings Using Ellipsoids.* Science, 2004. **303**(13): p. 990-993.

2.6 Tables

Table 2.1 Experimental conditions for colloid-filled hydrogel granules production via microfluidic assembly.

Granule Composition/Shape	**Inlet Composition**			**Channel Width x Height (μm)**	
	[1]	[2]	[3]	[1,2,3,4]	[5]
Homogenous/Spherical Granules	FITC	FITC	OIL	100x150	220x150
Homogenous/Discoid Granules	RITC	RITC	OIL	100x75	220x75
Janus/Spherical Granules	FITC	RITC	OIL	100x150	220x150
Janus/Discoid Granules	FITC	RITC	OIL	100x75	220x75

2.7 Figures

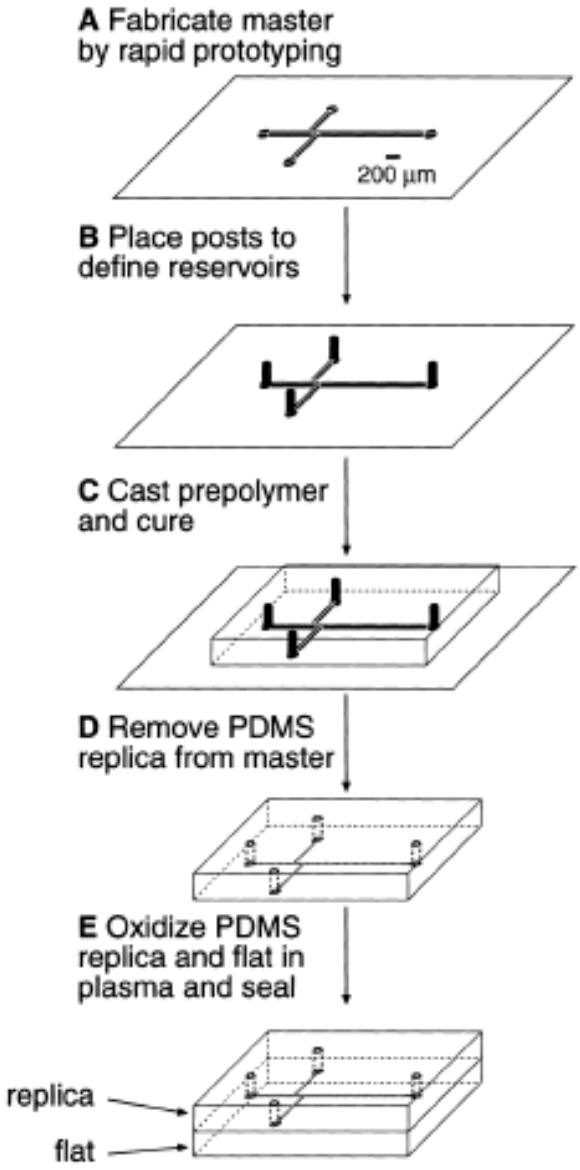

Figure 2.1 Schematic illustration of soft lithographic fabrication of poly(dimethyl siloxane) (PDMS) microchannels. (A) An SU-8 positive-relief pattern is created on a silicon wafer via photolithography. (B) In some cases, posts can be placed on the SU-8 pattern to incorporate holes into the (C) poured PDMS prepolymer. (D) The prepolymer is cured at elevated temperature and peeled off to reveal the relief pattern and holes built into the PDMS mold. (E) The mold and cured PDMS flat are oxidized in PDMS, forming silanol (SiOH) groups on the surface. The two pieces are then placed in conformal contact and allowed to interbond, forming sealed channels of PDMS.[18]

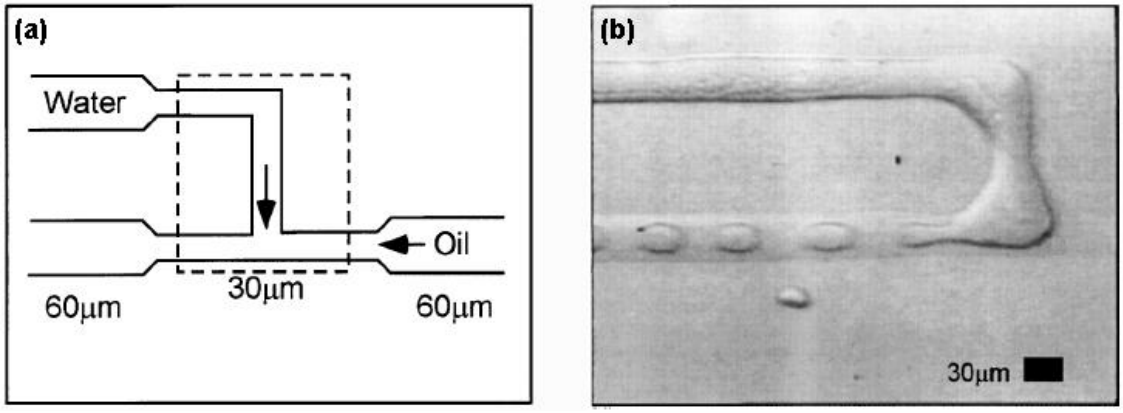

Figure 2.2 (a,b) An inverse emulsion of water in silicone oil is made by shearing an incident flow of water on a 90^{o} crossflow of silicone oil. b) Droplet formation in a microfluidic device. Channel dimensions for the water and silicone oil at point of incidence is 30 μm.

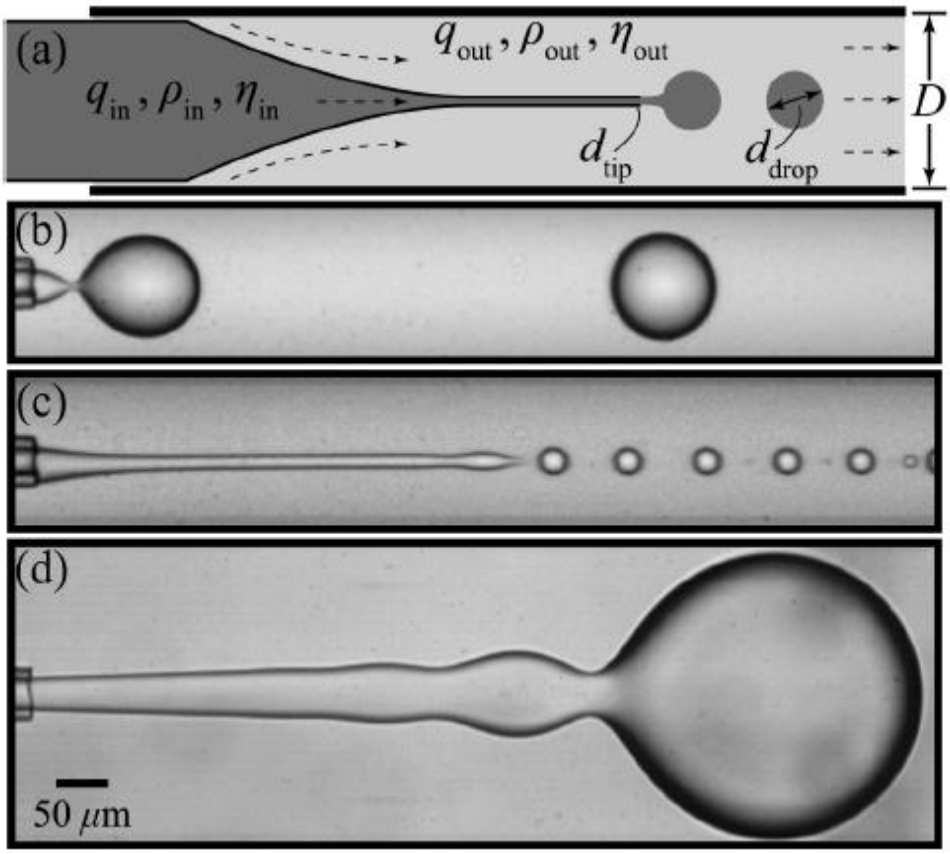

Figure 2.3 Drop breakup modes where (b) is dripping mode, (c) is an extensional jetting mode, and (d) is a widening jetting mode.[26]

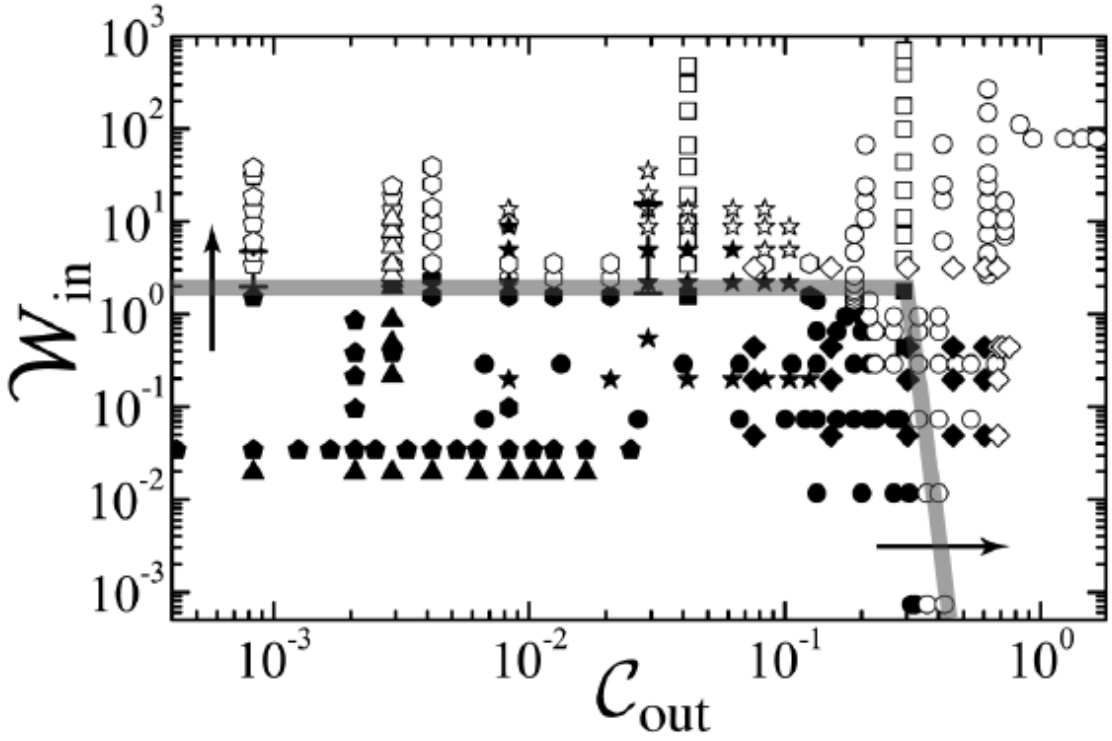

Figure 2.4 Plot of the inner fluid Weber number as a function of the outer fluid capillary number in a coaxial microcapillary device. Filled symbols denote drop formation via a dripping mode, whereas open symbols denote those formed by a jetting mode.[26]

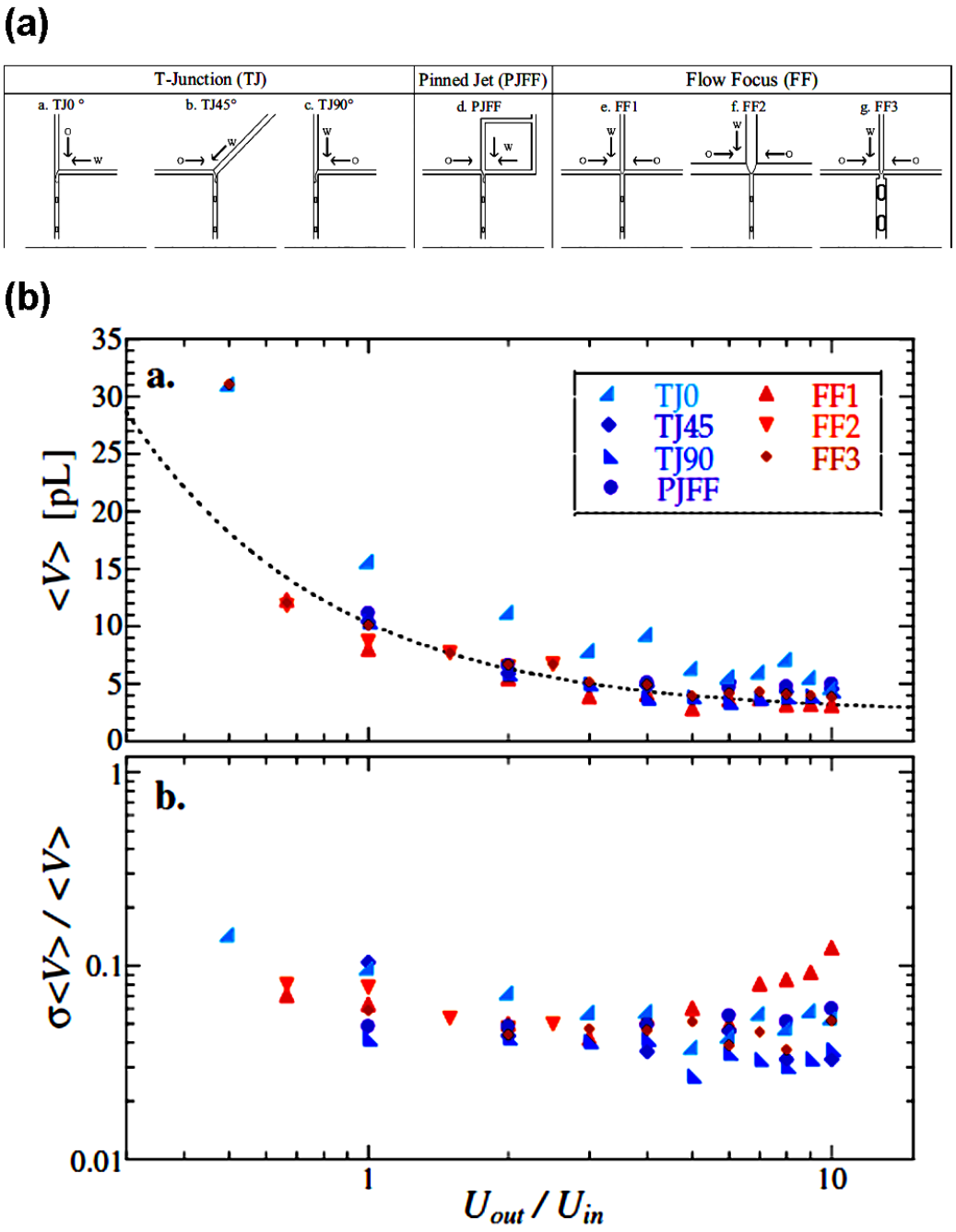

Figure 2.5 (b, top) Mean volumes of droplets formed at a *Ca* = 0.015 for TJ devices and *Ca* = 0.05 for FF devices described in (a). (b, bottom) Standard deviation of drops produced using the same conditions as (b, top).[29]

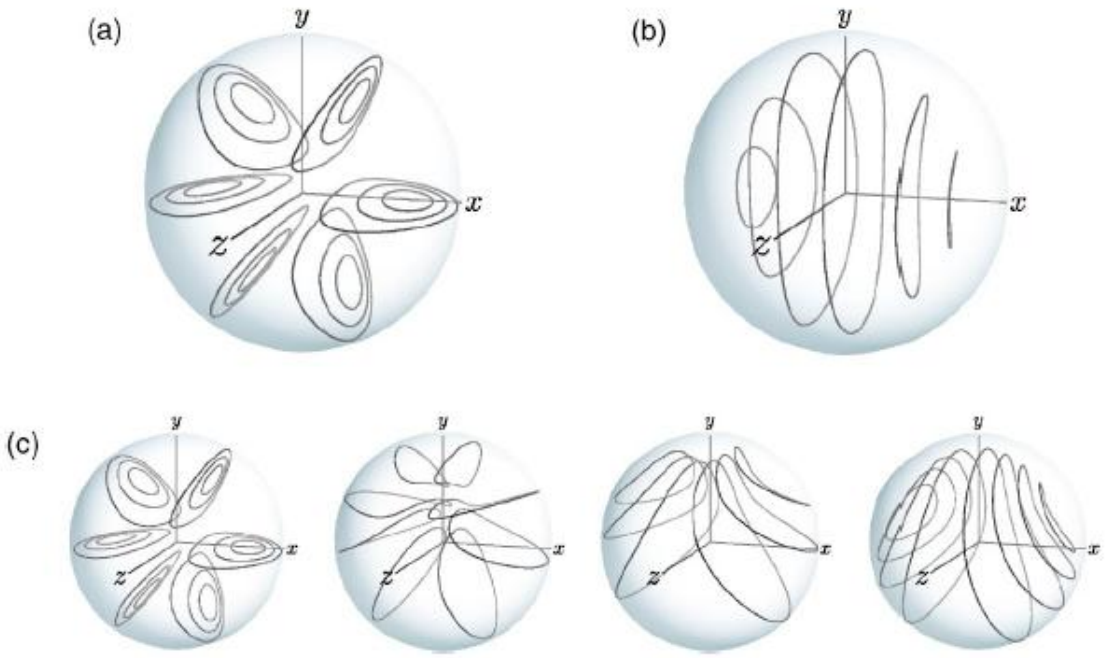

Figure 2.6 Simulation results of shear induced, recirculatory flow within liquid drops. The different shear environments are (a) hemispherically symmetric flow (b) axisymmetric flow and (c) variety of internal flow motifs demonstrating a break in symmetry under certain external flow conditions.[30]

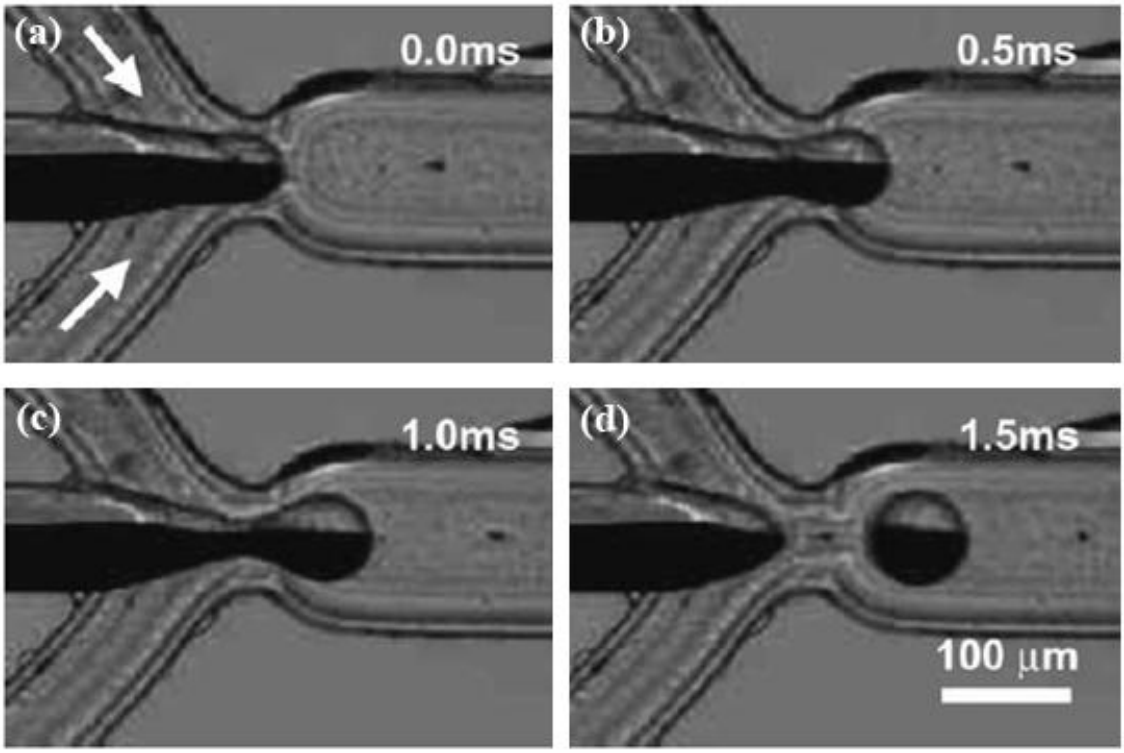

Figure 2.7 Axisymmetric flow focusing device coflowing two hydrophobic monomer streams into an external flow of an aqueous polyvinyl alcohol solution. (a-d) Stages of drop formation demonstrating no mixing of hemispheres during axisymmetric drop breakup at different times through the cycle.[15]

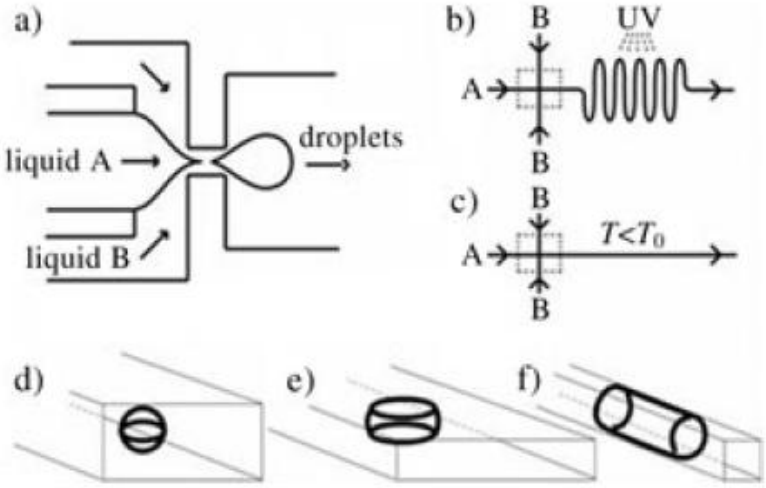

Figure 2.8 (a) Functional monomer droplet formation in a microfluidic flow focusing device prior to (b) UV irradiation and photopolymerization of the monomer droplet. (d) Sphere, (e) disk, and (f) rod formation via geometric confinement by microchannels.[11]

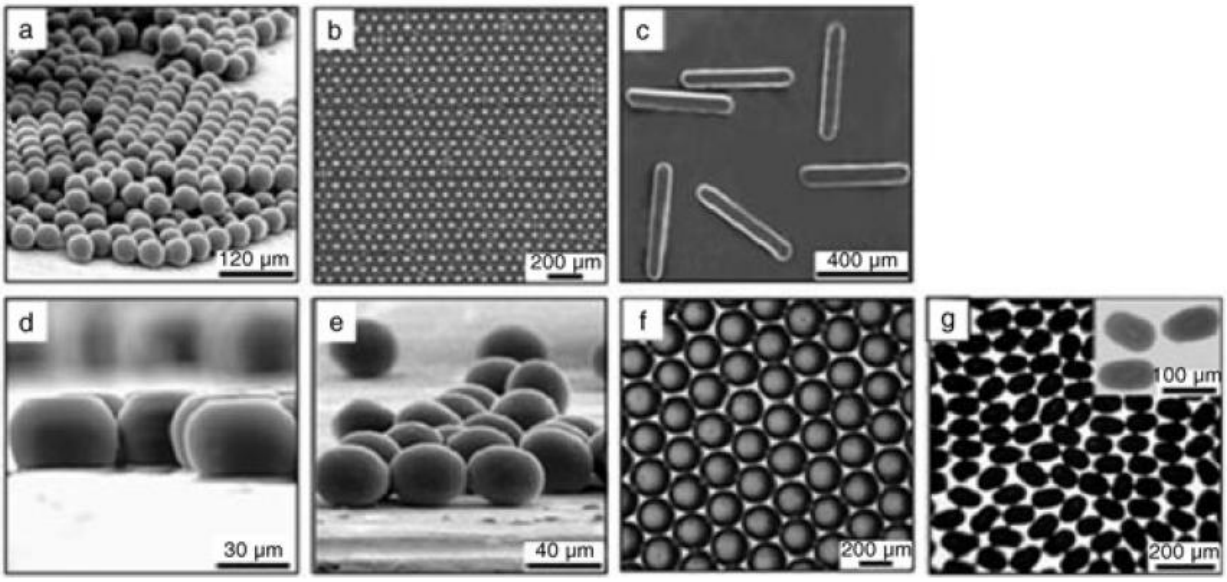

Figure 2.9 (a) Spheres and (b) crystalline lattice of spheres generated from the device architecture in **Figure 2.8a**. (c) Rod geometry generated from microfluidic architecture in **Figure 2.8f,** (d-g) disk shaped particles generated from device architecture in **Figure 2.8e**. Varying the channel dimensions creates different aspect ratios of rods and disks.[11]

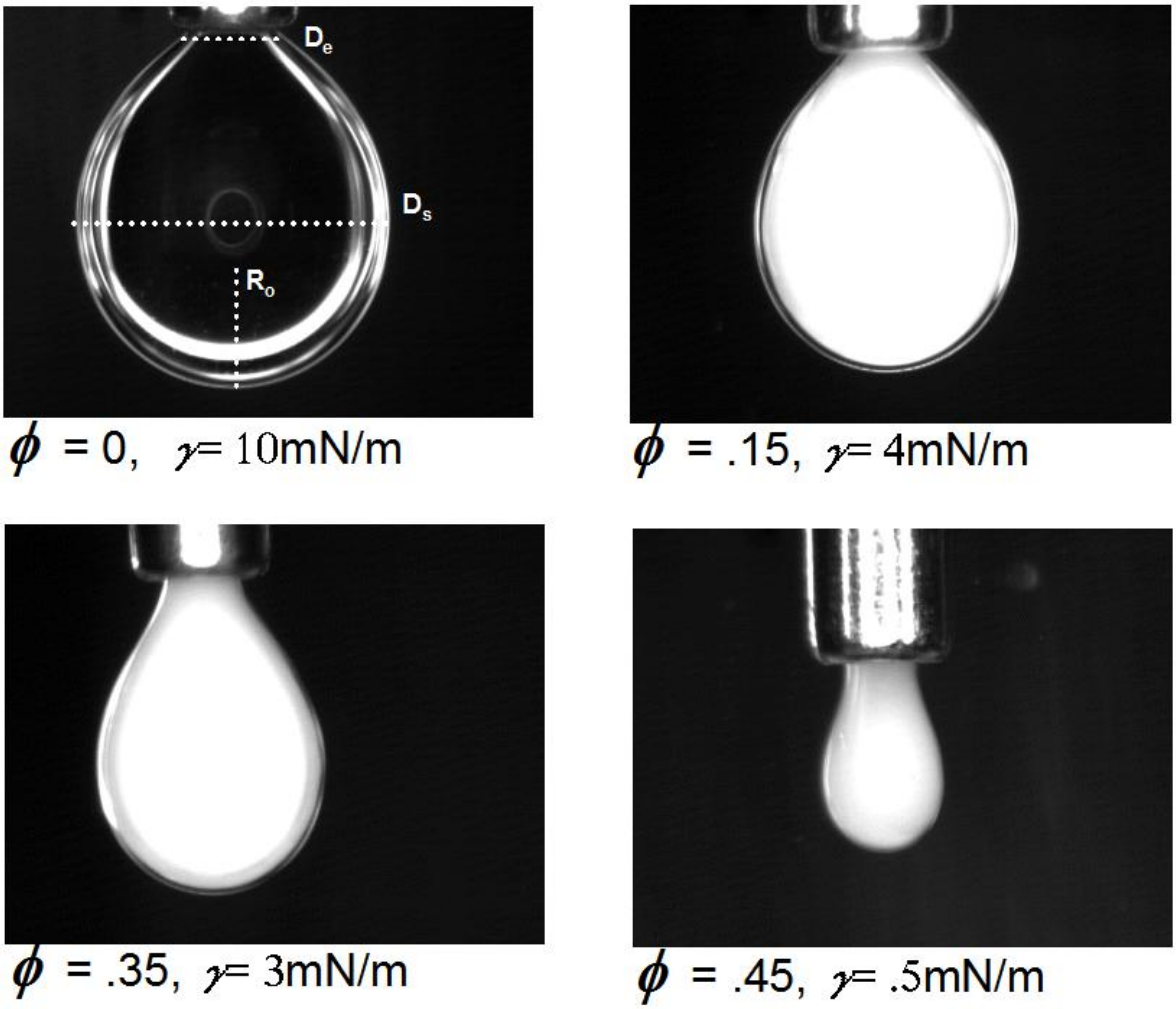

Figure 2.10 Axisymmetric drop shape analysis demonstrating the decreasing interfacial tension (left to right, top to bottom) as a function of increasing volume fraction (φ) of colloidal silica microspheres in an aqueous acrylamide solution. [Note: Drops are surrounded by mineral oil (black).]

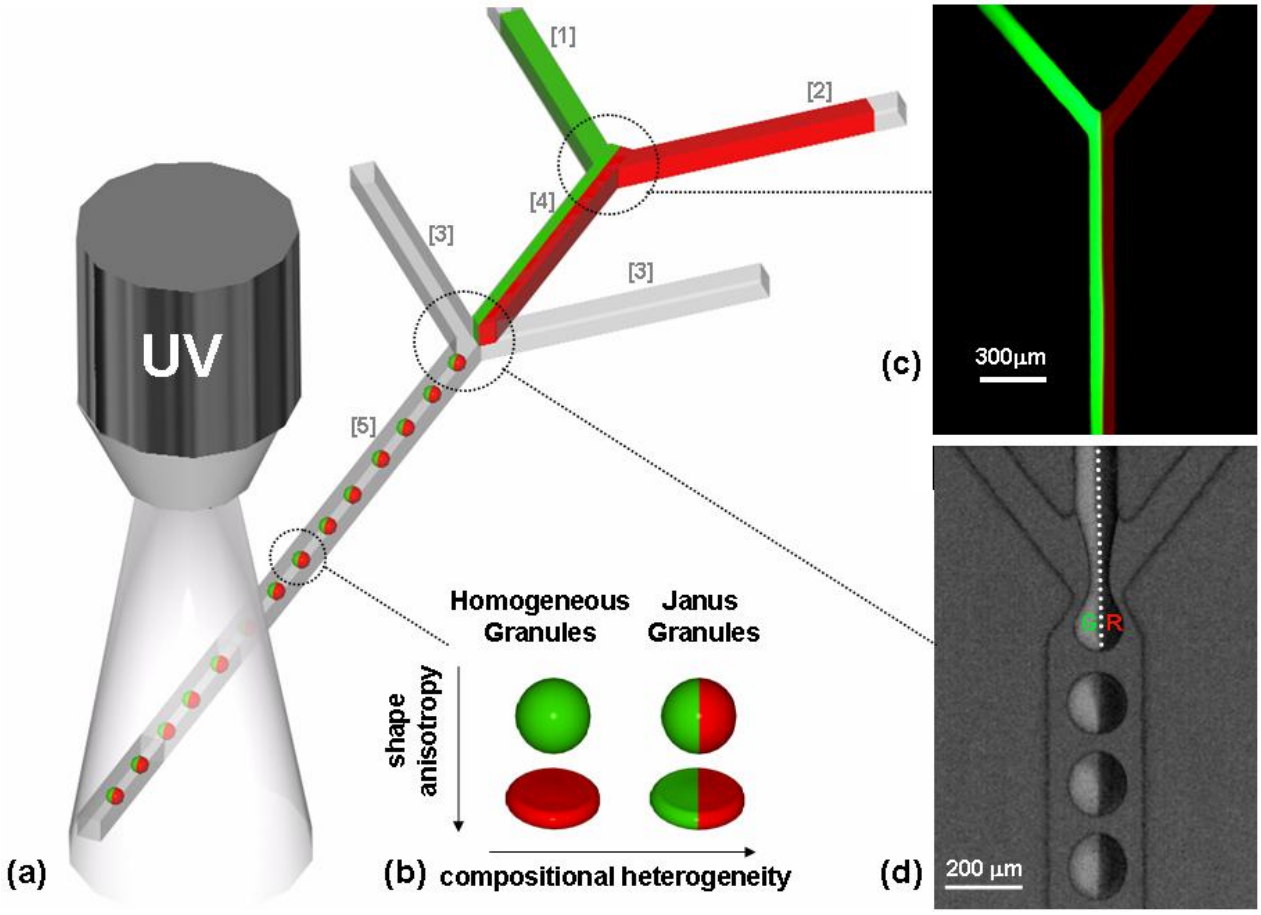

Figure 2.11 (a) Schematic representation of a sheath-flow microfluidic device used to produce monodisperse colloid-filled hydrogel granules, (b) schematic view of granule shapes and compositions explored, (c) fluorescent image of Y-junction formed by inlets [1] and [2] for the production of Janus spheres, and (d) backlit fluorescence image (green excitation) illustrating that the FITC-silica microspheres remain sequestered in the left hemisphere of each granule generated. [32]

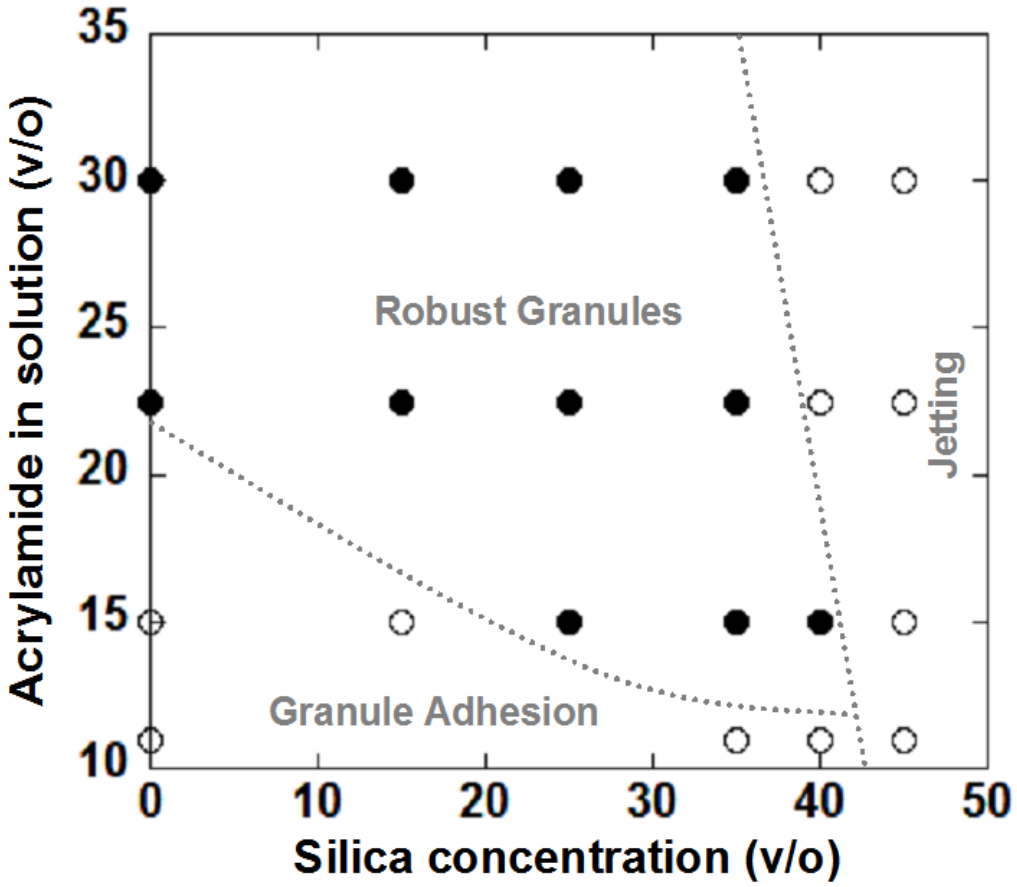

Figure 2.12 Processing phase diagram outlining the optimal region (filled symbols) for forming robust, monodisperse colloid-filled hydrogel granules from suspensions of varying composition with fixed photoinitiator concentration ($\varphi_{initiator}$ of 0.005 in suspension and $\varphi_{initiator}$ of 0.05 in oil) at short UV exposure times (~ 3 sec at an illumination intensity of 8000 mW/cm^2). [32]

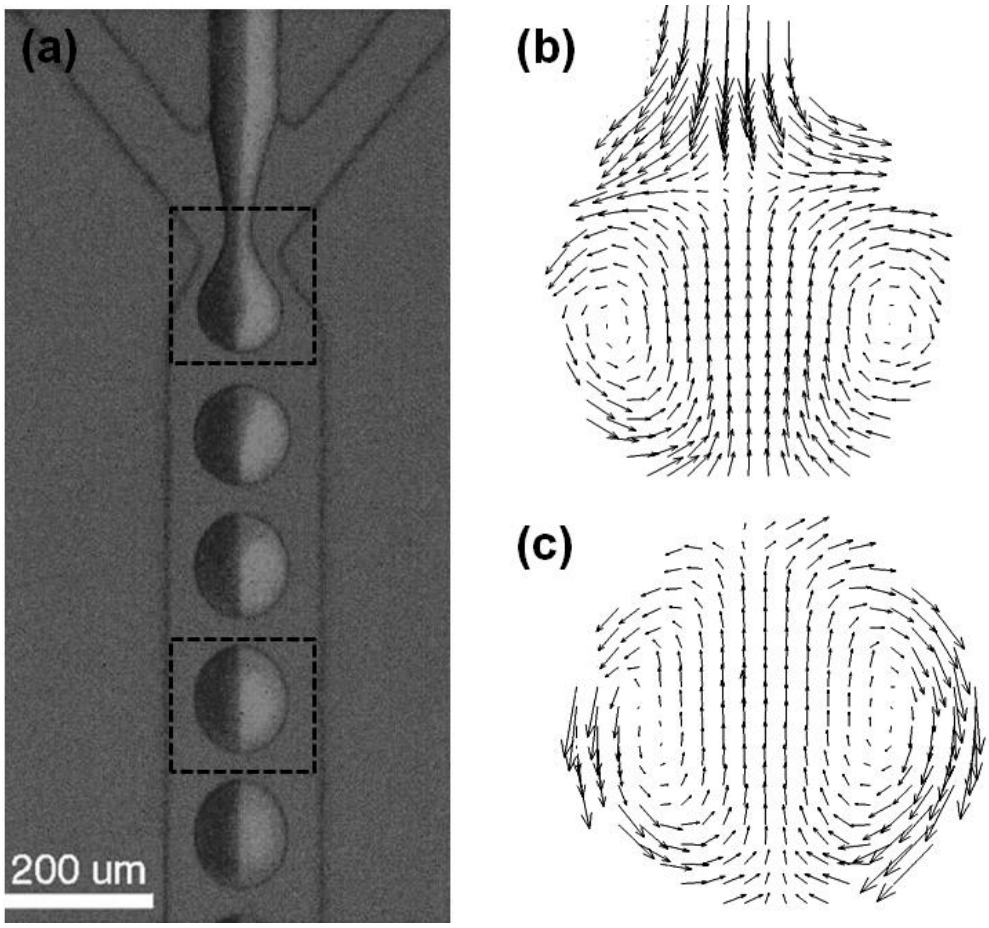

Figure 2.13 (a) Microfluidic Flow Focusing Device coflowing fluorescent silica (right) and non-fluorescent silica suspensions into an immiscible mineral oil to form hemispherically disting Janus drops of the colloidal suspensions. (b) Micro-Particle Imaging Velocimetry of the drop formation showing symmetric recirculation zones that (c) persist down the channel. [Dashed boxes correspond to locations where the PIV data was taken in (b,c)]

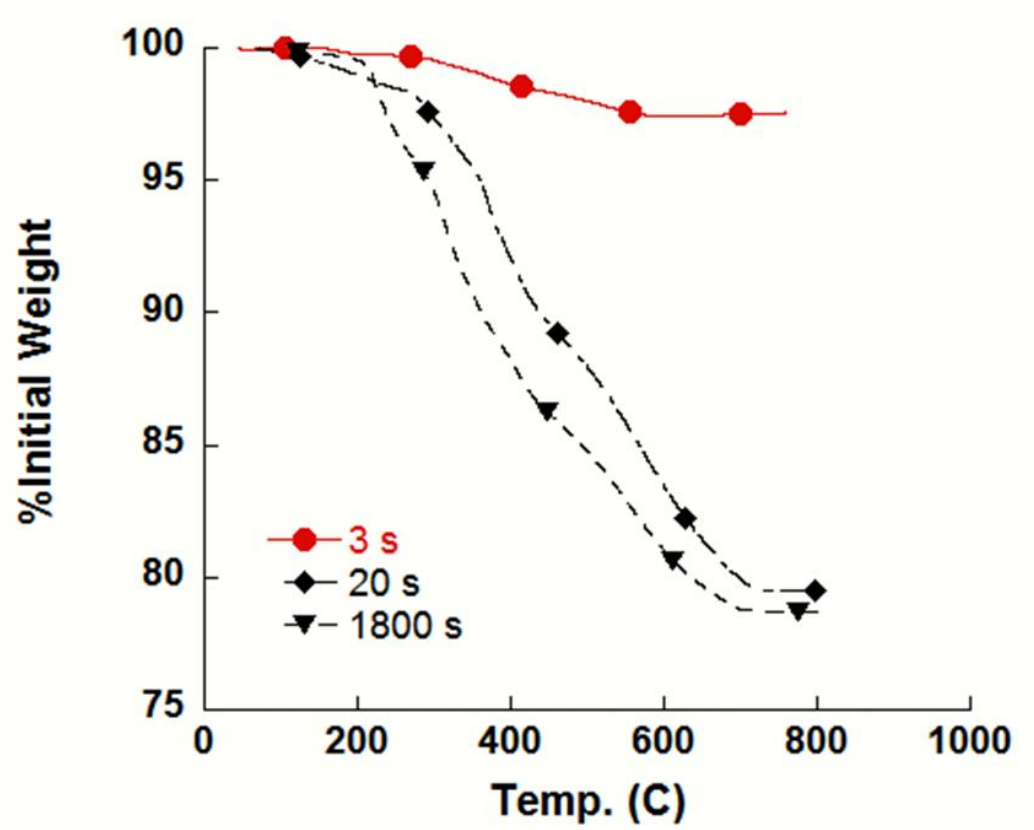

Figure 2.14 ThermoGravimetric Analysis of silica colloid filled hydrogel granules formed at varying exposure times, where the initial prehydrogel monomer concentration was ~20wt%. The data indicates that [red] 3 s exposure times result in a limited weight loss during burn off of the hydrogel and, thus, not all monomer is converted to hydrogel. Longer exposure times [black] demonstrate that a large degree of weight loss occurs, suggesting near total conversion of monomer to hydrogel at 20 s exposures and longer.

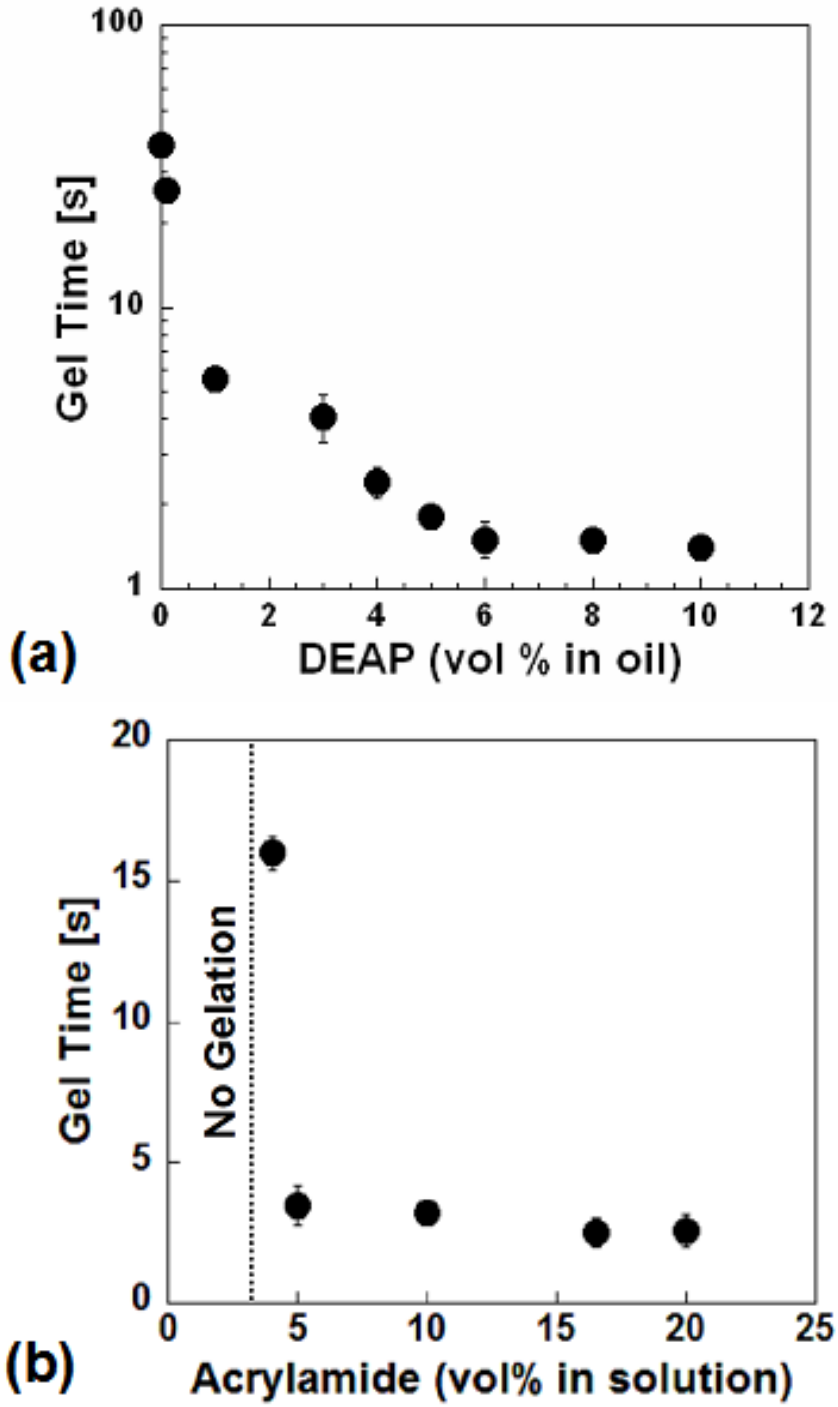

Figure 2.15 Granule gelation time as a function of (a) DEAP photoinitiator concentration in the oil phase at a fixed $\varphi_{acrylamide}$ of 0.165, and (b) acrylamide concentration at a fixed photoinitiator concentration ($\varphi_{initiator}$ of 0.005 in suspension and $\varphi_{initiator}$ of 0.05 in oil). Gelation is not observed for acrylamide concentrations below ~ 3 v/o, as indicated by the dashed line in (b).

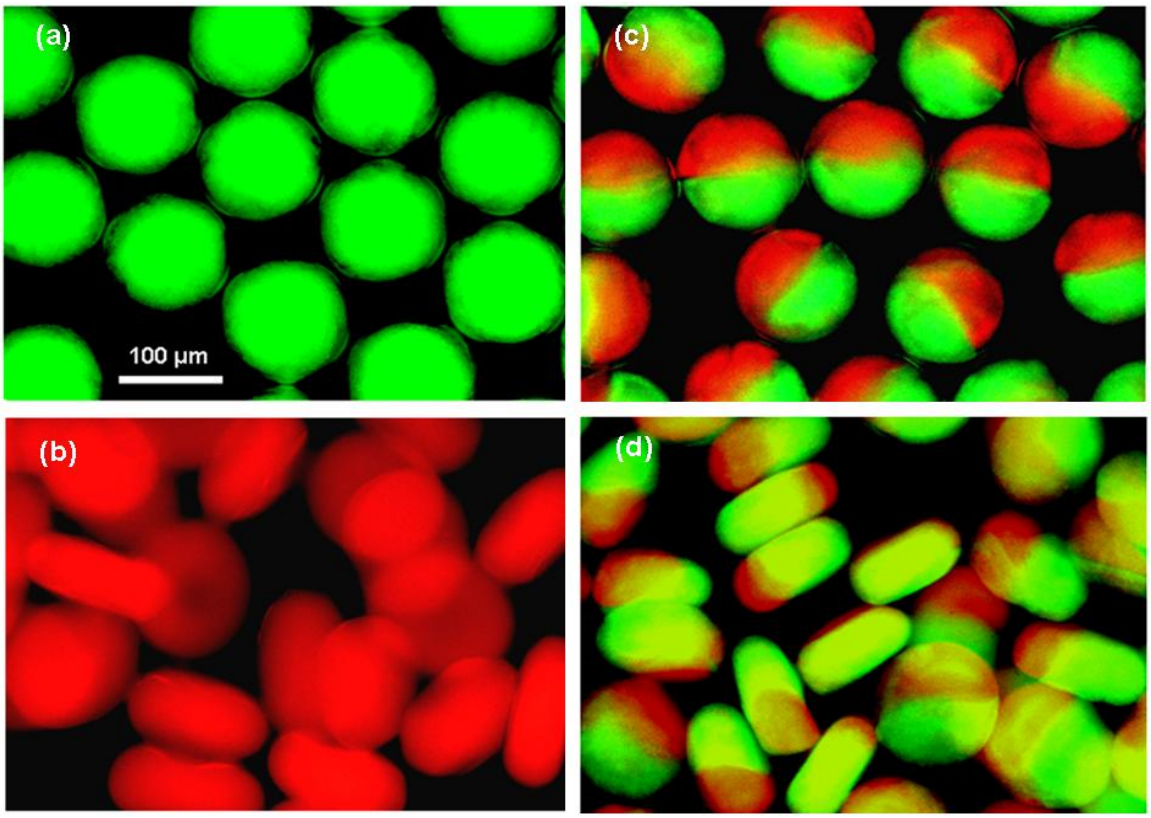

Figure 2.16 Fluorescence images of homogenous (a) spherical and (b) discoidal granules (in oil), and two-excitation fluorescence microscopy images of Janus (c) spherical and (d) discoidal granules (in oil). The images acquired from FITC- and RITC-excitations are overlaid in (c) and (d). Scale bars are identical for each image.

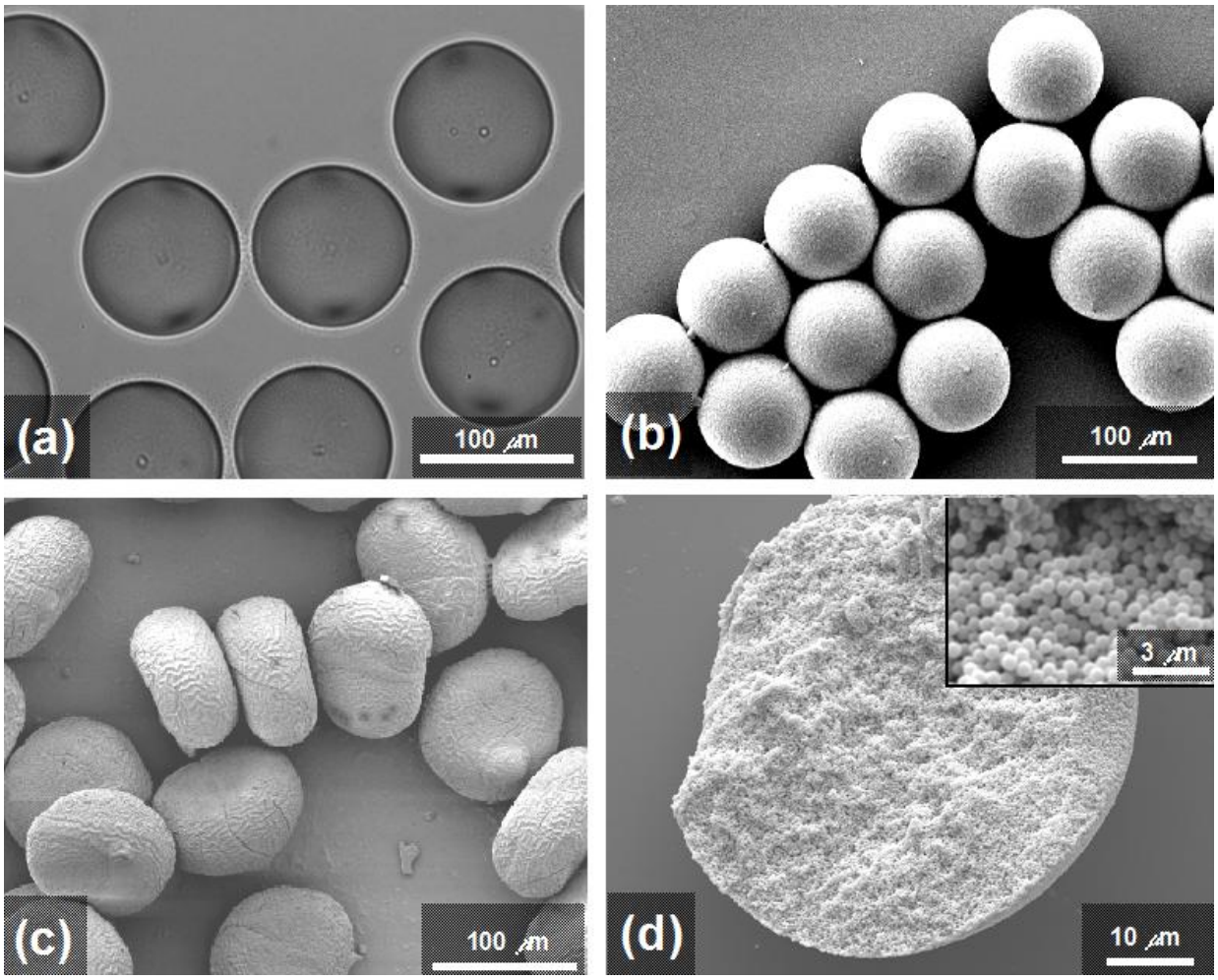

Figure 2.17 (a) Optical micrograph of pure hydrogel spheres (in oil), (b,c) scanning electron micrographs of dried spherical and discoid granules, and (d) scanning electron micrograph of a dried, freeze-fractured spherical granule. Inset (d) depicts a higher-magnification view of the random close-packed network of silica microspheres within the dried granule.

CHAPTER 3

MICROFLUIDIC PATTERNING OF COLLOIDAL, GLASS, AND SILICON MICROCOMPONENTS

3.1 Introduction

The assembly of oxide and non-oxide microcomponents from colloidal building blocks is central to a broad array of applications, including sensors,[1-3] optical devices,[4] and microelectromechanical systems (MEMS),[5-9] as well as to fundamental studies of granular materials.[10, 11] Progress in these areas has been hindered by the availability of colloidal microcomponents of precisely tailored size, shape, and composition. Thus, there is tremendous interest in developing new patterning methods for creating precisely tailored microcomponents composed of colloidal building blocks, amorphous or polycrystalline oxides, and silicon. For example, colloidal-based microcomponents produced in discoid, triangular, cuboid, or rectangular shapes, may serve as novel granular feedstock for ceramics,[12, 13] optical display technologies[4] and pharmaceuticals.[14, 15]

Traditional methods for producing colloidal granules, such as fluid bed granulation,[16] high shear mixer granulation,[17] and spray drying,[13] do not provide adequate control over granule size, shape, or composition. Equally important is the need to create porous and dense oxide and non-oxide microcomponents for functional devices ranging from micro-mixers and heat exchangers[18, 19] to MEMS.[5-9] Although several fabrication methods have been recently introduced, including lithography, electroplating and molding (LIGA),[20, 21] micro-extrusion,[22] micro-injection molding,[23, 24] micro-stereolithography,[25, 26] and micro-electro-discharge machining,[27] each lacks the materials flexibility or rapid assembly times desired for many applications.

Microfluidic assembly techniques provide a new platform for creating novel polymer particles from photopolymerizable resins[28-31] and hydrogels[32, 33] as well as colloidal granules, as discussed in Chapter 2.[34] In this chapter, we introduce and demonstrate its ability to produce a new technique, known as stop-flow lithography (SFL)[35] that can create a rich array of simple and complex colloidal granules and microcomponents at production rates in excess of 10^3 min^{-1}. SFL couples microfluidic control with microscope projection photolithography[36] in a microfluidic device,[35] as shown in **Figure 3.1**. The SFL devices are fabricated using soft-lithography.[37] SFL operates by first flowing a photopolymerizeable fluid, then stopping its flow, exposing the fluid to UV light that passes through a photomask to cure the desired shape(s), and then initiating flow to eject the photopatterned microparticle(s), as shown in **Figure 3.1b**.

The maximum throughput, T_s, of this process is defined by:

$$T_s = \frac{N_p}{t_{stop} + t_{polymerize} + t_{flow}}$$

where N_p is the number of particles formed in one exposure, t_{stop} is the time required for the fluid to cease forward motion, $t_{polymerize}$ is the exposure time of the fluid to UV light, and t_{flow} is the time allowed for the fluid to flow before stopping for the next exposure (usually a time long enough to clear the exposure area of particles). N_p is defined by the mask design and optics utilized. $t_{polymerize}$ is determined by the fluid chemistry, while t_{stop} is influenced by the material properties of the microchannel design.[35] **Figure 3.2** demonstrates that different microchannel thicknesses result in different values of t_{stop}. The t_{stop} dependence arises due to deformation of the

PDMS microchannel and the fluid viscosity, as shown in **Figure 3.3.** Specifically t_{stop} is related to [35]:

$$t_{stop} \propto \frac{\eta L^2 W}{E H^3}$$

where *L*, *W*, and *H* are the microchannel length, width, and height respectively, *E* is the modulus of the microchannel material (PDMS), and η is the photopolymerizeable liquid viscosity. To minimize t_{stop}, the microchannel length should be reduced, while its height should be maximized.

The use of PDMS devices for SFL is critical, as it gives rise to a simple oxygen quenching mechanism that limits free radical polymerization.[38] Because oxygen can freely diffuse to the channel interior, the microparticles are inhibited from sticking to the top or bottom surfaces of the PDMS microchannel, allowing multiple exposures at a single location, as shown in **Figure 3.4**.[38] Importantly, the oxygen inhibition layer decreases in thickness with time and thus, there is a maximum $t_{polymerize}$ before the microparticles will stick to the microchannel surfaces.

To date, SFL has been used to create Janus particles[39] and patterned microparticles for biomolecular analysis.[40] In addition, porous particles have been created by interference lithography.[41] In this chapter, we report the assembly of colloidal granules and microcomponents in the form of microgear, triangular, discoid, cuboid, and rectangular shapes using SFL as well as demonstrate pathways by which these building blocks can be transformed into both porous and dense oxide and non-oxide structures. To facilitate SFL, we designed a novel photopolymerizable colloid-filled hydrogel solution, in which the solvent system was nearly index matched with the silica microspheres. In addition, we optimized the microchannel geometry and suspension properties (solids loading and viscosity) to allow for high throughput.

3.2 Experimental Methods

3.2.1 Material System

Colloidal suspensions are prepared by first adding an appropriate amount of polyethyleneimine (PEI); (1800 g mol^{-1}); Aldrich Chemical Co to deionized water. The solution pH is then adjusted to 6 by adding aliquots of a 1M HNO_3 solution (Fisher Scientific). Following this, silica microspheres (ϕ_{silica} = 0.5, 500 ± 25 nm diameter, FUSO, Japan) are added to the solution and allowed to stir overnight to adsorb 0.5 mg PEI/m^2 silica[42]. This opaque suspension is then index-matched by the addition of dimethyl sulfoxide (DMSO; Fisher Scientific) to achieve a volumetric ratio of 65:35 v/v DMSO to water. The suspension is then concentrated by centrifuging at 3000 rpm. After the supernatant is decanted, a photoinitiator, ϕ_{init} = 0.03 (Darocur 1173, Ciba), acrylamide monomer, a 0.09 wt% (Acros Organics), and crosslinking agent N,N methylene bisacrylamide (Aldrich Chemical Co.) at an 8:2 w/w ratio of monomer to crosslinking agent is added to the dense sediment. The index-matching is finely tuned by adding deionized water to yield a final composition of ϕ_{silica} = 0.50, 62:38 v/v of DMSO:water, and 0.08 wt% acrylamide. Note, to facilitate direct visualization of representative patterned microcomponents, silica microspheres (ca. 700 nm in diameter) are synthesized with a fluorescent, rhodamine isothiocyanate (RITC) core-shell architecture following the procedure described in Ref. 41. A 1:9 number ratio of fluorescent to non-fluorescent silica is utilized in suspension. To quantify the extent of polymerization as a function of exposure time, we performed thermogravimetric analysis (TGA) (Pyris 6, Perkin-Elmer) on representative dried granules heated to 800°C at 10°C/min in air. The UV absorption properties of the system are determined by placing 2ml of 5v/o silica suspension or acrylamide solution into a quartz cuvette in a UV/Vis (UV-2401PC, Shimadzu) and measuring absorbance for a spectrum of 200nm to

600nm in increments of 1nm. Mie scattering simulations are performed using a freely available online routine provided by the Oregon Medical Laser Center, OMLC.[43]

3.2.2 Suspension Rheology

Viscometry measurements are carried out on suspensions of varying colloid volume using a controlled-stress rheometer (CVOR, Bohlin) equipped with a cup and bob geometry (C15 cell). Prior to taking measurements, a preshear of 50 s^{-1} is applied for 10 s and allowed to rest for 300 s before starting each experiment. We first measure the viscosity from a shear rate of 0.01 to 300 s^{-1} of a 50 v/o suspension, which is utilized in SFL. After this initial measurement, the suspension is diluted with the acrylamide solution, and the measurement is subsequently repeated for 45, 40, and 35 v/o suspensions.

3.2.3 Device Fabrication

Microfluidic devices are produced via soft lithography[37] by pouring PDMS (Sylgard 184; Dow Corning) onto a silicon wafer patterned with SU-8 photoresist features (SU-8 50; Microchem). After curing the PDMS, the mold is cut out and treated via UVO[37] with an accompanying PDMS coated coverslip. After treatment, the mold and coverslip are brought into conformal contact and allowed to bond, forming a monolithic structure. Although unnecessary, we protected the microchannel surfaces during UVO treatment following the procedure described in Ref. 43. The microchannel dimensions used in these experiments are: D = 1 mm, L = 1 cm, and H = 30 μm, 40 μm or 55 μm, which were obtained by spin-coating at either 3000, 2500, or 2000 rpm, respectively. Note, channel heights as low as 10 μm could be achieved at higher spin speeds. Photomasks are rendered with CAD (Autocad 2005 ®) and printed via a high-resolution laser printer (5080 dpi; CAD/Art Services, Inc.).

3.2.4 Stop-Flow Lithography

The transparent colloidal suspension (50 v/o silica) is flowed into the microfluidic device in a pulsed sequence and synched with flashes of UV exposure, as described in Ref. 43. By applying a voltage to a solenoid valve through software written in Labview©, the suspension is flowed at 2 psi for 400 ms, the pressure is then stopped by removal of the applied voltage. After the pressure is released, the system is allowed to relax for 300 ms, during which time the fluid comes to a full stop. Immediately after flow ceases, UV light is projected through a photomask into an objective lens (20X, N.A. 0.46; Zeiss) that focuses the negative mask image onto the microchannel for a periods of 200 ms or 400 ms, depending on the extent of reaction desired for polymerization and crosslinking of the acrylamide solution. This process is repeated until the desired number of microcomponents is formed.

3.2.5 Particle Tracking

A concentrated colloidal suspension ($\phi_{silica} = 0.5$) that contains a dilute amount ($\phi =$ 0.001) of 1.6 μm latex beads (Sulfate modified; A37297; Invitrogen) is flowed through representative microchannels that are 1 mm wide, 1 cm long, and 40 μm thick. A pressure of 2 psi is applied for 1 s and turned off for 2 s, before repeating the cycle. A high-speed camera (Phantom V7.1) is used to record video at a frame rate of 700 fps through an objective lens (60X oil immersion; Olympus). Particle tracking algorithms developed by Crocker and Grier for IDL[44] are used to track a single particle at the center of the microchannel, ~20 μm into the channel depth, near the output to determine the particle position within each frame. The particle velocity is determined using the forward difference method between frames.

3.2.6 Thermal Processing

Representative colloidal microcomponents are harvested from the SFL device, dried, and then densified on a sapphire window (Edmunds Optics) by heating at 1^{o}C/ min to 1150^{o}C for varying hold times of 1, 3, or 10 h before cooling to ambient temperature at a rate of 1^{o}C/min. Porous and dense glass (silica) microgears are produced depending on the hold time employed. Note, dense zirconia substrates are used for samples, when substrate transparency is not required.

3.2.7 Silicon Replication

Porous glass microgears are transformed into silicon replicas by a magnesiothermic reduction process.[45] Each microgear is placed on a silicon substrate within a low carbon (1010) steel boat. The source of magnesium vapor, Mg_2Si powder (99.5% purity, Alfa Aesar) (0.3 g), is placed at the other end of the steel boat at a distance of 1 cm from the microgear. The steel boat is placed within a steel ampoule (2.5 cm in diameter, 15.2 cm in length) that is then welded shut in an argon atmosphere. The ampoule is heated at a rate of 7^{o}C/ min to 850^{o}C and held at this temperature for 2.5 h to allow the magnesium vapor to fully react with the porous silica microgear to yield a mixture of magnesium oxide and silicon. After cooling to room temperature, the reacted gear is removed from the ampoule and then immersed in an hydrochloric acid (HCl) solution (HCl:H_2O:EtOH molar ratio of 0.7:4.7:8.9) for 4 h at room temperature to selectively dissolve MgO yielding the desired nanoporous silicon microcomponents.

3.2.8 Microcomponent Characterization

Representative colloidal microcomponents that contain fluorescent-core silica microspheres are harvested from the SFL device, dried, and then immersed in a 65:35 DMSO:water solution prior to imaging with a confocal scanning fluorescence microscope (SP2

Multiphoton, Leica) equipped with an argon laser (excitation wavelength of 514 nm). Confocal *x-y* scans are acquired at 0.765 μm intervals in the *z*-direction through a given microcomponent. The images are then compiled into a 3D rendering using Amira © imaging software and the *x*, *y*, and *z* values given from the confocal images. Representative colloidal, glass, and nanoporous silicon microcomponents are imaged using scanning electron microscopy (SEM) (6060 LV, JEOL). Energy dispersive x-ray analysis (EDX) (ISIS, Oxford Instruments) is performed on replicated silicon microgears to verify complete reaction and MgO dissolution conversion. In addition, surface roughness measurements are carried out using atomic force microscopy (AFM) (MFP-3D; Asylum Research). These data are acquired by probing three 25 μm^2 areas selected randomly. The root-mean-squared, RMS, roughness values are calculated by taking an average of each data set after applying a 3rd degree polynomial flatness convolution algorithm.

3.3 Results and Discussion

We demonstrate this novel assembly method by first designing a model colloidal suspension capable of being rapidly polymerized via projection lithography within a microfluidic device. The system is composed of silica microspheres suspended in a mixture of dimethyl sulfoxide (DMSO) and water at a volume fraction, ϕ_{silica}, of 0.5 and contains acrylamide monomer, a cross-linking agent, and photoinitiator. Pure aqueous silica suspensions are opaque due to the refractive index difference between silica (n = 1.46) and water (n = 1.33). By adding an appropriate amount of DMSO (n = 1.48), a transparent suspension is produced in which scattering from the suspended particles is minimized.

We utilized the SFL setup shown in **Figure 3.5a**, which operates to that in **Figure 3.1a**. Patterned microcomponent(s) are formed by projecting ultraviolet light through a photomask inserted into the field stop of an inverted microscope. Microcomponent fabrication involves the

stop-polymerize-flow sequence[46] captured in optical images shown in **Figure 3.5b-d**. **Figure 1b** shows an image of a suspension-filled microchannel prior to UV polymerization. The suspension is transparent due to its index-matched state. **Figure 3.5c** is acquired immediately after photopolymerization and shows a colloidal microgear that consists of a polyacrylamide network filled with silica microspheres and the solvent mixture. The modest change in refractive index upon polymerization enables one to visualize the as-patterned structure within the microchannel. Finally, **Figure 3.5d** shows the microgear as it accelerates in response to the onset of an applied pressure within the microchannel.

To minimize microcomponent shrinkage during drying, we used suspensions with high solids loading (ϕ_{silica}= 0.5) that are capable of flowing through the SFL device without clogging. The photopolymerizable suspensions exhibit Newtonian flow behavior when ϕ_{silica} < 0.35 (data not shown). At ϕ_{silica} ~ 0.35, there is a transition to shear thinning behavior, which becomes more pronounced with increasing ϕ_{silica} (**Figure 3.6a**). This behavior facilitates their flow through the SFL device at modest applied pressures.

We carried out particle tracking measurements for index-matched suspensions of varying colloidal volume fraction to obtain centerline velocities (**Figure 3.6b**). We estimate characteristic shear rates, which range from 40 to 200 s^{-1}, for colloidal suspensions of ϕ_{silica} = 0.5-0.35, respectively, by dividing the maximum centerline velocity by half the microchannel height. Over this shear rate range, each suspension can be approximated to first order as a Newtonian fluid (**Figure 3.6a**). The centerline velocity at the exit of a low aspect ratio (H/W <1) deformable PDMS microchannel is estimated by equation 3:[46, 47]

$$V(L) = \frac{H^3 E}{32 W \eta L}\left[\left(1+\frac{PW}{EH}\right)^4 - 1\right]$$

where E is the Young's modulus of PDMS (1MPa). These estimated velocities shown in **Table 3.1** are in good agreement with the measured maximum centerline velocities.

SFL consists of three distinct steps – stop, polymerize, and flow – repeated in a cyclical fashion;[46] hence, t_{stop}, $t_{polymerize}$, and t_{flow} are key experimental parameters. We determine the values for t_{stop}, which range from 100 to 300 ms for colloidal suspensions of ϕ_{silica} = 0.5-0.35, respectively, from the particle tracking data shown in **Figure 3.6b**. In our experiments, we use a value of 300 ms for t_{stop}, which is sufficient to ensure complete cessation of suspension flow prior to polymerization. We employ values of $t_{polymerize}$ that vary from ~ 200–400 ms depending on the mask design, which enable microcomponents to be patterned with precise control over their shape and size. Finally, a t_{flow} value of 400 ms is used, which is sufficient to expel the patterned microcomponent from the field of view thus preventing its double exposure.

Unlike the spherical colloidal granules produced by droplet-based microfluidic methods, whose shapes are defined by minimization of surface energy (see Chapter 2), the objects patterned via SFL are defined by the photomask that shapes the projected UV light. To best replicate the photomask features in the colloidal suspension, the fluid must display minimal scattering at the appropriate UV wavelength (~365 nm), allow transmission of UV light through the thickness of the microchannel, and polymerize the monomer rapidly to achieve high throughput. By using the index-matched system shown in **Figure 3.7a**, the polymerization kinetics are enhanced. **Figure 3.7b** reveals a much higher conversion efficiency for this system relative to the pure aqueous (opaque) suspension for a given exposure time of 3 s.

The photoinitiator used in these experiments is optimized for absorption at ~365nm; thus, at this wavelength, the projected UV light should penetrate the full thickness of the microchannel. Even though the index-matched suspension is transparent at visible wavelengths,

there is significant adsorption (64%) at ~365 nm (see **Figure 3.8a**). By contrast, however, there is nearly complete adsorption at a wavelength of 365 nm for the pure aqueous suspension. The absorption at 365 nm for index matched suspensions, however, is less than the near complete absorption of 365 nm light for a non-index matched suspension, **Figure 3.8a**.

Another important consideration is that Mie scattering is reduced when the index of refraction of the medium is similar to that of the particles themselves[48]. Through simulation, **Figure 3.8b**, we observe that suspensions of 500nm spherical particles with n = 1.46 (silica) suspended in a medium of n = 1.33 (water) show increased scattering over 500nm spherical particles of n = 1.46 suspended in an index-matched medium. By fine tuning the suspension chemistry for photopatterning, we can replicate patterns with excellent fidelity down to feature sizes of 10μm using standard microscope optics at a magnification of 20X, **Figure 3.9**.

To demonstrate the flexibility of this patterning technique and suspension composition, we produce colloidal microcomponents in both simple and complex shapes, **Figure 3.10**. Specifically, we assemble microcomponents with geometries that vary from triangular, cuboid, discoid and rectangular shapes to more complicated geometries, such as microgears, with uniform sizes that range from 20 μm to 300 μm in maximum dimension. Microcomponents composed of simple geometric forms are polymerized for shorter times, because they are able to withstand the modest deformation that occurs during ejection from the microchannel. By contrast, the complex microgears require the longest $t_{polymerize}$ (400 ms) to produce rigid structures that maintain their shape during ejection. This $t_{polymerize}$ was long enough to assure rigid mechanical properties, yet short enough to maintain an oxygen inhibition layer sufficient to prevent sticking to the PDMS microchannel surface. After production, because the microcomponents remain immersed in an index-matched solution, they appear translucent in the

optical images depicted in **Figure 3.10**. The microcomponent production rates for the 2x2 and 4x1 photomask arrays are approximately 240 min^{-1} for simple shapes and 200 min^{-1} for gears.

We investigate the distribution of colloidal microspheres within the polymerized microcomponents using a combination of confocal scanning microscopy, CLSM, and scanning electron microscopy (SEM). **Figure 3.11a** shows a confocal image (*x*-*y* scan) acquired at depth of 20 μm into a representative microgear in which 10% of the silica microspheres contain fluorescent cores. Both the *x*-*y* and *x*-*z* scans reveal that the microspheres are randomly distributed throughout these microcomponents. From this data, we find that the microgear thickness is approximately 50 μm. Since photopolymerization occurred within a 55 μm deep microchannel, we believe that inhibition layers no more than a few microns thick form at the interfaces between the suspension and microchannel. Their presence facilitates microcomponent ejection once suspension flow is reinitiated. Importantly, the colloidal microgears maintain their shape after being harvested from the microfluidic device and dried, as shown in the SEM images provided in **Figure 3.11b-c**. The tilted image, **Figure 3.11b**, clearly demonstrates that the photomask features can be replicated with a high degree of precision, while the corresponding high magnification view reveals that the colloidal microspheres are densely packed together with a final solids volume fraction of 0.62, as determined from the net shrinkage that occurs during drying. The inner and outer radii of the dried microgears are 95 ± 3 μm and 225 ± 3 μm, respectively.

To enhance their structural integrity, the colloidal microgears are transformed into fully dense, glassy silica microgears by sintering at 1150^{o}C for 3-10 h. SEM images of a sintered glass microgear are shown in **Figure 3.12a-b**. During densification, the microgear undergoes significant radial shrinkage (~25%) resulting in the final dimensions of 71 ± 1 μm (inner radius)

and 164 ± 4 μm (outer radius). Because the microcomponents are sintered on a transparent sapphire window, we can also image them via transmitted light microscopy. After sintering at 1150^{o}C for 3 h, the microgears are translucent. However, their surface remains rough on the size scale of the individual microsphere building blocks. At longer hold times (~10 h) the surface of the microgears becomes smooth. Their root-mean-squared (rms) surface roughness is approximately 6 nm, as determined by atomic force microscopy, **Figure 3.12c**.

Porous silica microgears are produced by partial sintering at 1150^{o}C for 1 h, as shown in **Figure 3.12d-e**. These microcomponents are mechanically stable and can be readily handled. Their rms surface roughness is ~ 130 nm, **Figure 3.12f**, due to the significant amount (23% by volume) of interconnected porosity that is retained after heat treatment. This porosity aids their transformation to porous silicon microcomponents via magnesiothermic reduction.[45] In this process, the silica microgears are heated to 850°C for 2.5 h in the presence of magnesium gas volatilized from Mg_2Si powder to promote the following reaction:

$$2Mg(g) + SiO_2(s) \longrightarrow 2\ MgO(s) + Si(s)$$

The MgO/Si composite generated by this reaction retains its 3D shape and porous features. The MgO/Si composite replicas are then immersed in a hydrochloric acid solution for 4 h to selectively dissolve the oxide phase yielding the desired porous silicon microgear replicas shown in **Figure 3.12g-h**. Energy dispersive x-ray analysis (EDX) reveals the presence of a strong silicon peak with a minimal oxygen peak, **Figure 3.12i**. The resulting silicon replicas contain two distinct pore size distributions, one associated with the interstices between the partially sintered silica microspheres and the other associated with the "ghost" microspheres on a finer scale, where each microsphere contains 65 v/o interior porosity based on the assumption of complete conversion to silicon and removal of MgO. These porosities, combined with the 5%

volumetric increase observed during the microcomponent conversion process result in a final silicon volume fraction of 0.27. Note, the silicon content could be enhanced significantly through an additional process, such as chemical vapor deposition.[5] The rms surface roughness of the porous silicon microgears is 118 nm, in good agreement with the surface roughness of the porous silica structures from which they are replicated. These values scale with the colloid size; hence, further improvements are possible by simply reducing the mean diameter of the colloidal building blocks utilized in suspension.

3.4 Conclusions

We have patterned silica-based microcomponents with a diverse array of geometric shapes, compositions, and physical properties with overall dimensions that range from approximately 10 μm to 1 mm at rates that exceed 10^3 min^{-1} using the SFL technique. Colloidal microcomponents may be used as novel granular media for fundamental studies of flow, packing, and compaction behavior. Recent efforts have shown that significant packing enhancements are observed simply by changing their shape from spherical to ellipsoidal granules.[49] Now, the possibility exists to explore such effects over a much broader range of granular shapes. Moreover, one can create granular building blocks with increasing chemical complexity by coflowing multiple suspensions of varying composition within the microfluidic device. For example, utilization of granular feedstock with Janus[34, 50] or other patchy motifs[51, 52] would enable the fabrication of more sophisticated ceramic components with nearly periodic compositional variations. We have also demonstrated that the patterned colloidal microcomponents can be converted to functional structures by densifying them at elevated temperature or via novel chemical conversion and replication schemes. As one example, porous silicon microcomponents may find potential application as gas sensors,[45] photoluminescent

materials,[53, 54] or MEMS devices. In related work, porous silicon structures replicated from biologically engineered silica "microcomponents" i.e. diatom frustules, have been shown to exhibit both rapid response times and high sensitivity to gases, such as nitrous oxide.[45] Finally, given their reduced contact area and weight, they should exhibit reduced *in-use* stiction[55] and require less power for actuation in MEMS applications.

3.5 References

1. Pan, Z., Z. Dai, and Z. Wang, *Nanobelts of semiconducting oxides.* Science, 2001. **291**(5510): p. 1947-1949.
2. Varghese, O.K., *et al., Extreme changes in the electrical resistance of titania nanotubes with hydrogen exposure.* Adv. Mater., 2003. **15**(7-8): p. 624-627.
3. Kim, I.-D., R. Avner, and C.Y. Lee, *Ultrasensitive Chemiresistors Based on Electrospun TiO2 Nanofibers.* Nano Letters, 2006. **6**(9): p. 2009-2013.
4. Chen, Y., *et al., Flexible active-matrix electronic ink display.* Nature, 2003. **423**(6936): p. 136-136.
5. Gratson, G.M., *et al., Direct-write assembly of three-dimensional photonic crystals: Conversion of polymer scaffolds to silicon hollow-woodpile structures.* Adv. Mater., 2006. **18**(4): p. 461-465.
6. Lehmann, O. and M. Stuke, Science, 1995. **270**: p. 1644-1646.
7. Schuster, R., V. Kirchner, and P. Allongue, *Electrochemical Machining.* Science, 2000. **289**(5476): p. 98-101.
8. Desbiens, J.-P. and P. Masson, *ArF excimer laser micromachining of Pyrex, SiC and PZT for rapid prototyping of MEMS components.* Sensors and Actuators A, 2007(136): p. 554-563.
9. Klajn, R., *et al., Plastic and moldable metals by self-assembly of sticky nanoparticle aggregates.* Science, 2007. **316**(5822): p. 261-264.
10. Mehta, A., *et al., Competition and cooperation: aspects of dynamics in sandpiles.* J. Phys.: Condens. Matter, 2005. **17**: p. S2657 - S2687.
11. Aste, T., *Variations around disordered close packing.* J. Phys.: Condens. Matter, 2005. **17**: p. S2361-S2390.

12. Lewis, J.A., Journal of the American Ceramics Society, 2000. **83**(10): p. 2341-2359.

13. Lukasiewicz, S.J., *Spray-Drying Ceramic Powders.* J. Am. Ceram. Soc., 1989. **72**(4): p. 617-624.

14. Collins, F.S. and V.A. McKusick, *Implications of the Human Genome Project for medical science.* Jama-Journal of the American Medical Association, 2001. **285**(5): p. 540-544.

15. York, P. and P.V. Marshall, *An investigation of the effect of the punch velocity on the compaction properties of ibuprofen.* Powder Technology, 1993(74): p. 171-177.

16. Cryer, S.A., *Modeling Agglomeration Processes in Fluid-Bed Granulation.* AIChE Journal, 1999. **45**(10): p. 2069-2078.

17. Darelius, A., *et al.*, *High shear wet granulation modelling--a mechanistic approach using population balances.* Powder Technology, 2005(160): p. 219-218.

18. Stroock, A.D., *et al.*, *Chaotic Mixer for Microchannels.* Science, 2002. **295**(25): p. 647-651.

19. Mundinger, D., *et al.*, *Demonstration of high-performance silicon microchannel heat exchangers for laser diode array cooling.* Applied Physics Letters, 1988. **53**(12): p. 1030-1032.

20. Becker, E.W., *et al.*, *Fabrication of microstructures with high aspect ratios and great structural heights by synchrotron radiation lithography, galvanoforming, and plastic moulding (LIGA process).* Microelectronic Engineering, 1986(4): p. 35-56.

21. Hruby, J., *LIGA Technologies and Applications.* MRS Bulletin, 2001: p. 337-340.

22. Rao, R.B., *et al.*, *Nozzles for Direct-Write Assembly of Three-Dimensional Periodic Structures.* Adv. Mater., 2005. **17**(3): p. 289-293.

23. Liu, Z.Y., *et al.*, *Micro-powder injection molding.* J. Mat. Pro. Tec., 2002(127): p. 165-168.

24. Campbell, C.J., *et al.*, *Direct Printing of 3D and Curvilinear Micrometer-Sized Architectures into Solid Substrates with Sub-micrometer Resolution.* Adv. Mater., 2006(18): p. 2004-2008.

25. Provin, C., *et al.*, *Three-dimensional ceramic microcomponents made using microstereolithography.* Adv. Mater., 2003. **15**(12): p. 994-997.

26. Conrad II, P.G., *et al.*, *Functional Molecularly Imprinted Polymer Microstructures Fabricated Using Microstereolithography.* Adv. Mater., 2003. **15**(18): p. 1541-1544.

27. Benavides, G.L., *et al., High aspect ratio meso-scale parts enabled by wire micro-EDM.* Microsystem Technologies, 2002. **8**(6): p. 395-401.

28. Dendukuri, D., *et al., Controlled Synthesis of Nonspherical Microparticles Using Microfluidics.* Langmuir, 2005(21): p. 2113-2116.

29. Xu, S., *et al., Generation of Monodisperse Particles by Using Microfluidics: Control over Size, Shape, and Composition.* Angew. Chem. Int. Ed., 2005(44): p. 724-728.

30. Seo, M., *et al., Continuous Microfluidic Reactors for Polymer Particles.* Langmuir, 2005. **21**(25): p. 11614-11622.

31. Roh, K.-H., D.C. Martin, and J. Lahan, *Biphasic Janus particles with nanoscale anisotropy.* Nature Materials, 2006. **4**: p. 759-763.

32. De Geest, B., *et al.*, Langmuir, 2005. **21**(23): p. 10275-10279.

33. Jeong, W.J., *et al., Continuous Fabrication of Biocatlyst Immobilized Microparticles Using Photopolymerization and Immiscible Liquids in Microfluidic Systems.* Langmuir, 2005(21): p. 3738-3741.

34. Shepherd, R.F., *et al., Microfluidic Assembly of Homogenous and Janus Colloid-Filled Hydrogel Granules.* Langmuir, 2006. **22**: p. 8618-8622.

35. Dendukuri, D., *et al., Stop-flow lithography in a microfluidic device.* Lab On A Chip, 2007. **7**(7): p. 818-828.

36. Love, J.C., *et al., Microscope projection photolithography for rapid prototyping of masters with micronscale features for use in soft lithography.* Langmuir, 2001. **17**(19): p. 6005-6012.

37. Zhao, X.-M., Y. Xia, and G.M. Whitesides, J. Mater. Chem., 1997(7): p. 1069-1074.

38. Dendukuri, D., *et al., Modeling of Oxygen-Inhibited Free Radical Photopolymerization in a PDMS Microfluidic Device.* Macromolecules, 2008. **41**: p. 8547-8556.

39. Dendukuri, D., T.A. Hatton, and P.S. Doyle, *Synthesis and Self-Assembly of Amphiphilic Polymeric Microparticles.* Langmuir, 2007. **23**(8): p. 4669-4674.

40. Pregibon, D.C., M. Toner, and P.S. Doyle, *Multifunctional Encoded Particles for High-Throughput Biomolecule Analysis.* Science, 2007. **315**(5817): p. 1393-1396.

41. Jang, J.H., *et al., A route to three-dimensional structures in a microfluidic device: Stop-flow interference lithography.* Angew. Chem. Int. Ed., 2007. **46**(47): p. 9027-9031.

42. Smay, J.E., *et al.*, *Directed Colloidal Assembly of 3D Periodic Structures.* Advanced Materials, 2002. **14**(18): p. 1279-1283.

43. Prahl, S., *Mie Scattering Calculator*. 2007, Oregon Medical Laser Center.

44. Crocker, J.C. and D.G. Grier, *Methods of digital video microscopy for colloidal studies.* Journal of Colloid and Interface Science, 1996. **179**(1): p. 298-310.

45. Bao, Z., *et al.*, *Chemical reduction of three-dimensional silica micro-assemblies into microporous silicon replicas.* Nature, 2007. **446**(8): p. 172-175.

46. Dendukuri, D., *et al.*, *Stop-flow lithography in a microfluidic device.* Lab on a Chip, 2007. **7**: p. 818-828.

47. Gervais, T., *et al.*, *Flow-induced deformation of shallow microfluidic channels.* Lab On A Chip, 2006. **6**(4): p. 500-507.

48. Mie, G., *Contributions to the optics of turbid media, particularly of colloidal metal solutions.* Annalen der Physik, 1908. **25**(3): p. 377-445.

49. Donev, A., *et al.*, *Improving the Density of Jammed Disordered Packings Using Ellipsoids.* Science, 2004. **303**(13): p. 990-993.

50. Nie, Z., *et al.*, *Janus and Ternary Particles Generated by Microfluidic Synthesis: Design, Synthesis, and Self-Assembly.* J. Am. Chem. Soc., 2006. **128**: p. 9408-9412.

51. Glotzer, S.C. and M.J. Solomon, *Anisotropy of building blocks and their assembly into complex structures.* Nature Materials, 2007. **6**(8): p. 557-562.

52. Glotzer, S.C., *Some assembly required.* Science, 2004. **306**(5695): p. 419-420.

53. Balagurov, L.A., *et al.*, *Influence of water and alcohols on photoluminescence of porous silicon.* Journal of Applied Physics, 1996. **79**(9): p. 7143-7147.

54. Gelloz, B., A. Kojima, and N. Koshida, *Highly efficient and stable luminescence of nanocrystalline porous silicon treated by high-pressure water vapor annealing.* Applied Physics Letters, 2005. **87**(031107): p. 1-3.

55. Tas, N., *et al.*, *Stiction in surface micromachining.* Journal of Micromechanics and Microengineering, 1996. **6**(4): p. 385-397.

3.6 Tables

Table 3.1 Comparison between estimated centerline velocities using Eq.(3) and experimentally obtained centerline velocities for the colloidal suspensions.

φ_{silica}	Maximum Centerline Velocity (μm/s)	Characteristic Shear Rate (s^{-1}) (2V/H)	Viscosity (Pa•s)	Estimated Centerline Velocity (μm/s)
0.35	5245	191	0.08	5675
0.40	3822	139	0.10	4540
0.45	2649	96	0.20	2270
0.50	1000	36	0.75	605

3.7 Figures

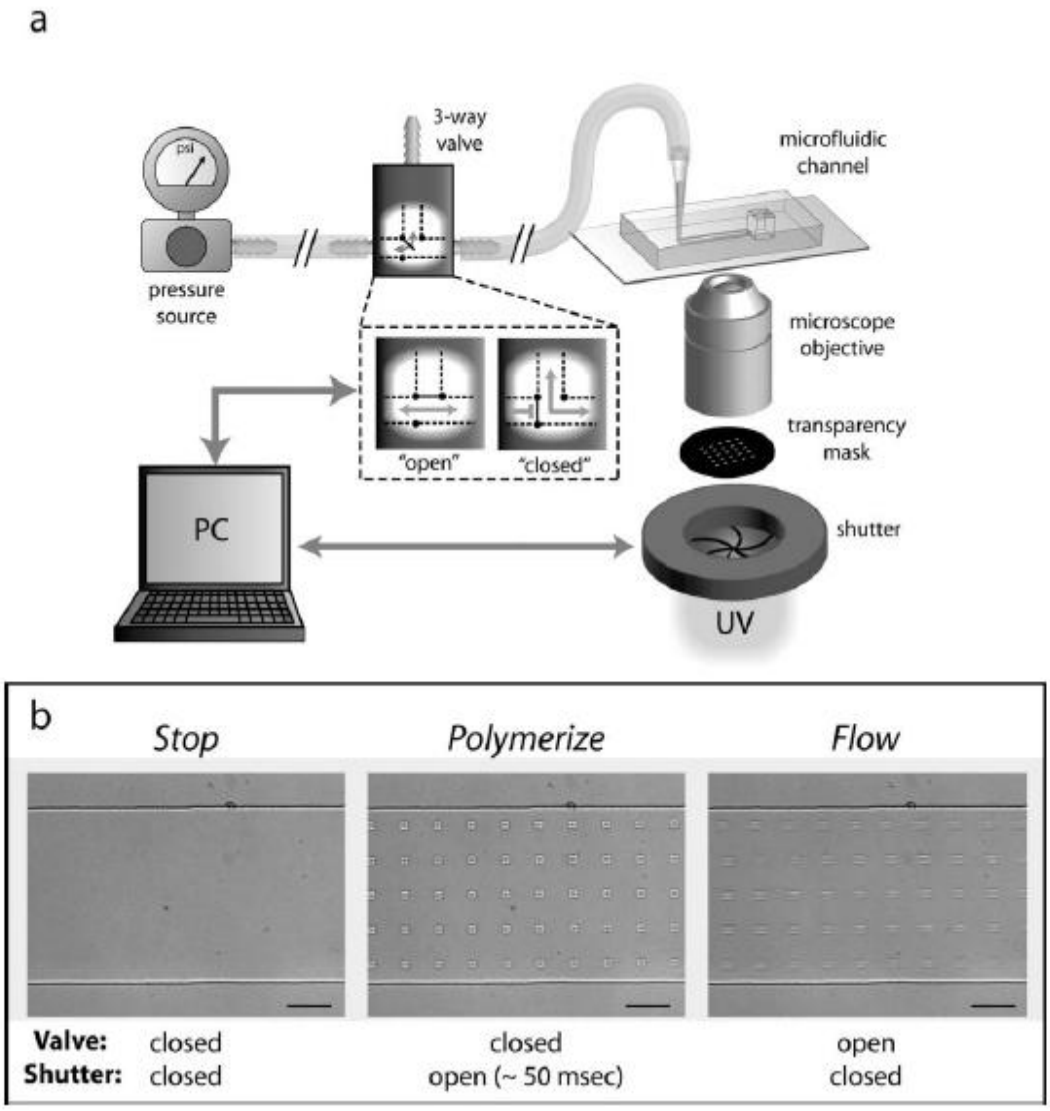

Figure 3.1 (a) SFL schematic of operation where a pressure source is applied in an on and off fashion controlled by a 3-way computer controlled valve. This pressure moves fluid in a microchannel where the fluid is then exposed to UV-light shaped by a photomask that is shuttered in sync with the valve control. The result is a start and stop flow of fluid in the microchannel, where the fluid is photopatterned when it is at rest. (b) An array of polymeric microparticles synthesized during the (left to right) stop, polymerize, flow sequence. [From Ref. [35]]

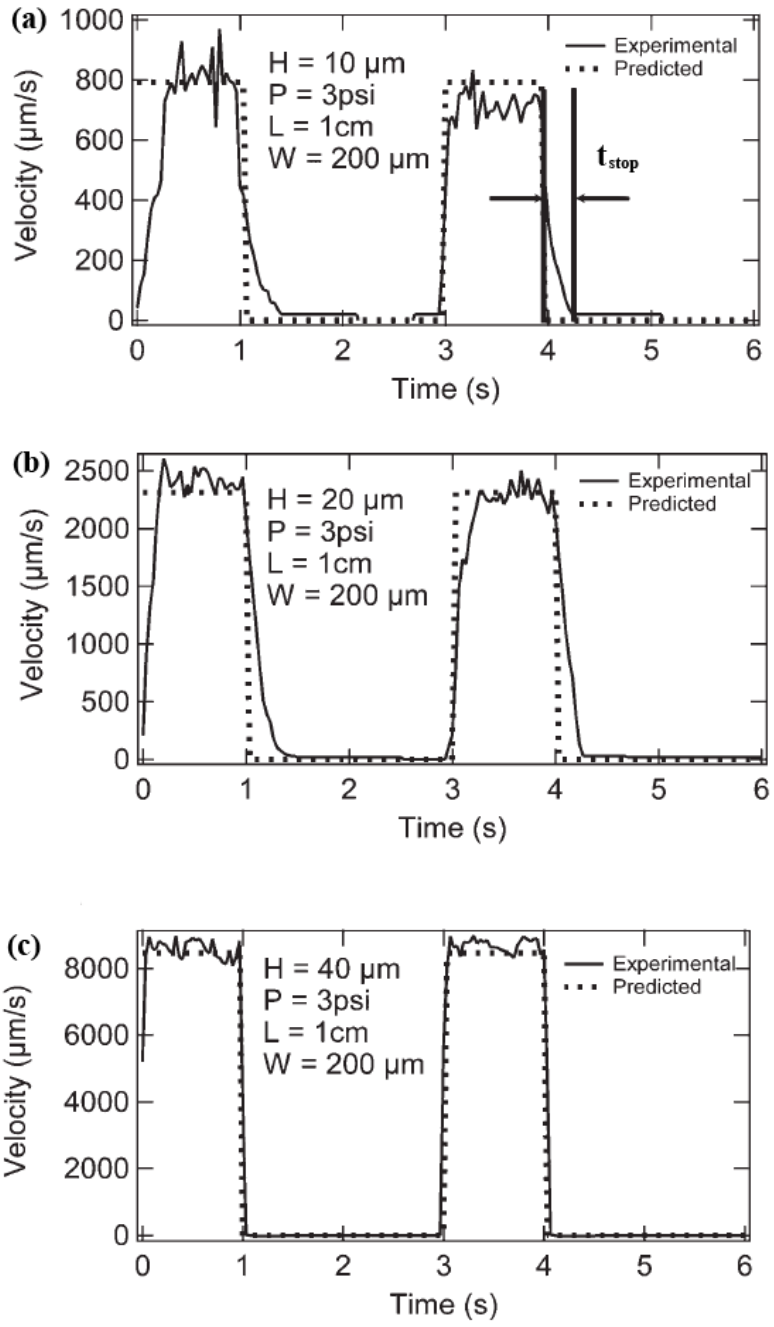

Figure 3.2 Velocity profiles of fluid flow during 2 stop-start SFL sequences and the decreasing t_{stop} times for the fluid flow to cease for different channel thicknesses of (a) 10μm, (b) 20μm, and (c) 40μm. The 40μm channel height shows no detectable time for the flow to stop once pressure is stopped. [From Ref. [35]]

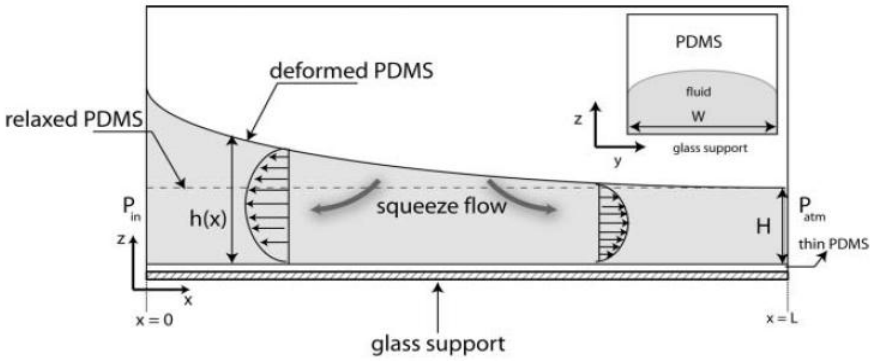

Figure 3.3 When pressure is applied during the SFL sequence, the soft PDMS microchannel is deformed. The deformation increases the thickness of the microchannel close to the point of applied pressure, with limited deformation at distances far from the point of applied pressure. When pressure is removed, during the stop sequence, the microchannel relaxes and creates a squeeze flow in the direction away from the point of applied pressure. [From Ref. [35]]

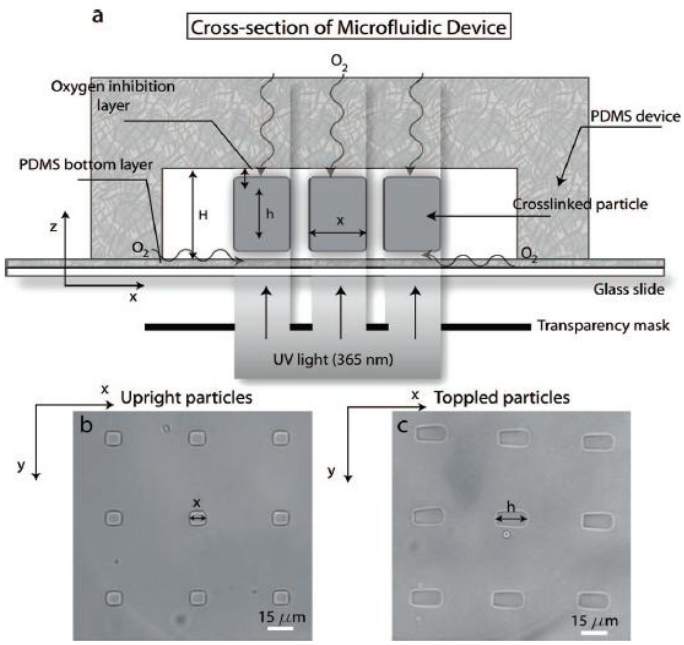

Figure 3.4 (a) The oxygen permeable PDMS microchannel allows free diffusion of oxygen to the interface of the photopolymerizeable fluid. During photopatterning, the oxygen inhibition layer stops polymerization at this interface and prevents sticking of microparticles to surface of the microchannel. (b) Upright particles immediately after synthesis and (c) the same particles after they have toppled over due to their thickness being less than that of the microchannel within which they are contained. [From Ref. [38]]

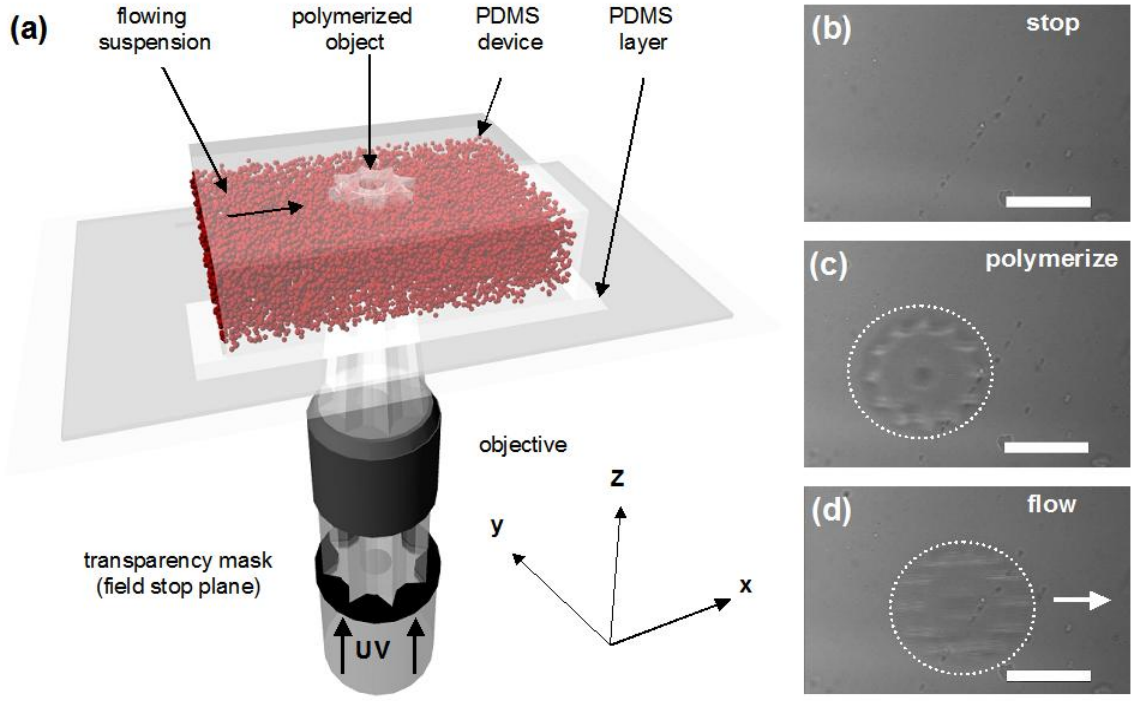

Figure 3.5 (a) Schematic illustration of stop flow lithography (SFL) system, where a photocurable, index-matched silica-acrylamide suspension is flowed through a PDMS microchannel. Microcomponents are patterned by (b) bringing the suspension to a complete stop within the microchannel, then (c) illuminating a defined volume of the suspension with UV light to induce photopolymerization, followed by (d) ejection of the as-patterned component through re-initiation of suspension flow. This process is repeated until the desired number of microcomponents is formed, at rates exceeding 10^3 min^{-1}. [Scalebars (b-d) are 100 μm]

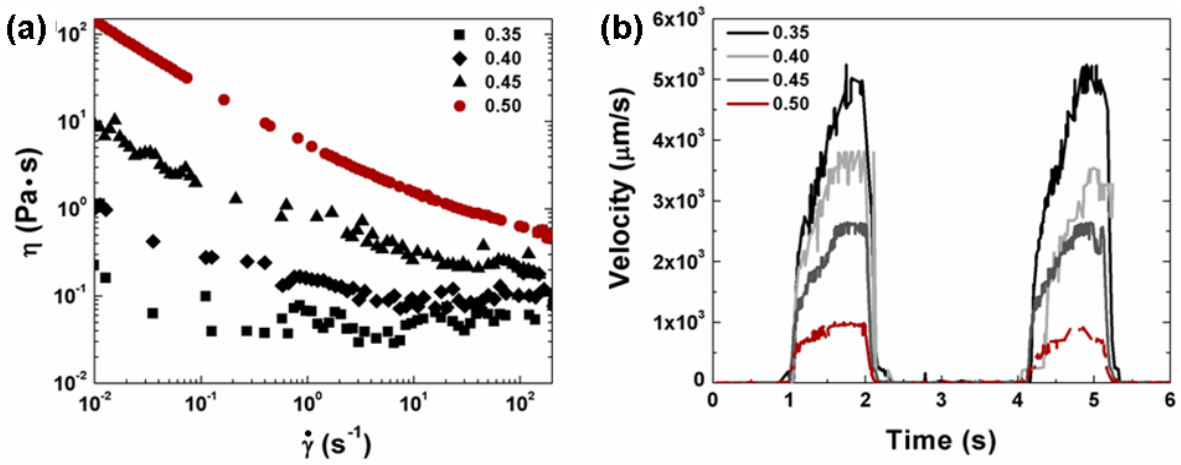

Figure 3.6 (a) Apparent viscosity as a function of shear rate for index-matched, silica-acrylamide suspensions of varying colloid volume fraction. (b) Centerline velocities for increasing solids loadings of colloidal silica within a 40 μm microchannel.

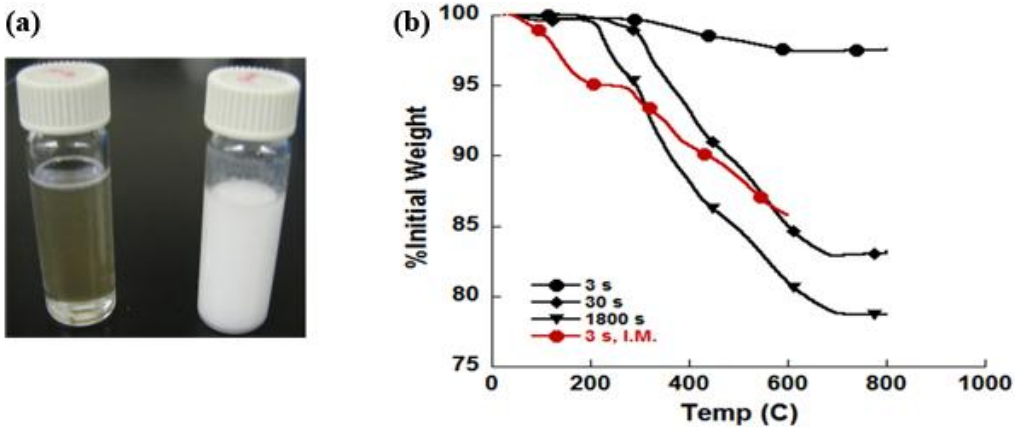

Figure 3.7 (a) Optical image of colloidal silica suspended in a mixture of DMSO and water (left) and pure water (right). (b) TGA plot of colloid-filled hydrogel granules formed at varying exposure times, where the initial monomer concentration was ~20wt%. The data indicates that [red] 3 s exposure time for the index-matched system resulted in a higher degree of polymerization (or greater weight loss) relative to the pure aqueous system.

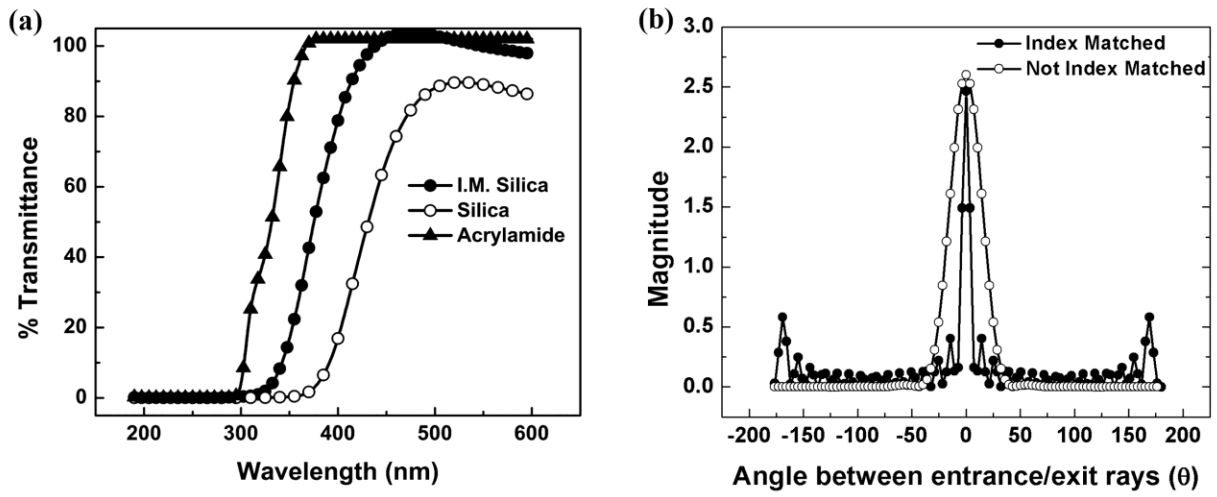

Figure 3.8 (a) UV/Vis data represented as %transmittance for a 5v/o index-matched colloidal silica suspension (filled circles), an aqueous silica suspension (open circles), and a pure 5/vo acrylamide solution (triangles). (b) Mie scattering predicted for 500nm silica particles suspended in either an index matched (filled circles) and pure aqueous media (open circles).

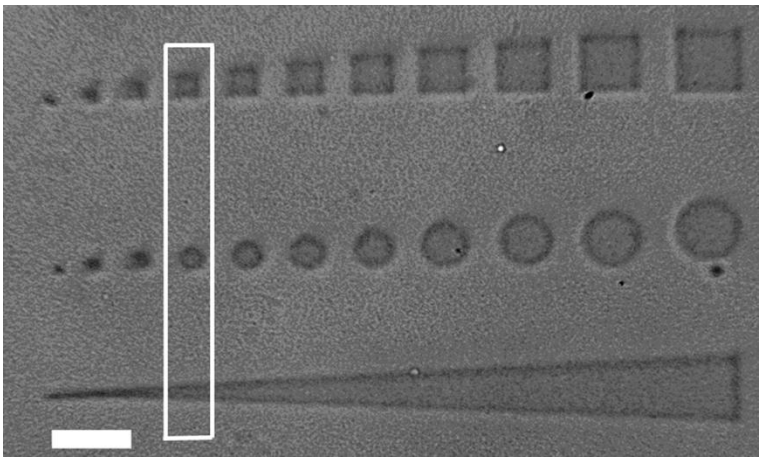

Figure 3.9 Minimum feature size determination for index-matched silica suspension used in production of colloidal microcomponents. The white box represents the minimum feature sizes (~8 μm) that can be replicated with satisfactory fidelity. [Scalebar is 30μm]

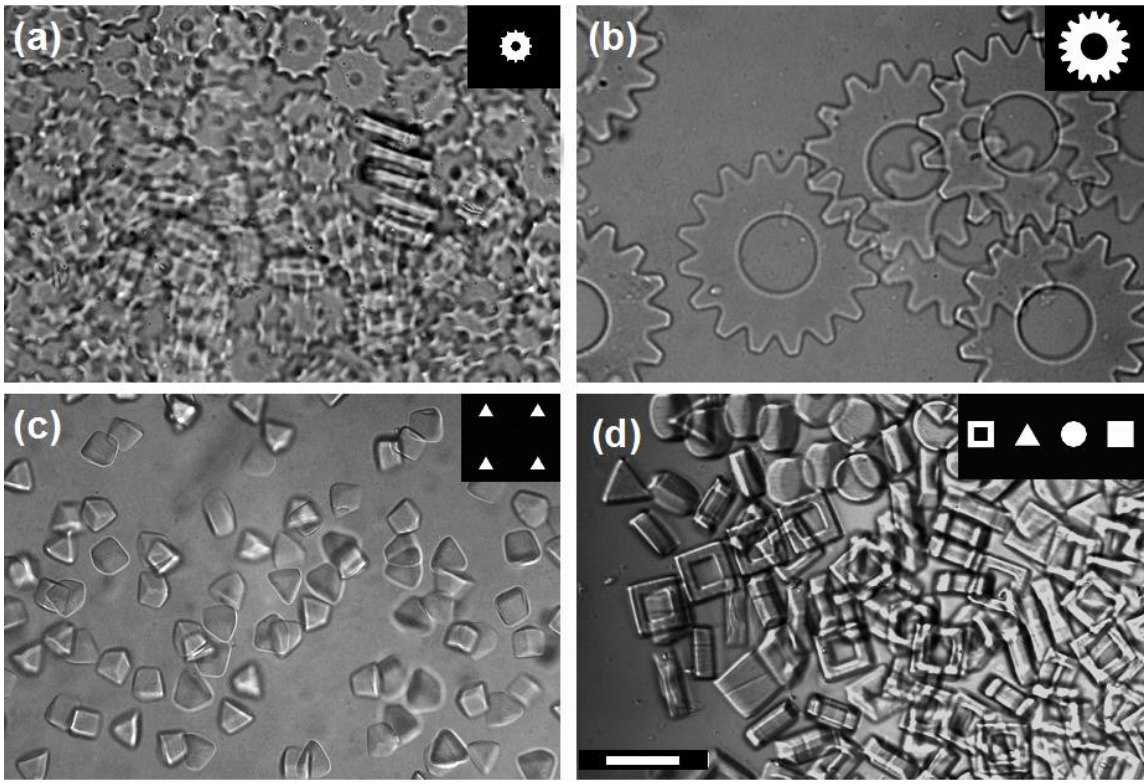

Figure 3.10 Optical images of colloidal microcomponents formed via SFL using the corresponding mask shown in each inset: (a) small microgears formed in a 30 μm thick microchannel, (b) large microgears formed in a 55 μm thick microchannel, (c) equilateral triangles formed in a 60 μm thick microchannel, and (d) an array of disk, cube, triangular, and rectangular microcomponents formed in a 40 μm thick microchannel. [Scalebar is 100 μm.]

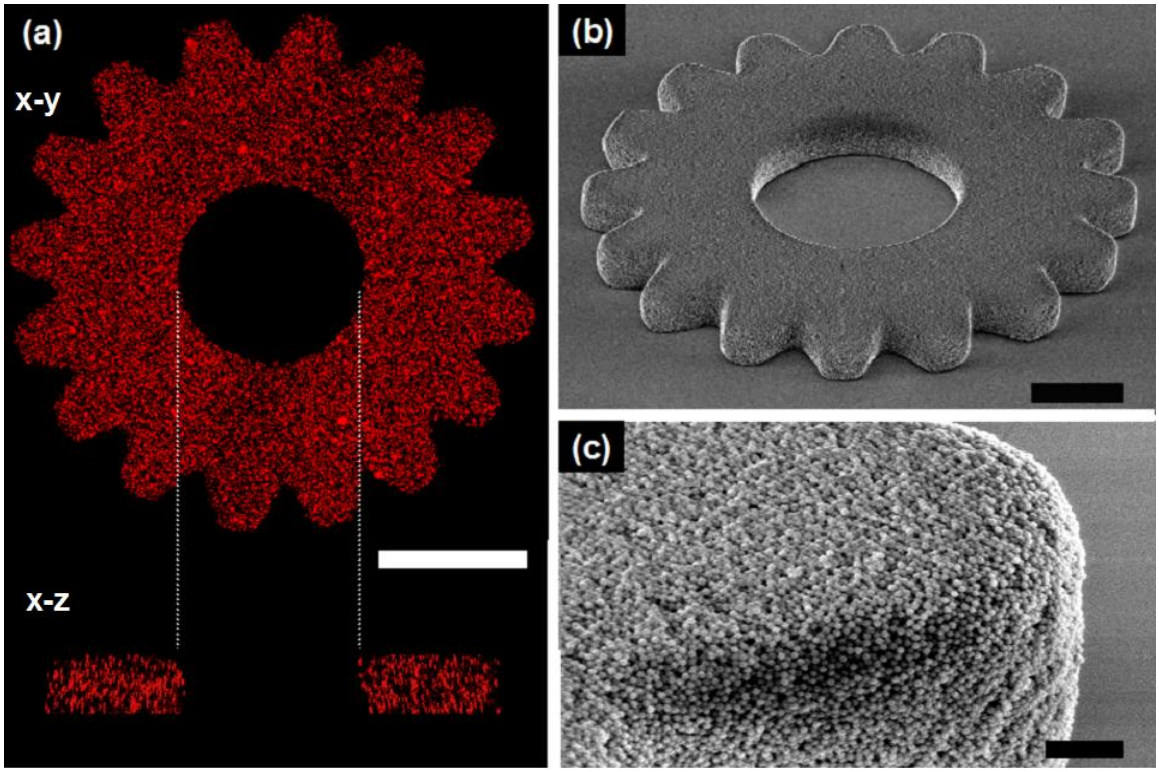

Figure 3.11 (a) Confocal image (top, *x-y* plane and bottom, *x-z* plane) of patterned colloidal microgear (*x-y* scan acquired at z = 20 μm) in an index-matched solution. (b) SEM image of a dried colloidal microgear composed of (c) densely packed silica microparticles. [Scalebars for (a)-(c) are 100 μm, 50 μm and 5 μm, respectively.]

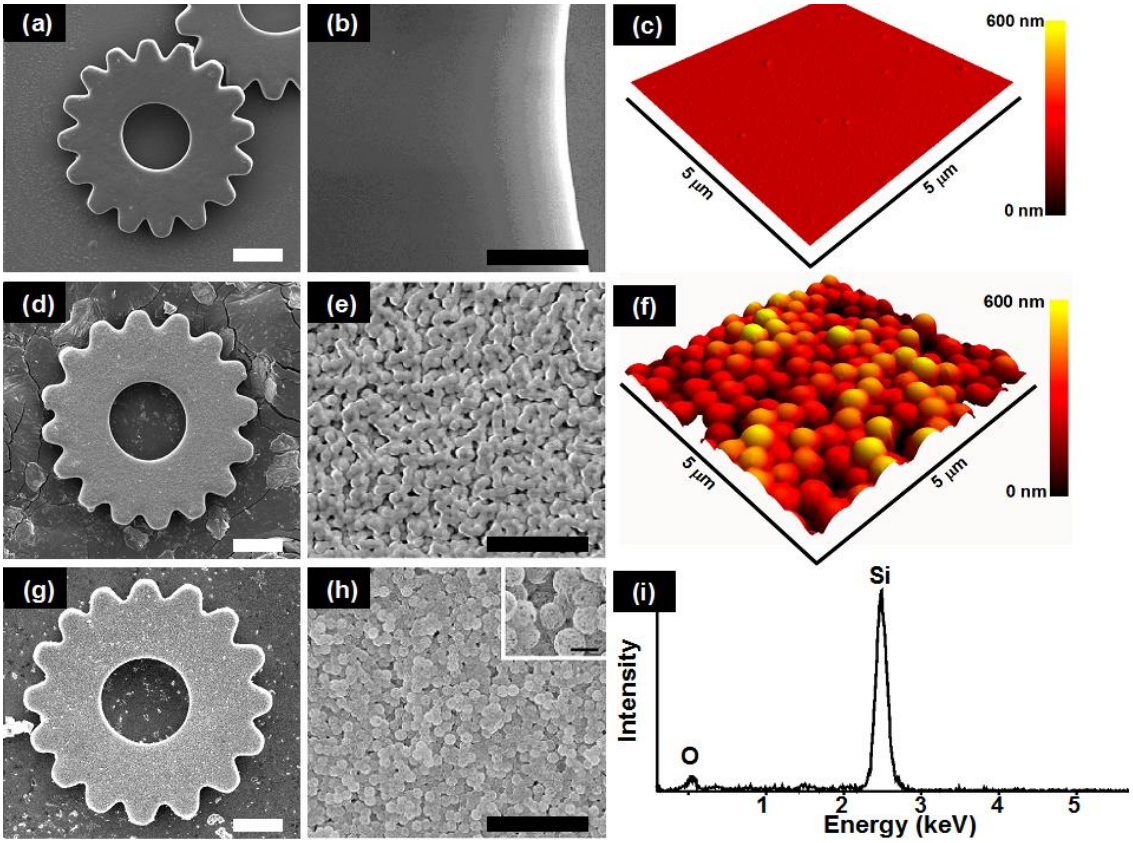

Figure 3.12 (a) SEM micrographs of a glassy silica microgear fully densified at 1150°C for 10 h, which is composed of (b) a smooth surface and dense interior (not shown), as demonstrated by (c) AFM surface reconstruction, (d) SEM micrographs of a porous silica microgear partially densified at 1150°C for 1 h, which is composed of (e) a porous network of fused silica microspheres, with (f) AFM surface reconstruction demonstrating roughness on the order of colloid size, and (g) SEM micrographs of a silicon microgear converted by a magnsiothermic reduction of the porous silica microgear shown in (d). This conversion reaction yields the nanoporous silicon replica shown at higher magnification in (h) with (i) EDX revealing a large silicon peak. [Scalebars are 50 µm for (a,d,g), 5µm for (b,e,h), and 500 nm for the inset in (h).]

CHAPTER 4

PACKING DYNAMICS OF NON-SPHERICAL COLLOIDAL GRANULES

4.1 Introduction

Granular matter is ubiquitous; sand on the beach, cosmetic and food powders, agricultural commodities, and pharmaceutical tablets are just a few examples. While most granular matter is non-spherical, the vast majority of studies on granular phenomena have focused on spherical granules.[1-6] Recently, the non-equilibrium packing behavior of granular matter has been studied by computer simulations and shown to depend significantly on granule shape.[1, 7-9] However, to date, most experimental investigations of granular materials has been limited to spherical, polydisperse, or randomly shaped granules.

The ability to precisely engineer the size, polydispersity, shape and deformability of colloidal granules is required to further elucidate basic physical concepts of granular materials. For example, it has been recently reported that flow behavior of granular matter is altered when the granule diameter is less than 100 microns,[8, 10], when surface forces become important relative to gravity.[8] For example, μN cohesive forces were shown to induce phenomenological similar drop breakup dynamics in ca. 100μm, spherical granular media; however, these cohesive forces could be mitigated by changing granule shape or surface roughness (**Figure 4.1)**.[10] Since granular packings are non-ergodic in nature and highly sensitive to loading conditions,[11-13] the details of granule flow into a container or mold are critical to efficient packing. Since cohesive surface forces are greatly affected by contact area and tangential forces, the granule shape and surface roughness are critical system parameters.[10]The static packing behavior of non-spherical granules is not well understood due to the limited availability of model granules and the relative difficulty of simulating large asymmetric particle assemblies under static and

dynamic conditions. Much of the existing experimental studies have been focused on the use of photoelastic plastic beads to study stress propagation[14-15] and most simulations involve spheroids containing a large degree of convexity.[16-18] Still, some experiments[8, 19] and simulations[1, 9] have been carried out on non-convex granule packs, which have led to observations that differ from that of spherical granular media. For example, an initial packing fraction of $\phi \approx 65$v/o for cubes in containers with lateral areas of either 100 or 20 times less than that of the individual cubes is reported by Fraige *et al*. and Latham *et al*., respectively (**Figure 4.2a**).[1, 8] When Fraige *et al*. increased the container lateral area to 1,600 times higher than of the individual cubes, the packing fraction decreased to $\phi \approx 0.37$ (**Figure 4.2)**, demonstrating the significance of wall effects on cube packing.

X-ray micro-computed tomography (μCT) has recently emerged as a method for directly visualizing the packing behavior of granular media.[2, 4, 20-21] This technique allows one to visualize packing in three dimensions at the single granule level.[2, 4, 20-21] By applying image analysis techniques, such as Voronoi tesselation, one can quantify the packing uniformity within the resultant granule beds.[2, 20-24] Voronoi tesselation maps out the volume closest to each granule, where the variance in the resultant Voronoi volumes provides a measure of packing homogeneity. To date, μCT and corresponding image analysis methods have only been applied to spherical granular sytems.

To quantify the distribution of Voronoi volumes (vv), it is necessary to segment and label each granule. **Figure 4.3a** shows a granular bed composed of 150,000 spherical granules along with the probability distribution of their local packing fraction (**Figure 4.3b)**, which is obtained by dividing the granule volume by its local Voronoi volume.[21] Aste *et al.* has recently shown

that monodisperse, spherical granule Voronoi volume distributions can be well approximated by a modified Gamma distribution, called a k-Gamma distribution,[25]

$$f(V,k) = \frac{k^k (V - V_{\min})^{(k-1)}}{\Gamma(k)(\bar{V} - V_{\min})^k} \exp(-k \frac{V - V_{\min}}{\bar{V} - V_{\min})}$$

where V is the Voronoi volume, $V_{\min}$ is the minimum observed Voronoi volume, $\bar{V}$ is the average Voronoi volume and $k = (\bar{V} - V_{\min})^2/(\sigma^2)$ is defined by the variance in Voronoi distribution. **Figure 4.4a** shows real data (points) and the *k*-Gamma fit (line). In their work, the Voronoi volume distribution of a large number of spherical granules is probed from a random loose-packed, $\phi \approx 0.55$, to a random close-packed, $\phi \approx 0.64$, (or jammed) state via X-ray μCT. Using the k-Gamma analytical function, Aste *et al.* reports a collapse of all jammed granule conditions onto a single curve via scaling by $(V - V_{min})/(\bar{V} - V_{min})$ for very similar *k*-values, k~12 (**Figure 4.4b**). Aste *et al*. suggests that similar *k*-values indicate a similar local granule configuration that may be scaled to different Voronoi distributions.[25]

Unlike their spherical counterparts, non-convex, prismatic granules have an increased probability of planar contact, thus one can no longer rely on convexity to easily segment each granule. In this case, proper segmentation requires high magnification μCT scans, which typically is achieved by reducing the sampling volume. Moreover, if the granules are geometrically asymmetric, local Voronoi volumes can no longer be found simply by growing from the granule center of mass. The use of a two-step distance transformation method is necessary to determine the local Voronoi volumes from μCT for non-spherical, asymmetric granules, **Figure 4.5**.[20]

In this chapter, we create large quantities of non-spherical colloidal granules of controlled surface roughness via stop-flow lithography (describe in Chapter 3). The packing behavior of cube, triangle, and rectangle prism granules as well as a bimodal cube granule system is investigated by μCT and image analysis under both static and dynamic conditions. Though we are capable of performing analysis in the dry state, all granules are analyzed in the wet (lubricated) state to limit effects to shape and surface roughness. We then fit their Voronoi volume distribution to the k-Gamma distribution in an attempt to quantify a particular order parameter for the jamming condition of low dispersity cube, rectangular prism and bimodal cube granules.

4.2 Experimental Methods

4.2.1 Material System

Colloidal suspensions are prepared by first adding an appropriate amount of polyethyleneimine (PEI); (1800 g mol^{-1}); Aldrich Chemical Co to deionized water. The solution pH is then adjusted to 6 by adding aliquots of a 1M HNO_3 solution (Fisher Scientific). Following this, silica microspheres (ϕ^v_{silica} = 0.5, 500 ± 25 nm diameter, FUSO, Japan) are added to the solution and allowed to stir overnight to allow the desired adsorption of (0.5 mg) PEI m^{-2} silica[26]. This opaque suspension is then index-matched by the addition of dimethyl sulfoxide (DMSO; Fisher Scientific) to achieve a volumetric ratio of 65:35 v/v DMSO to water. The suspension is then concentrated by centrifuging at 3000 rpm. After the supernatant is decanted, a photoinitiator, ϕ^v_{init} = 0.03 (Darocur 1173, Ciba), acrylamide monomer, a ϕ^w_{acryl} = 0.09 (Acros Organics), and crosslinking agent N,N methylene bisacrylamide (Aldrich Chemical Co.) at an 8:2 w/w ratio of monomer to crosslinking agent is added to the dense sediment. The index-

matching is achieved by adding an appropriate amount of deionized water to yield a final composition of $\phi^{v}_{silica} = 0.50$, 62:38 v/v of DMSO:water, and $\phi^{w}_{acrylamide} = 0.08$.

4.2.2 Microfluidic Device Fabrication

Microfluidic devices are produced via soft lithography[27] by pouring PDMS (Sylgard 184; Dow Corning) onto a silicon wafer patterned with SU-8 photoresist features (SU-8 50; Microchem). After curing the PDMS, the mold is cut out and treated via UVO[27] with an accompanying PDMS coated coverslip. After treatment, the mold and coverslip is brought into conformal contact and allowed to bond, forming a monolithic structure. The microchannel dimensions used in these experiments are 1 mm in diameter with channel heights of either 30 μm, 40 μm or 55 μm, by spin-coating at either 3000, 2500, or 2000 rpm, though channel heights as low as 10 μm have been successfully used in this system. Photomasks are rendered with CAD (Autocad 2005 ®) and printed via a high-resolution laser printer (5080 dpi; CAD/Art Services, Inc.).

4.2.3 Patterned Granule Fabrication and Harvesting

The transparent colloidal suspension is flowed into the SFL microfluidic device in a pulsed sequence and synched with flashes of UV exposure as described in ref [28]. For this material system, by applying a voltage to a solenoid valve through software written in Labview©, the suspension is flowed at 2 psi for 400 ms, the pressure is then stopped by removal of the applied voltage. After the pressure is released, the system is allowed to relax for 300 ms, where the motion of the fluid comes to a full stop. Immediately after the flow is stopped, UV light is projected through a photomask into an objective lens (20X, N.A. 0.46; Zeiss) that focuses the negative mask image onto the microchannel for a periods of 400 ms. This process is repeated until the desired number of microcomponents are formed. Optical microscopy is used to quantify

the average size and variance of the granule population by sampling 100 granules and measuring using Fiji ©.

After granule formation, the granules remain immersed in the excess unpolymerized index matched suspension. The granules are purified by first washing away the excess unpolymerized aqueous silica suspension via solvent exchange with an aqueous solution of 65:35 v/v DMSO to water. This step is repeated 3 times to assure all colloidal silica not associated with the granule media has been removed. Following this, the aqueous solution is exchanged with acetone as an intermediate for heptane. This step is repeated 3 times. After the granules are immersed in acetone, the acetone is substituted for heptane via a similar 3 step solvent exchange process. If the granules are to be examined in the dry state, they can remain in heptane to allow evaporation; however, in all studies reported here, the granules are immersed in hexadecane to lubricate the granule surface. The granules immersed in hexadecane are then gently pulled into a 200 μL plastic pipette tip (TH-PL-9400260; Thermo-Fisher Scientific) and then brought into contact with the meniscus of the polyimide tube μCT sample chamber. The granules are then allowed to gently fall to the bottom of the container, to a bed height greater than 7mm.

4.2.4 Direct Imaging via X-ray Micro-Computed Tomography

Polyimide tubing, diameter ca. 2mm (SWPT-064-030; Smallparts, inc.) is mounted on a ca. 10mm^2 plastic cutout from a petri-dish (Fisher Scientific) using a small amount of 5 min epoxy (S-206; Devcon). If the granules are to be interrogated in the dry state, the chamber is then filled with heptane (H2198; Aldrich). If the granules are to be interrogated in the lubricated condition, the chamber is filled with hexadecane (H6703; Aldrich).

The samples are centered on the stage of the X-ray μCT (MicroCT-200; X-Radia). After the edge of the sample is found, the stage is moved so the collection volume is in position more

than 300μm from the container walls and 1 mm and 0.5 mm from the bottom of the container and top of the granule pack, respectively. A 41 kV and 7 Watts X-ray source is used and either a 20X or 10X objective lens is selected resulting in a pixel size of 0.931 or 1.63 μm/pixel respectively. The samples are rotated 180^{o} and images are taken every ¼ degree at a resolution of 1024x1024x1024 voxels at 8bits/channel.

The segmentation accuracy is increased when higher magnification objective lenses are used during analysis; however, this also reduces the number of granules sampled. Thus, we used a 10X, 1.63 μm/pixel, objective lens to probe the cubic and rectangular prism granules. This allows us to sample more than 1,000 granules, while still performing accurate segmentation based on shape regularity. For the bimodal cube system, we used a 20X, 0.93 μm/pixel, objective lens as an optimum magnification to achieve accurate segmentation while acquiring a statistically significant, greater than 500, number of granules, since shape regularity is not a reliable method.

4.2.5 Image Analysis

The volume fraction of each granular pack is determined by first importing the raw data into Fiji © and then thresholding away pixel values below 150, resulting in granule sizes that compare well to those images by SEM (see Figure 4.7). The thresholded image volumes are then analyzed by counting bright pixels and dark pixels. The sum of the bright pixels (granules) is divided by the sum of the dark pixels (void) to get the average volume fraction of the granule bed. The thresholded volume is then imported into Imaris © image analysis software. A seeded watershed algorithm is used to segment the granules based on the average size of the granule. The output image volume is then imported into Matlab © and downsampled by 10X to accommodate the computation capacity of the computer.

The Voronoi tesselation map for each granule is then found using a custom Matlab © script, which first takes a distance transform of all granules in the presence of all other granules and then a distance transform of each individual granule, referred to as the global and local distance maps, respectively. The difference between these maps is the Voronoi map of each granule. The interface between all Voronoi maps is then determined and labeled to form the Skeleton of Influence Zone (SKIZ). This script is based off the work done by Alshibli *et al.*[20].

Since the granule segmentation is not perfect, unrealistic granule sizes that are either less than or greater than ±35% the average granule volume are removed. These values lie outside of the C.V. and represent over or under segmented granules. This type of filter is not applied to the bimodal granule distribution data, since those volumes are acquired at 20X magnification and the segmentation is more accurate. Finally, since the sampled volume resides within the interior of each granule pack, it contains fragments at the edge of the sampled region of interest. A filtering algorithm is performed to remove these external Voronoi volumes. Finally a smoothing algorithm, Kernel Density Estimate (KDE), is used to plot a histogram of the Voronoi volumes with a bin number of 36. Finally, the *k*-value from the k-Gamma function is determined using a least-squares non-linear curve fit of the binned KDE experimental data.

4.3 Results and Discussion

Non-spherical colloidal granules with controlled surface roughness are created by stop-flow lithography (SFL), following the method outlined in Chapter 3 (**Figure 4.6**). Large quantities (> 5000) of granular matter are produced by this approach with a C.V. < 10%, of monodisperse square and equilateral triangle geometries with side length or diameter of 50μm and depth of 40μm are produced 20 at a time using photomasks with 5x4 arrays in microchannels of depth 50μm. While rectangular prism granules of 150x50x40μm^3 (3:1:1) are

produced 8 at a time using a 4x2 array in a 50μm microfluidic channel depth. Interestingly, the lateral dimensions of the patterned granules can be controlled by the location of the focal plane within the microchannel, enabling facile control of granule size dispersion. By exploiting this, a bimodal distribution of $50x50x40\mu m^3$ and $75x75x40\mu m^3$ granules are also produced, with a corresponding C.V. of 300%. SEM micrographs of all granule geometries are shown in **Figure 4.7**.

Prior to transferring the patterned colloidal granules into the μCT sample chamber, they are cleaned via a three-step washing and solvent exchange process. The granules are then immersed in hexadecane to evaluate their assembly in a lubricated environment.[29] The granules are transferred into the μCT sample holder by creating a meniscus at the top of the chamber, allowing the granules to gently fall into the container, shown schematically in **Figure 4.8a**. A reconstruction of the raw μCT data obtained on this sample is provided in **Figure 4.8b**.

After the granules have been allowed to fill the container to a depth of >7mm, the sample is gently placed into the x-ray μCT chamber. A volumetric region of interest is then imaged using either a 20X and 10X objective lens, corresponding to $680x10^6\mu m^3$ and $906x10^6\mu m^3$ respectively. As a benchmark, a typical single granule volume ranges from $100x10^3\mu m^3$ (cubes) to $300\mu m^3$ (rectangles). After the samples are digitized via image collection on the CCD, the initial packing fraction of the granules is determined for all shapes, as shown in **Figure 4.9**. Lubricated cubes exhibit an initial packing fraction of $\phi < 0.50$, even though their ultimate packing fraction can theoretically reach unity. This is in agreement with results by Fraige *et al.*, who reports packing fractions as low as $\phi = 0.34$ for random packings of cubes in the absence of wall effects.[1] Four initial packings of nearly monodisperse cube granules are investigated and the resulting packing fractions lie within a narrow average volume fraction of $\phi = 0.47 \pm 0.15$

(**Figure 4.9)**. Interestingly, triangular granules display a similar packing fraction as that observed for cubes; which suggests that the contact area between adjacent granules is the dominant parameter as opposed to a specific granule shape. The maximum contact area of $2.5x10^3\ \mu m^2$ for the cubes and triangles is identical; whereas the rectangular granules have a maximum contact area of $7.5x10^2 \mu m^2$ with a lower corresponding packing fraction, $\phi \approx 0.38$. The bimodal cube population has an average contact area of $4.0x10^2\ \mu m^2$ with a maximum contact area of $5.6x10^3 \mu m^2$ for the large granules and maximum contact area of $2.5x10^3 \mu m^2$ for the smaller population. The bimodal cubic granules exhibit the lowest initial packing fraction of $\phi \approx 0.33$ though this may be due to a combined effect of contact area and size dispersion.

Select granule geometries are agitated via horizontal shaking for varying times. A horizontal shaking method is employed due to readily available equipment and the unique ability of rotationally asymmetric geometries to compact by rearranging their orientation without moving beyond their center of mass.[7] The packing dynamics of both the bimodal cube and rectangular prism geometries are investigated as a function of agitation times, because of their initially low packing fraction, while the cubic system serves as a benchmark.

The monodisperse cubes begin at an initially higher packing fraction than the other geometries and thus take quite some time to undergo any significant change in packing fraction; however, after several hours of agitation, their packing fraction approaches a plateau of $\phi \approx 0.56$ in this experiment. The bimodal granules undergo rapid consolidation in a very short time (~600s). The rectangular granules also undergo rapid consolidation from $\phi \approx 0.38$ to $\phi \approx 0.52$; however, the most dramatic change in ϕ occurs under the first agitation event, indicating the granules initially pack in a highly unstable configuration.

Though the total packing fraction yields useful information on mean population behavior, μCT data also contains information on individual granule shape and orientation. By mapping the distance from each granule surface to that of its neighbors, we create a Voronoi tesselation map that provides the Voronoi volume of each granule; where the free volume for consolidation is the difference between the Voronoi volume and the granule volume.[20] Statistical analysis of the resulting Voronoi volume distributions provides information about the packing homogeneity of the granule bed and, through fitting of the *k*-Gamma function, the resulting *k*-values can be used to track the evolution of local granule structure.[25] Specifically, the *k*-value is the ratio of the average free volume of the granules to the variance of the Voronoi volumes. If the *k*-values remain constant through compaction, it is a strong indicator that the local packing structure also remains constant.

To determine the Voronoi volumes, we follow an image segmentation and Voronoi tesselation method generic to all granule shapes. First, we erode the surface of the granules to reduce the degree of planar contact. A full assembly of narrow size dispersion cube granules used in this analysis is presented in **Figure 4.10a**; due to the erosion necessary to label and track the granules, the volumes used in analysis (blue) are reduced in size yet maintain the same shape and orientation as the original granule (white overlay). We then use a seeded watershed algorithm to properly label each granule. Finally, we employ the Voronoi tessellation method outlined by Alshibli *et al*. [20] A distance transformation is applied to the entire granule pack and then compared to the distance transform for each individual granule from the surface of the granule. The difference of these distance transformations is the local volume for each particular granule. The benefit of this technique is that the distance transform is measured from the surface

of the granules; therefore, there is no implicit assumption about the shape or orientation of the particular granule.

The Voronoi volume distributions for cube and rectangular prism granule geometries as well as the bimodal cube granule distribution as well as examples of the skeleton of influence zone outlining the Voronoi volumes around these granules are provided in **Figure 4.10b-d**. The monodisperse cube granules initially display a broad Voronoi volume distribution, which decreases from an average volume of 1,060μm^3 to 940μm^3 after 25,000s of agitation time (**Figure 4.11a**). The rectangular granules also undergo a change in Voronoi volume distribution under agitation (**Figure 4.11b)**. **Table 4.1** shows that there is a decrease in mean Voronoi volume from 1,520μm^3 to ~1380μm^3, accompanied by a reduction in standard deviation from 308μm^3 to 245μm^3. Finally, we determine the Voronoi volume distribution of the bimodal granule system for all agitation times. **Figure 4.11c** shows the initial packing conditions have larger average Voronoi volumes with a broad distribution; however, there is a dramatic shift of average volumes and a narrowing of the distribution under agitation.

The Voronoi volume distributions for each system are then fit to the k-Gamma function, yielding the resulting curves shown in **Figure 4.11**. Interestingly, the Voronoi distributions fit well to the k-Gamma distribution reported by Aste *et al*.; however, unlike their experiments on spherical granules, the *k*-values for the cube granules decrease with agitation time, **Table 4.1**. This *k*-value variation reflects the fact that the local structure changes during consolidation, i.e., the standard deviation of Voronoi volumes does not change in a manner consistent with the average Voronoi volume. The rectangular prism granule's *k*-value, however, remains largely constant over the experimental conditions probed with an average *k*-value of *k*~9.9. The bimodal granule system also displays a relatively unchanging *k* with an average value of *k*~9.3. This data

shows clearly that the cube granule's *k*-value decrease with increasing packing fraction; whereas the rectangular prism and bimodal granule distributions remain at similar values throughout compaction. Importantly, using the *k*-values obtained from these fits, we are able to collapse all the curves onto a single master curve by scaling the distributions as $(V - V_{min})/(\overline{V} - V_{min})$ (**Figures 4.11a-c,right**). The *k*-values observed at varying packing fractions are summarized in **Figure 4.12**)

4.4 Conclusions

We have demonstrated non-spherical colloidal granules of varying geometry and prescribed size dispersion and surface roughness can be patterned in large quantities using stop-flow lithography. We have also demonstrated the ability to quantify the packing homogeneity of non-spherical granules using Voronoi tesselation and fit the resultant Voronoi distributions to the *k*-Gamma analytical function. The resulting characteristic *k*-values may indicate that cubic granules are undergoing a fundamental change in their local packing structure. The rectangular prism and bimodal granule distributions yield similar *k*-values during compaction, which suggests their local granule structure is "frozen" even though the free volume decreases as a function of agitation time. The good fit of the data and the collapse of the *k*-Gamma distributions for cubic, rectanglar, and bimodal cubic granules onto single master curves suggests that this function may be broadly applied to non-spherical and polydisperse granular matter.

4.5 References

1. Fraige, F.Y., P.A. Langston, and G.Z. Chen, *Distinct element modelling of cubic particle packing and flow*. Powder Technology, 2008. **186**(3): p. 224-240.
2. Aste, T., *Variations around disordered close packing.* J. Phys.: Condens. Matter, 2005. **17**: p. S2361-S2390.

3. Deis, T.A. and J.J. Lannutti, *X-ray Computer Tomography for Evaluation of Density Gradient Formation during the Compaction of Spray-Dried Granules.* J. Am. Ceram. Soc., 1998. **81**(5): p. 1237-1247.

4. Fu, X., *et al.*, *Application of X-ray Microtomography and Image Processing to the Investigation of a Compacted Granular System.* Part. Part. Syst. Charact., 2006(23): p. 229-236.

5. Lukasiewicz, S.J., *Spray-Drying Ceramic Powders.* J. Am. Ceram. Soc., 1989. **72**(4): p. 617-624.

6. Zhou, J., *et al.*, *Measurement of Forces Inside a Three-Dimensional Pile of Frictionless Droplets.* Science, 2006. **312**: p. 1631-1633.

7. Mehta, A., *et al.*, *Competition and cooperation: aspects of dynamics in sandpiles.* J. Phys.: Condens. Matter, 2005. **17**: p. S2657 - S2687.

8. Latham, J.-P. and A. Munjiza, *The Modelling of Particle Systems with Real Shapes.* Philosophical Transactions: Mathematical, Physical and Engineering Sciences, 2004. **362**(1822): p. 1953-1972.

9. Remond, S., J.L. Gallia, and A. Mizrahi, *Simulation of the packing of granular mixtures of non-convex particles and voids characterization.* Granular Matter, 2008. **10**: p. 157-170.

10. Royer, J.R., *et al.*, *High-speed tracking of rupture and clustering in freely falling granular streams.* Nature, 2009. **459**: p. 1110-1113.

11. Jaeger, H.M. and S.R. Nagel, *Physics of the Granular State.* Science, 1992. **255**(1523-1531).

12. Kadanoff, L.P., *Built upon sand: Theoretical ideas inspired by granular flows.* Reviews of Modern Physics, 1999. **71**(1): p. 435-444.

13. Jop, P., Y. Forterre, and O. Pouliquen, *A constitutive law for dense granular flows.* Nature, 2006. **441**(7094): p. 727-730.

14. Majmudar, T.S. and R.P. Behringer, *Contact force measurements and stress-induced anisotropy in granular materials.* Nature, 2005. **435**(23): p. 1079-1082.

15. Geng, J., *et al.*, *Footprints in Sand: The Response of a Granular Material to Local Perturbations.* Physical Review Letters, 2001. **87**(3): p. 035506-1 -035506-4.

16. Donev, A., *et al.*, *Improving the Density of Jammed Disordered Packings Using Ellipsoids.* Science, 2004. **303**(13): p. 990-993.

17. Langston, P.A., *et al., Distinct element modelling of non-spherical frictionless particle flow.* Chemical Engineering Science, 2004. **59**: p. 425-435.

18. Wouterse, A., S. Luding, and A.P. Philipse, *On contact numbers in random rod packings.* Granular Matter, 2009. **11**: p. 169-177.

19. Nolan, G.T. and P.E. Kavanagh, *Random packing of nonspherical particles.* Powder Technology, 1995. **84**: p. 199-205.

20. Al-Raoush, R. and K.A. Alshibli, *Distribution of local void ratio in porous media systems from 3D X-ray microtomography images.* Physica A, 2006. **361**: p. 441-456.

21. Aste, T., M. Saadatfar, and T.J. Senden, *Geometrical structure of disordered sphere packings.* Physical Review E, 2005. **71**(061302): p. 1-15.

22. Starr, F.W., *et al., What Do We Learn From the Local Geometry of Glass-Forming Liquids?* Physical Review Letters, 2002. **89**(12): p. 125501-1 - 125501-4.

23. Slotterback, S., *et al., Correlation between Particle Motion and Voronoi-Cell-Shape Fluctuations during the Compaction of Granular Matter.* Physical Review Letters, 2008. **101**(258001): p. 1-4.

24. Slotterback, S., *et al., Correlation between Particle Motion and Voronoi-Cell-Shape Fluctuations during the Compaction of Granular Matter.* Physical Review Letters, 2008. **101**: p. 258001-1 - 258001-4.

25. Aste, T. and T. Di Matteo, *Emergence of Gamma distributions in granular materials and packing models.* Physical Review E, 2008. **77**(021309): p. 1-8.

26. Smay, J.E., *et al., Directed Colloidal Assembly of 3D Periodic Structures.* Advanced Materials, 2002. **14**(18): p. 1279-1283.

27. Zhao, X.-M., Y. Xia, and G.M. Whitesides, J. Mater. Chem., 1997(7): p. 1069-1074.

28. Dendukuri, D., *et al., Stop-flow lithography in a microfluidic device.* Lab on a Chip, 2007. **7**: p. 818-828.

29. Lee, I., *Friction and adhesion of silica fibres in liquid media.* Journal of Material Science, 1995. **30**: p. 6019-6022.

4.6 Tables

Table 4.1 Mean, standard deviation, and *k*-values of (top) cubes, (middle) rectangular, and (bottom) bimodal cube Voronoi volume distributions.

Monodisperse Cubes	Vavg	variance	k
0	650.9822	7912.1	15.5696
10	599.2038	6890.2	12.9929
100	608.4517	7148.6	13.3093
1000	613.7749	7500.7	13.1261
25000	574.3516	6490	11.602
Rectangles	**Vavg**	**variance**	**k**
0	941.6681	30941	11.3145
10	900.4448	30250	10.0373
40	848.3599	26798	9.2807
300	855.9332	28582	8.9557
900	868.3518	26191	10.2717
2700	845.4404	25419	9.6578
25000	855.1446	26435	9.6636
Bimodal Cubes	**Vavg**	**variance**	**k**
0	3617.5	665070	11.0535
10	3240.1	506870	10.6725
40	3096.7	589570	8.0807
300	2906.1	402310	9.884
600	2821.5	370850	9.8129
1200	2828.6	403610	9.0735
3000	2767.3	365590	9.3845
10000	2778.1	359460	9.6566

4.7 Figures

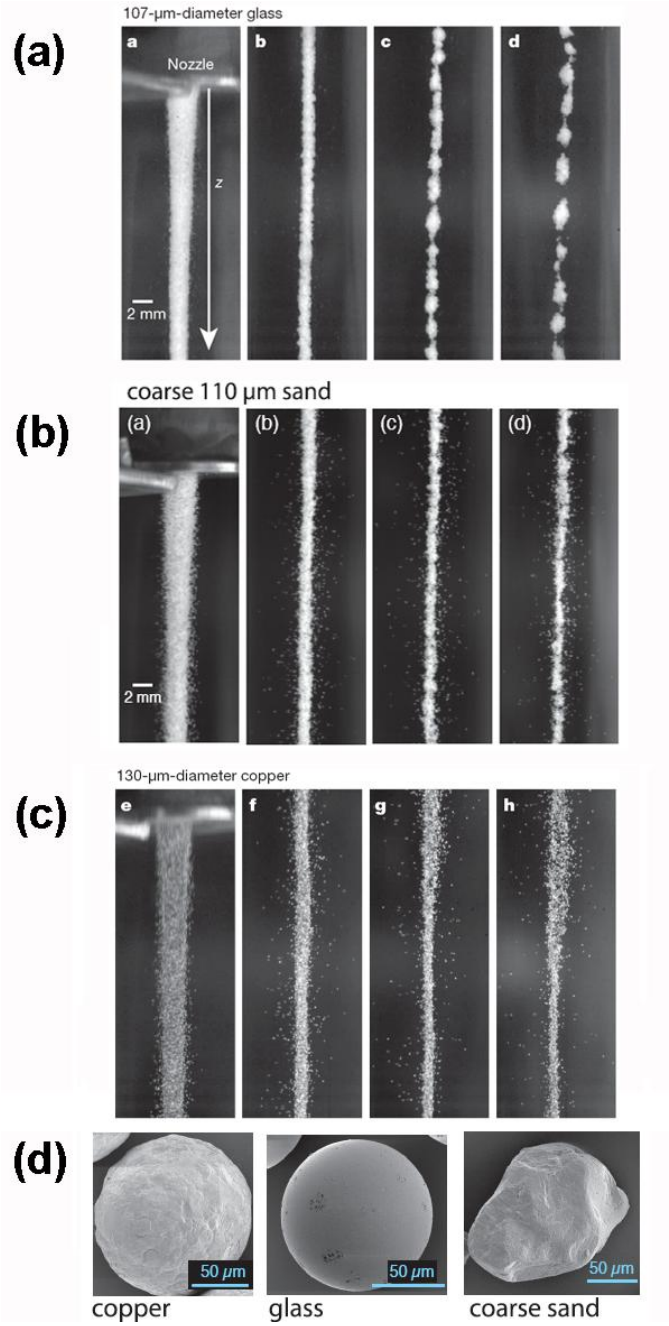

Figure 4.1 High speed video of granular flow from a hopper for (a) smooth glass, (b) coarse grained sand, and (c) copper granules shown in (d). The video is taken at (left to right) just below, 20, 50, and 77 cm distances from the hopper nozzle. Only the smooth glass granules exhibit a drop-breakup phenomenon (a). Taken from Ref. [10].

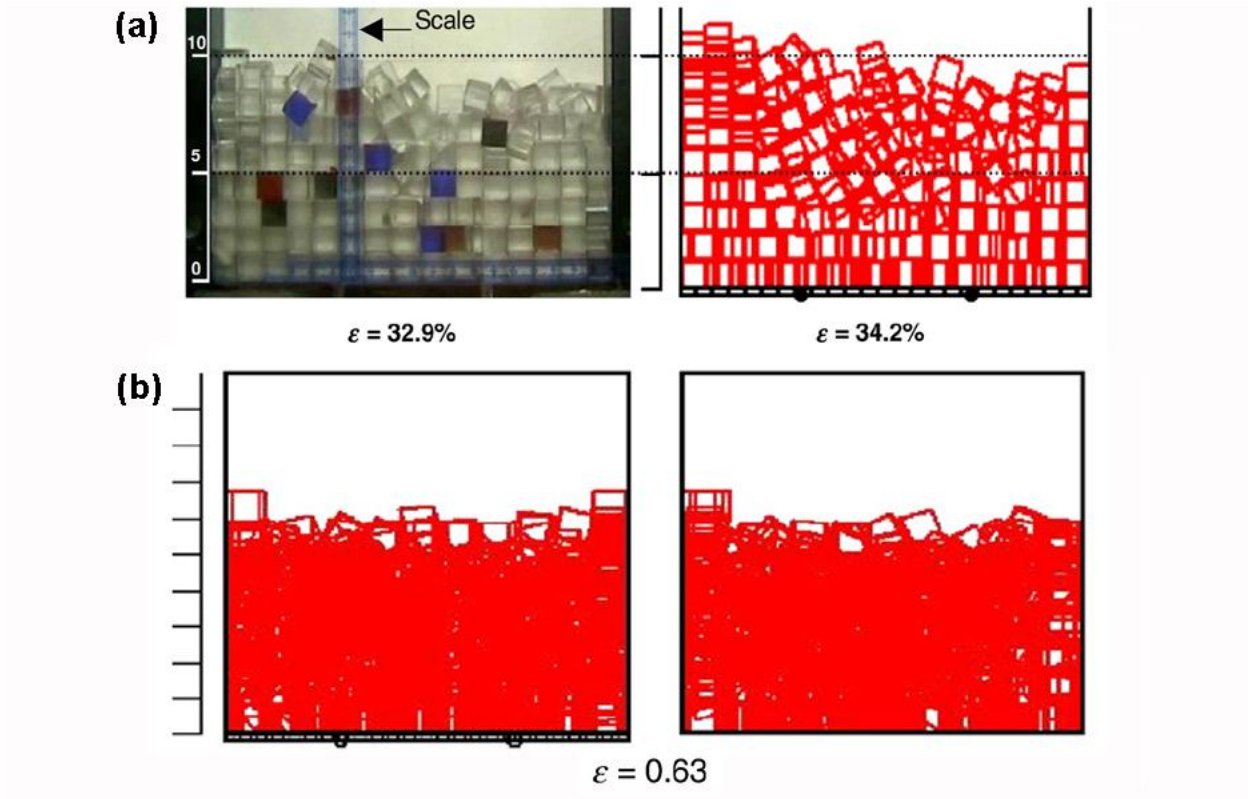

Figure 4.2 (a) Experiment (left) and simulation (right) 12.5 mm^2 of cubes packed in a 100 x 30 mm^2 container and (b) simulation of 12.5mm^2 cubes packed in a 500x500mm^2 container. (a) Presents a void fraction of $\phi \approx 0.33$ and (b) presents a void fraction of $\phi \approx 0.63$ – resulting in a packing fraction of $\phi \approx 0.66$ and $\phi \approx 0.37$, respectively. Taken from Ref. [1].

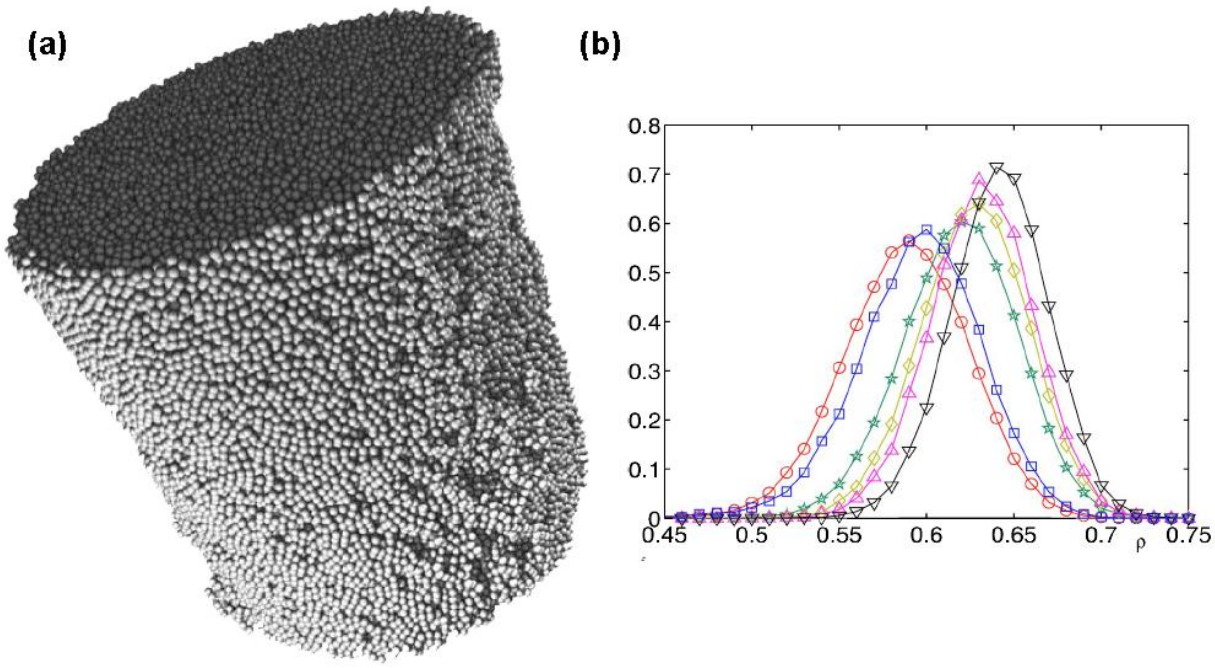

Figure 4.3 (a) 150,000 spherical ~1mm glass bead packing reconstructed from x-ray μCT data. (b) Local packing fraction of constituent glass beads. Taken from Ref. [21].

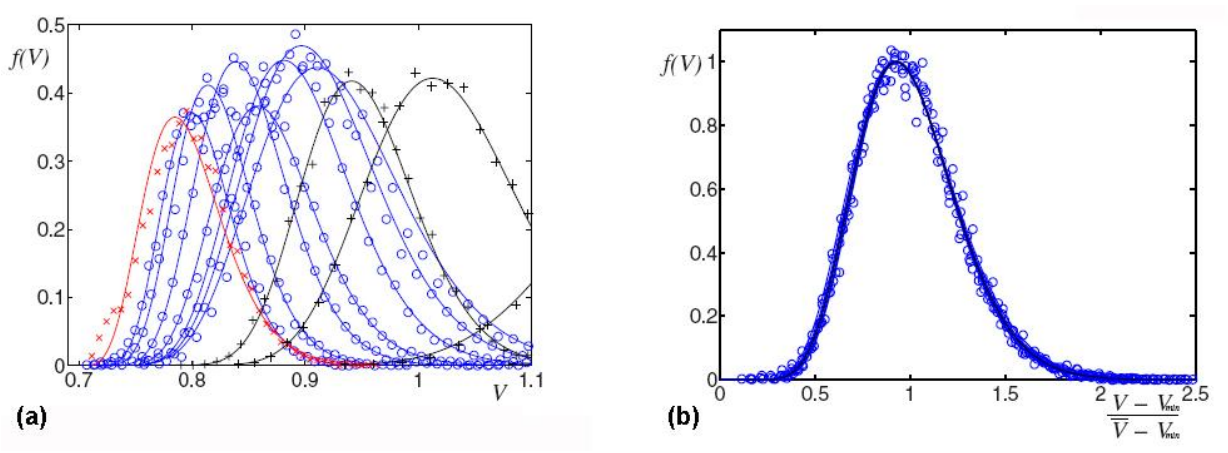

Figure 4.4 (a) The Voronoi volume distributions for (o) jammed, (+) unjammed, and (x) crystalline packings where the minimum Voronoi volume is the minimum volume of a sphere, or 0.6975. (b) The jammed granules collapse onto a single curve if scaled by $(V-V_{min})/(\bar{V}-V_{min})$. Taken from Ref. [25].

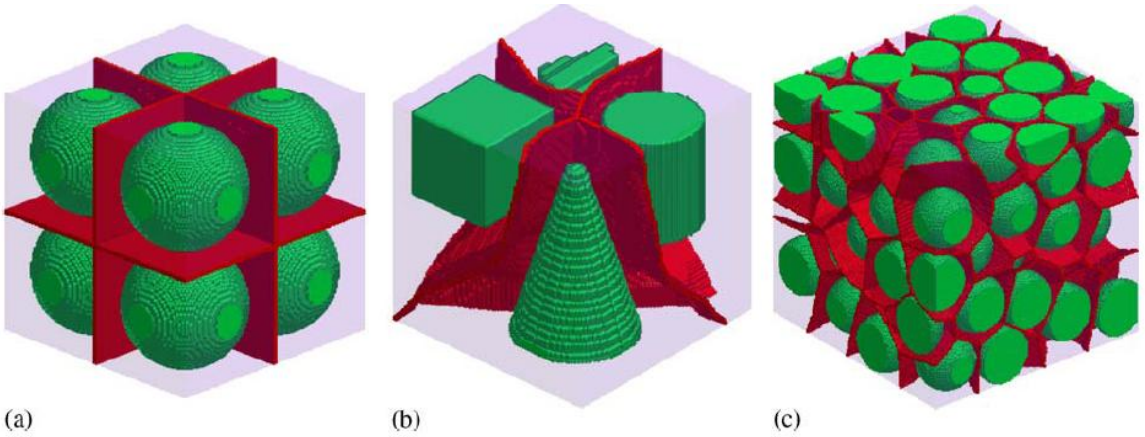

Figure 4.5 (green) (a) Simulated spheres (b) various simulated non-spherical objects and (c) a μCT collection of real spherical granules and the (red) outlines of their Voronoi volumes, otherwise referred to as Skeleton of Influence Zone. Taken from Ref. [20].

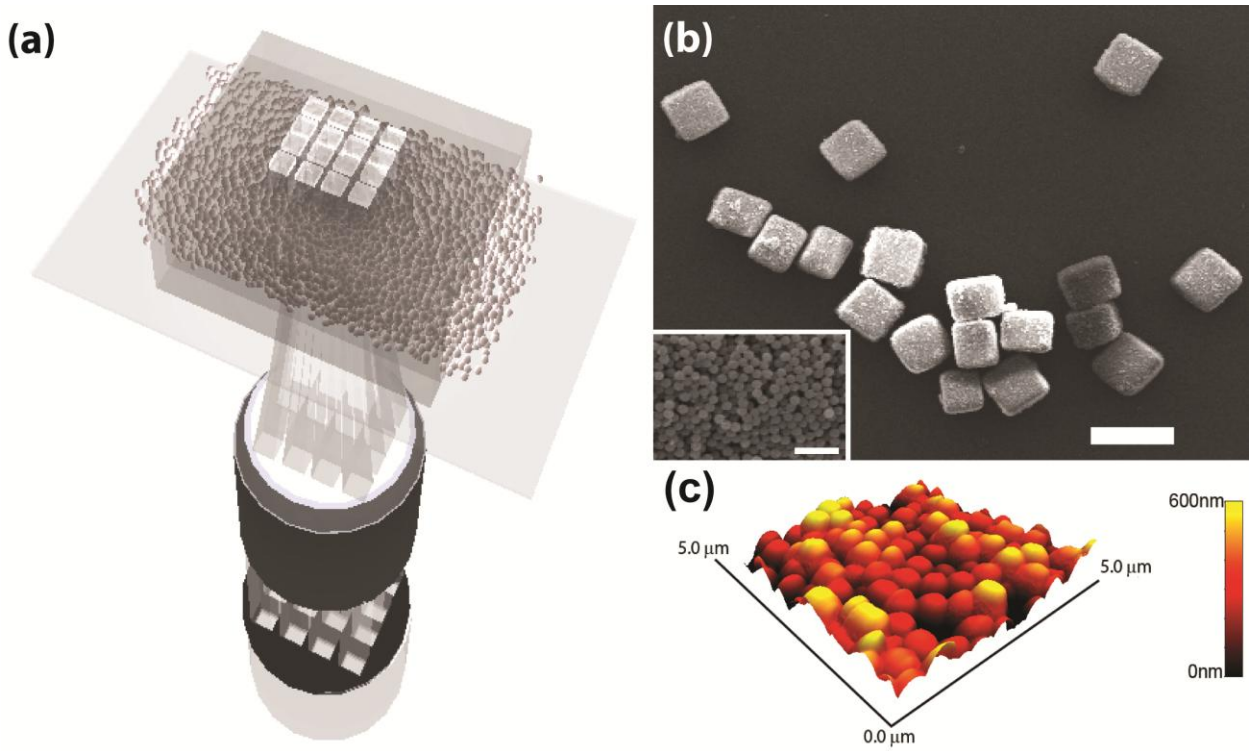

Figure 4.6 (a) Schematic illustration of SFL of colloidal silica using a square array photomask to produce cube granules. (b) SEM micrograph of cube colloidal granules with an (inset) SEM micrograph of 500nm silica colloids on surface of granule. (c) AFM micrograph of colloidal silica shown in the inset of (b). [Scalebars are (b) 75µm and (b, inset) 2µm]

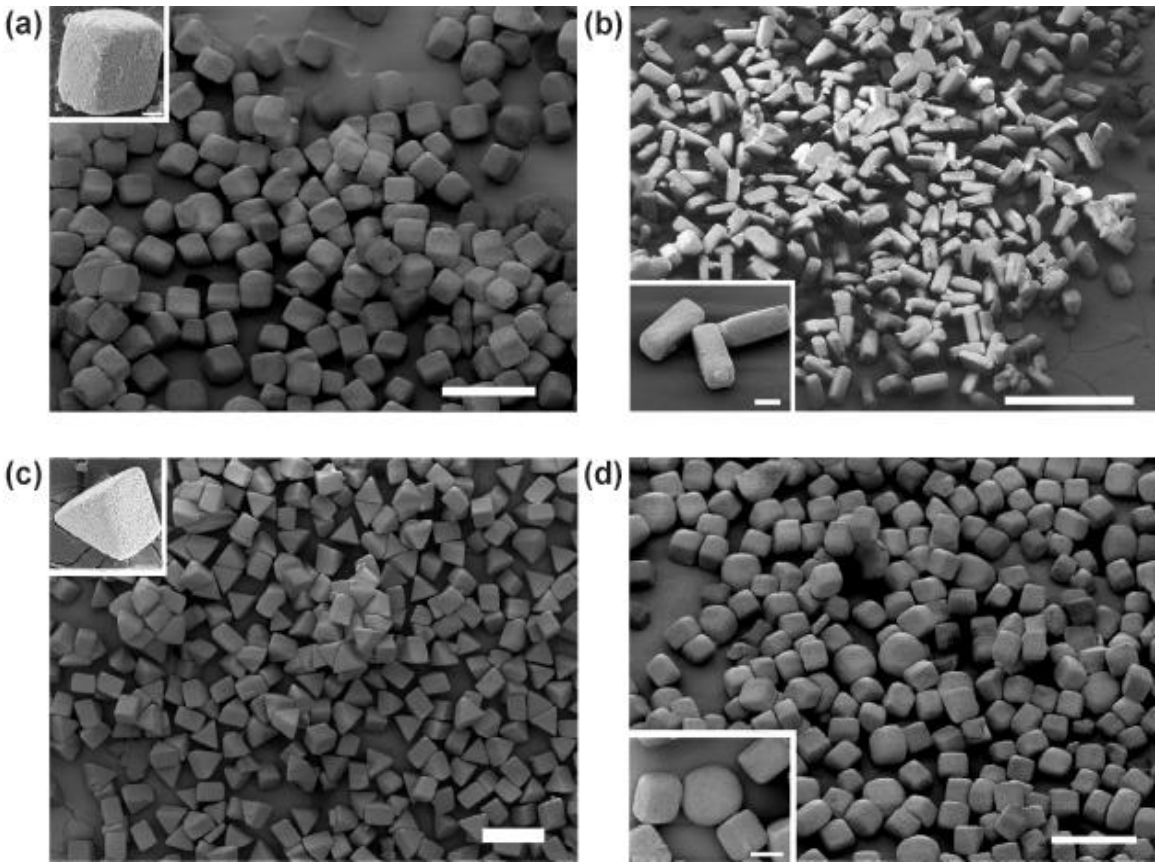

Figure 4.7 SEM micrographs of (a) cube, (b) rectangular prism, (c) triangular prism, and (d) bimodal cube granules. The insets of (a-d) are representative granules. [Scalebars are (a) 150μm, (b) 500μm, (c) 100μm, (d) 150μm and (a,c) insets are 10μm and (b,d) insets are 50μm]

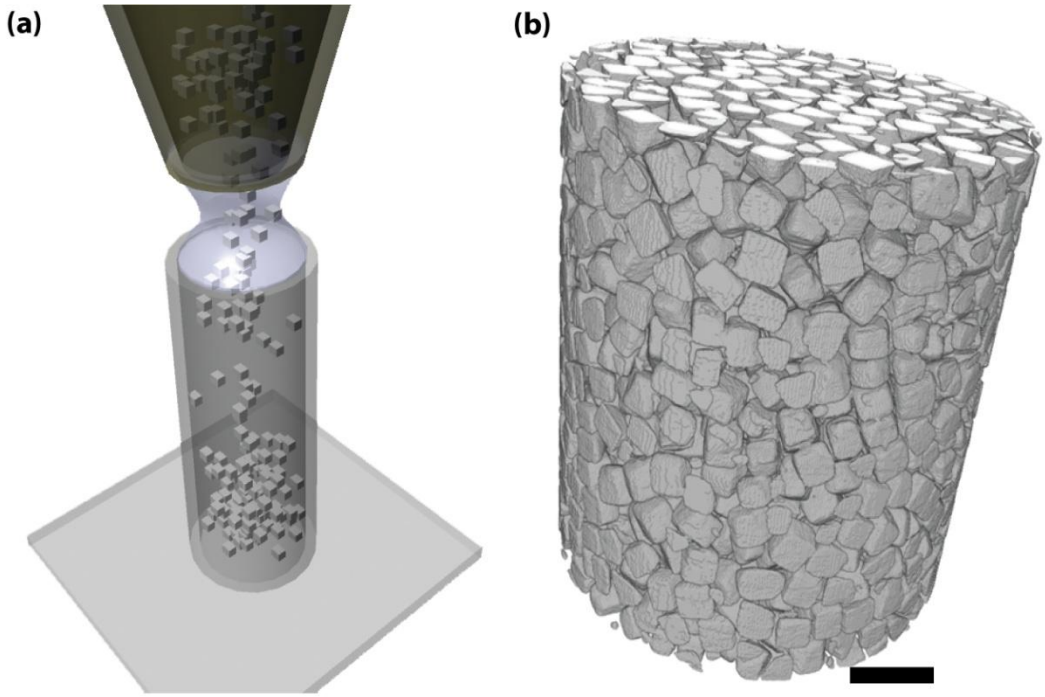

Figure 4.8 (a) Transfer of granules through alkane meniscal contact with x-ray μCT sample chamber. (b) Reconstructed image of cubic granule pack within sample chamber. [Scalebar is 100μm]

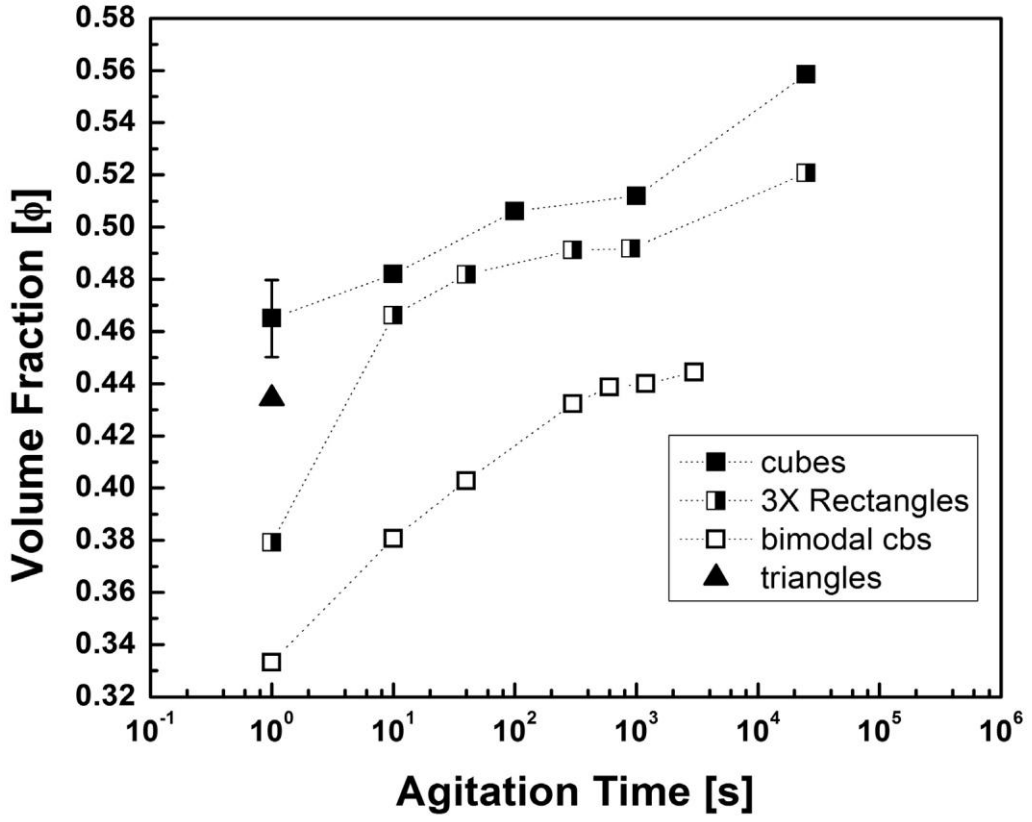

Figure 4.9 Volume fraction of cube, rectangular, bimodal cube and triangular granules at varying agitation times.

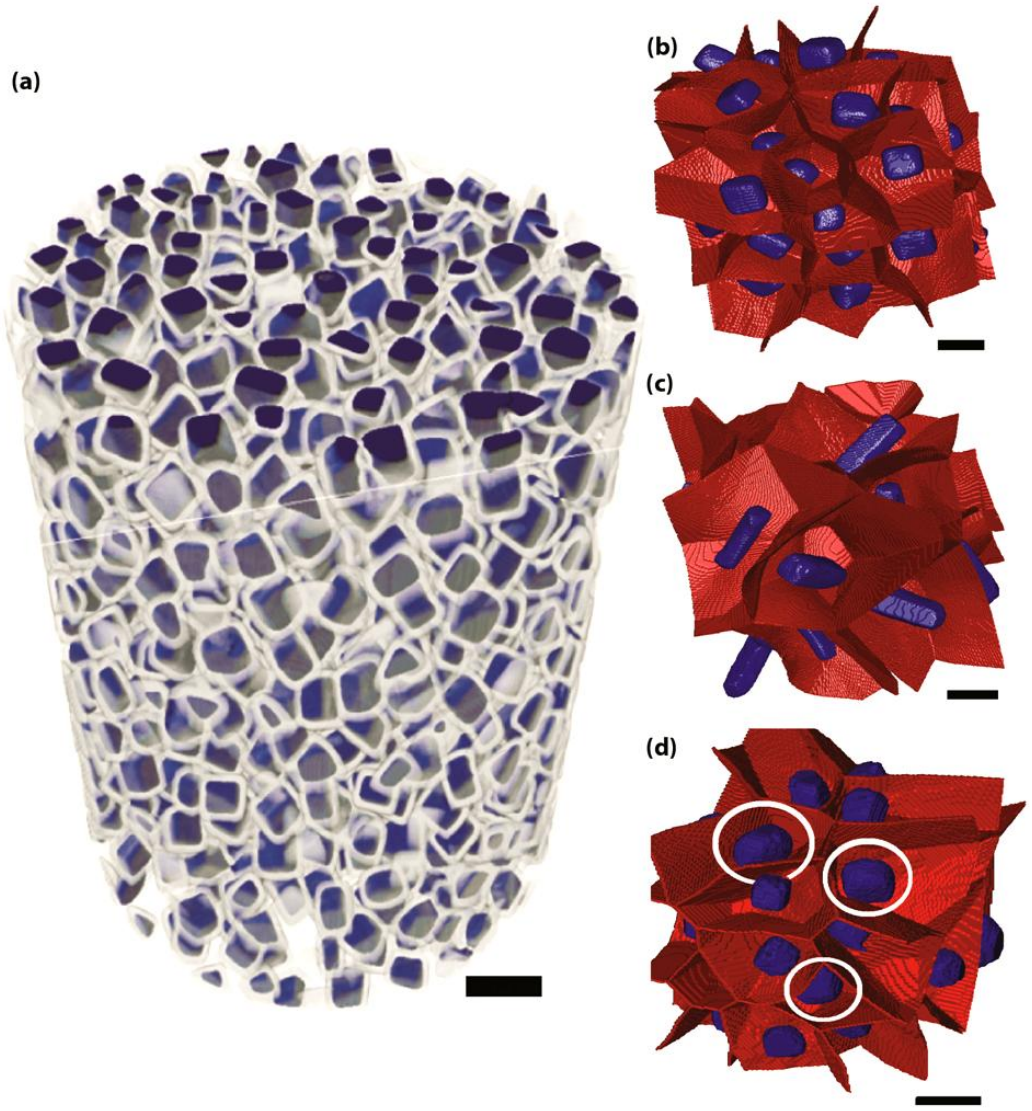

Figure 4.10 (a) Granule pack extracted from core of larger granule bed, more than 6 granule diameters from sides of container and top or bottom of bed. Eroded (blue) cube granules overlayed on raw (gray) cube granule bed. The erosion allows for image segmentation and Voronoi volume visualization for (b) cubes, (b) rectangular granules, and (c) a bimodal distribution of cube granules, where some of the larger granule population is circled in white. [Scalebars are 100μm, 50μm, 50μm and 70μm respectively]

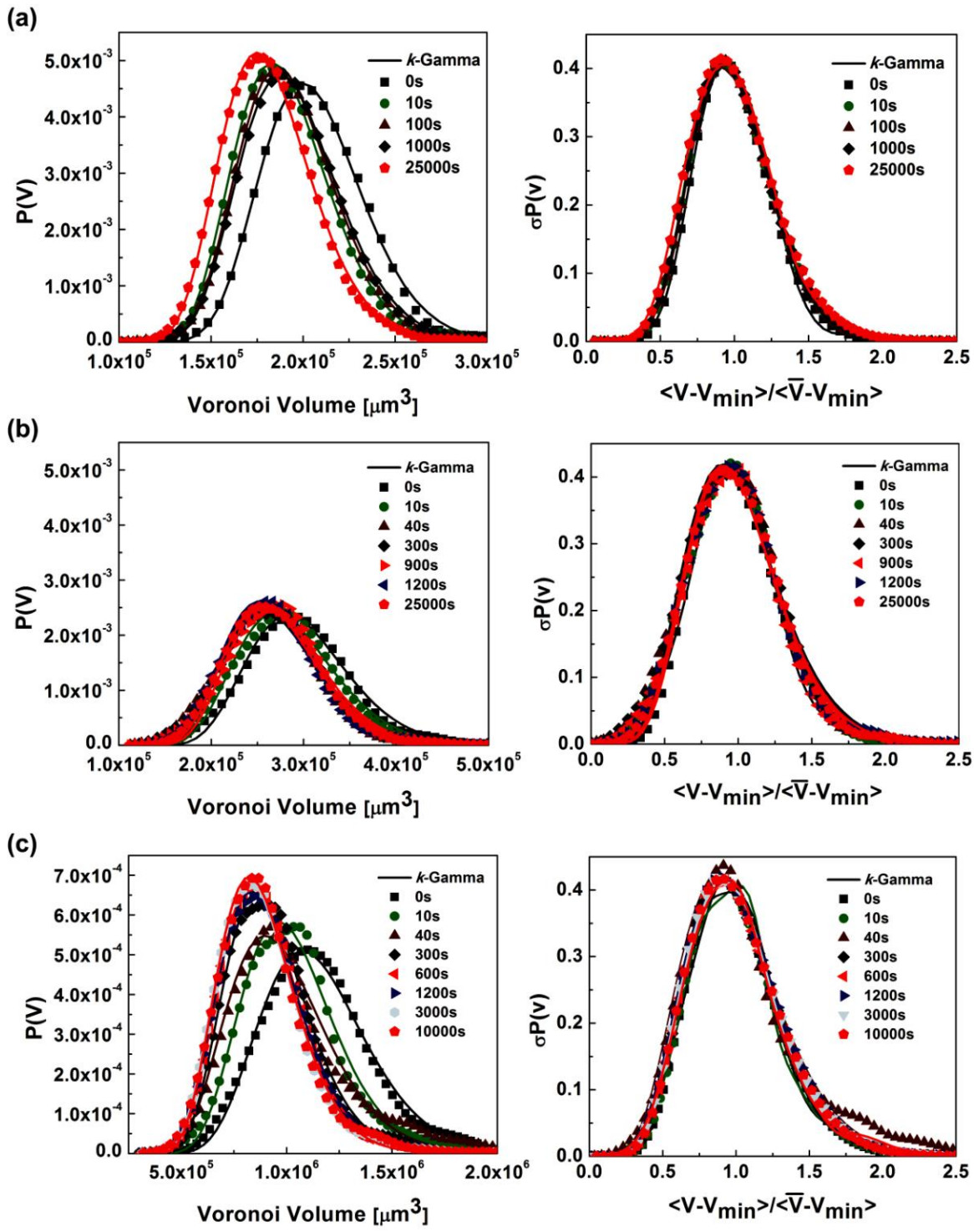

Figure 4.11 (a, left) PDF of Voronoi volume distribution for cubes and (a, right) scaled PDF's for cubes. (b, left) PDF of Voronoi volume distributions for rectangular prism granules and (b, right) scaled PDF's for rectangular prism granules. (c, left) PDF of Voronoi volume distributions for bimodal cube granules and (c, right) scaled PDF's for bimodal cube distribution.

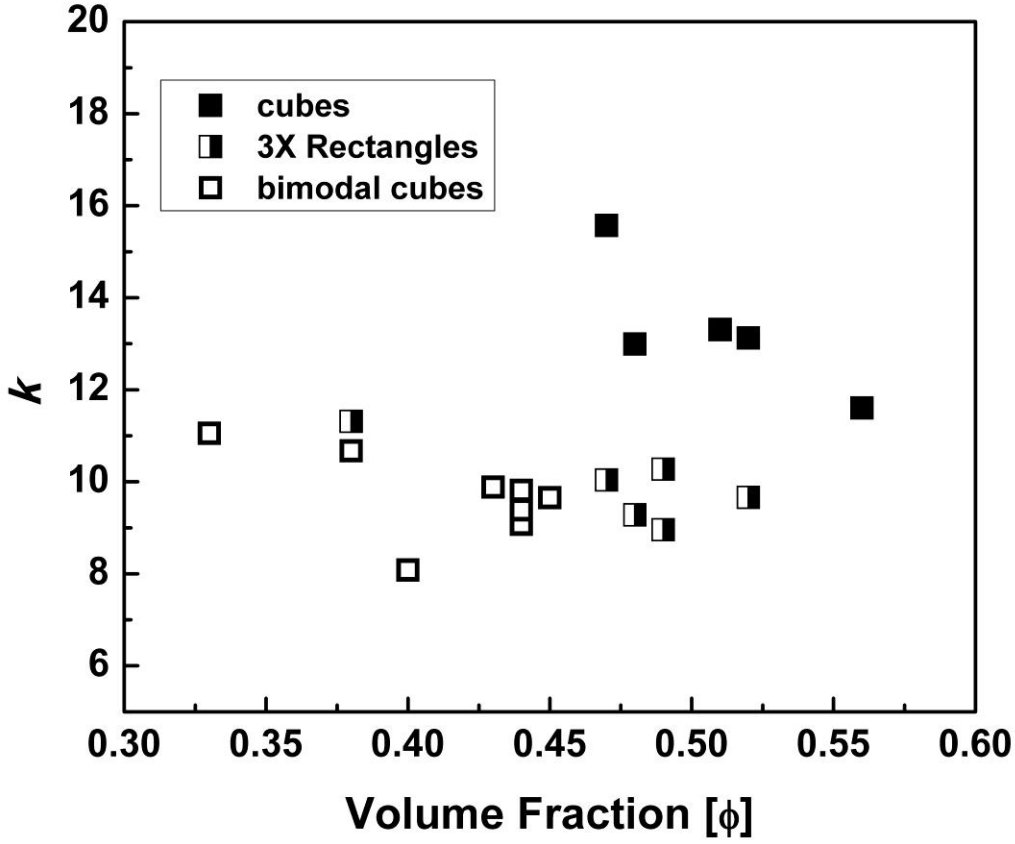

Figure 4.12 The *k* parameter from the *k*-Gamma fit to experimental Voronoi volume data for cube, rectangular prism and bimodal cube granule distributions.

CHAPTER 5

THESIS CONCLUSIONS

We have formulated two concentrated silica microsphere-hydrogel suspensions compatible with processing in confined microchannel geometries; one based on an aqueous system and the other based on an index-matched system. The aqueous suspension is used in drop-based microfluidics to assemble spherical and discoid colloidal granules in homogenous or Janus distributions. The index-matched suspension is used in stop-flow-lithography to assemble colloidal granules in non-spherical prismatic geometries, including microgears, cubes, rectangular, and triangular prisms. Finally, x-ray μCT is used to characterize the packing dynamics of non-spherical colloidal granules under horizontal agitation conditions. The principal findings of this research are summarized below:

(1) Microfluidic Assembly of Spherical Colloidal Granules

i. Spherical and discoid granules, ca. 100μm, of colloidal silica were fabricated in sheath-flow microfluidic geometries.

ii. Separate streams of colloidal suspension were delivered into separate drop hemispheres and locked into place, creating hemispherically distinct Janus granules in both spherical and discoid geometries.

(2) Microfluidic Patterning of Colloidal, Glass, and Silicon Microcomponents

i. An aqueous colloidal suspension was made transparent and thus compatible with SFL, a microfluidic based lithography platform, by index matching the silica microspheres in a DMSO:water solution.

ii. A variety of prismatic granule geometries were fabricated, including both simple and complex shapes, i.e., a microgear geometry.

iii. The microgear components were partially or fully sintered at elevated temperature to yield either porous or dense glass microgears, respectively. Representative porous microgears were further transformed into porous silicon microgears via magnesiothermic reduction.

(3) Packing Dynamics of Non-Spherical Colloidal Granules

i. X-ray μCT was used to determine the packing fraction of non-spherical granules of varying shape as a function of horizontal agitation time.

ii. A method to determine the Voronoi volume distribution from images of non-spherical granular packs was developed.

iii. The Voronoi volume distributions were fit to a probability distribution function and the resulting fit parameter was used to describe the local granule structure.

iv. All k-Gamma fits were able to rescale onto a single master curve, indicating that the jamming conditions remained qualitatively similar during consolidation.

AUTHOR'S BIOGRAPHY

Robert Shepherd was born in Honolulu, HI on November 5th, 1980 to Michael and Jacqueline Shepherd. He has lived in many other places – Dunoon, Scotland – La Madelana, Italy – Saratoga Springs, NY – Virginia Beach, VA – and Decatur/Champaign, IL, but considers Central Illinois his home. He went to Millikin University for physics, but transferred to University of Illinois – Urbana, Champaign (Illinois) to complete his bachelor's degree in Material Science & Engineering in 2002. He continued his graduate education at Illinois, pursuing a Ph.D under the advisement of Dr. Jennifer Lewis and seeking an M.B.A. with a focus on entrepreneurship.

During these pursuits, he gained a strong understanding of complex fluids and the tuning of rheology to advance the fields of microfluidics and three-dimensional printing. Robert has used his knowledge of complex fluids and passion for entrepreneurship to found a venture backed company, Liquid Glass Technologies, Incorporated. This company's flagship product is a pad that adheres to golf clubs and 'changes color', to indicate the impact point and club-face angle; the product's name is *Fracture Pad*. Robert will continue to help grow this company remotely after graduation.

During his time at Illinois, he met another Material Science graduate student named Jennifer Hanson. After four years of dating, they were married on September 5th, 2009 in Roseville, MN – her hometown. Robert and Jennifer have collaborated on the fabrication of hydrogel scaffolds for tissue engineering applications, with one published journal article and another submitted article. Both Robert and Jennifer will pursue post-doctoral research in Boston, MA; Jennifer under Dr. Michael Cima (M.I.T.) and Robert under Dr. George Whitesides (Harvard University).